2. RADIATION EFFECTS ON FAST REACTOR CLADDING AND STRUCTURAL MATERIALS

(1304)

J. Moteff,* F. D. Kingsbury,† J. P. Smith†

The objective of this program is to determine the effect of radiation on the time-, temperature-, and stress-dependent properties of selected heat-resistant alloys and refractory metals, to identify the causes of any changes observed in these properties, and to develop remedial measures.

The experimental program to study effects of neutron irradiation on the creep-rupture, tensile, hardness, and resistivity properties of the above classes of metals and alloys is continuing. Direct observations of defect configurations by means of the transmission electron microscope, and analysis of the neutron-induced defects and their migration behavior, are being performed and correlated with the measured changes in the mechanical properties. Detailed spectra studies are being performed to determine an accurate profile of flux and energy distribution of reactor positions used in the program.

Materials investigated in the heat-resistant alloys portion of the program include A-286, Hastelloy X, Hastelloy N (INOR-8), Hastelloy R-235, Fe-Cr-Al-Y alloys, AISI 304, 316, and 348 stainless steels, ASTM-A302B and A350-LF3 pressure vessel steels, and various Inconel and Incoloy alloys.

The refractory metals portion of the program includes investigations of V, Mo, Nb, W, Ta, and their alloys.

2.1 STATUS OF IRRADIATIONS (F. D. Kingsbury, J. P. Smith, W. S. Chenault)

EBR-II IRRADIATION PROGRAM

A planned program of fast neutron spectrum irradiations in the EBR-II reactor was initiated in conjunction with ORNL. This program is a reorientation of a previous program for a series of irradiations in the Fermi reactor. Two phases of the present program were implemented.

Phase I consisted of irradiating Fe, Ti, Ni, and Co dosimeters and 16 refractory metal tensile/creep-rupture specimens. The irradiation of 148 dosimeters resulted in complete flux mapping of the EBR-II rows 2 and 7 positions with the new 91-element reactor core configuration. Irradiation was conducted at a maximum reactor power level of 30 Mw to a total integrated exposure of 688 Mw hours. The neutron flux density profile was determined in order to interpret subsequent EBR-II material irradiations and to correlate irradiation test results from other reactors. The radiochemical analysis of the dosimeters are discussed in the dosimetry section.

*Project leader.

†Principal investigator.

Phase IIA of the program provides for the irradiation of resistivity, hot-hardness, and tensile/creep-rupture specimens at various elevated temperature and fluence values. Individual NMPO capsules, loaded into the tube bundles by ORNL personnel and awaiting insertion into the EBR-II, include 112 tensile/creep-rupture specimens, 64 hot-hardness specimens, and 264 resistivity (wire) specimens. Materials to be irradiated are the heat-resistant alloys Hastelloy X, Hastelloy R (three different B isotope dopings), Fe-Cr-Al-Y, and Mo, Cb, W, Ta, and their alloys. Additional materials including stainless steels and vanadium-base alloys are planned for Phase IIB.

ORR AND ETR IRRADIATIONS

Four refractory metal specimen capsules were irradiated in the ORR and four heat-resistant alloy capsules were irradiated, three in the ETR, one in the ORR.

2.2 HEAT-RESISTANT ALLOY PROGRAM

The objectives of this phase are to determine engineering and design data of heat-resistant alloys and to interpret these data (with supporting transmission electron microscopy) to determine the mechanisms of radiation damage. Materials tested include Incoloy 800, Hastelloy X, A-286, Hastelloy R-235, and Fe – 15Cr – 4Al – 1Y (1541 alloy).

CREEP-RUPTURE TESTING (R. A. Joseph, J. P. Smith, J. Moteff, J. A. Edwards)

All creep-rupture testing except for the 1541 alloy was performed in standard lever-loaded (5:1 ratio) dead-weight equipment. Essentially all creep data to be discussed were measured from total load train movement. To determine the order of magnitude of error inherent in this technique, several specimens were instrumented with platinum strip-type extensometers attached directly to the gage length of the specimens. Comparison of strain as determined by the load-train LVDT sensor against the optical showed that for strains above 2 percent the relative error was less than 10 percent. For strains less than 1 percent, the relative error was somewhat higher (up to 40%). These tests verified that the total load-train monitoring system utilized was satisfactory for recording strains above 1 to 2 percent, generally well below the range at which second-stage or minimum creep occurs with the possible exception of extremely brittle materials.

Incoloy 800

Specimens of Incoloy 800, irradiated at about 540°C in EBR-II to fast fluences of 0.27 and 2.7 x 10^{20} n/cm^2 ($E_n \geq 1$ Mev), were creep-rupture tested at 540°C and 705°C. Data are summarized in the graphs of Figures 2.1 and 2.2. Radiation affects the creep properties somewhat differently at the two temperatures. At 540°C the minimum creep rate ($\dot{\epsilon}$) is increased and time to rupture (t_R) is reduced compared to the unirradiated material; at 705°C, $\dot{\epsilon}$ is reduced and t_R increased (except at high stresses) compared to the control specimens. At both test temperatures radiation reduced the rupture elongation by about a factor of 3. Another significant difference is that for 540°C tests the irradiated and control lines tend to converge at low stresses but more tests are needed to verify this; on the other hand, the tendency for convergence of the unirradiated and irradiated control lines at 705°C is at high stresses. This convergence at high stress is unique among alloys investigated at NMPO; generally any convergence occurs at low-stress (longtime) tests, as appears to be the case at 540°C (Figure 2.1), indicating annealing of point defects. To determine whether the effect observed at 705°C was due to thermal aging or to combined stress and temperature, an irradiated and an unirradiated control specimen were aged at 705°C for 500 hours and then tested at 10.5 kg/mm^2. The irradiated specimen ruptured after 24.7 hours and had a minimum creep rate of 2.4 x 10^{-6} sec^{-1}, and a fracture elongation of 37 percent; these properties are essentially identical to those of the as-irradiated tests shown in Figure 2.2. This indicates that the divergence of the control

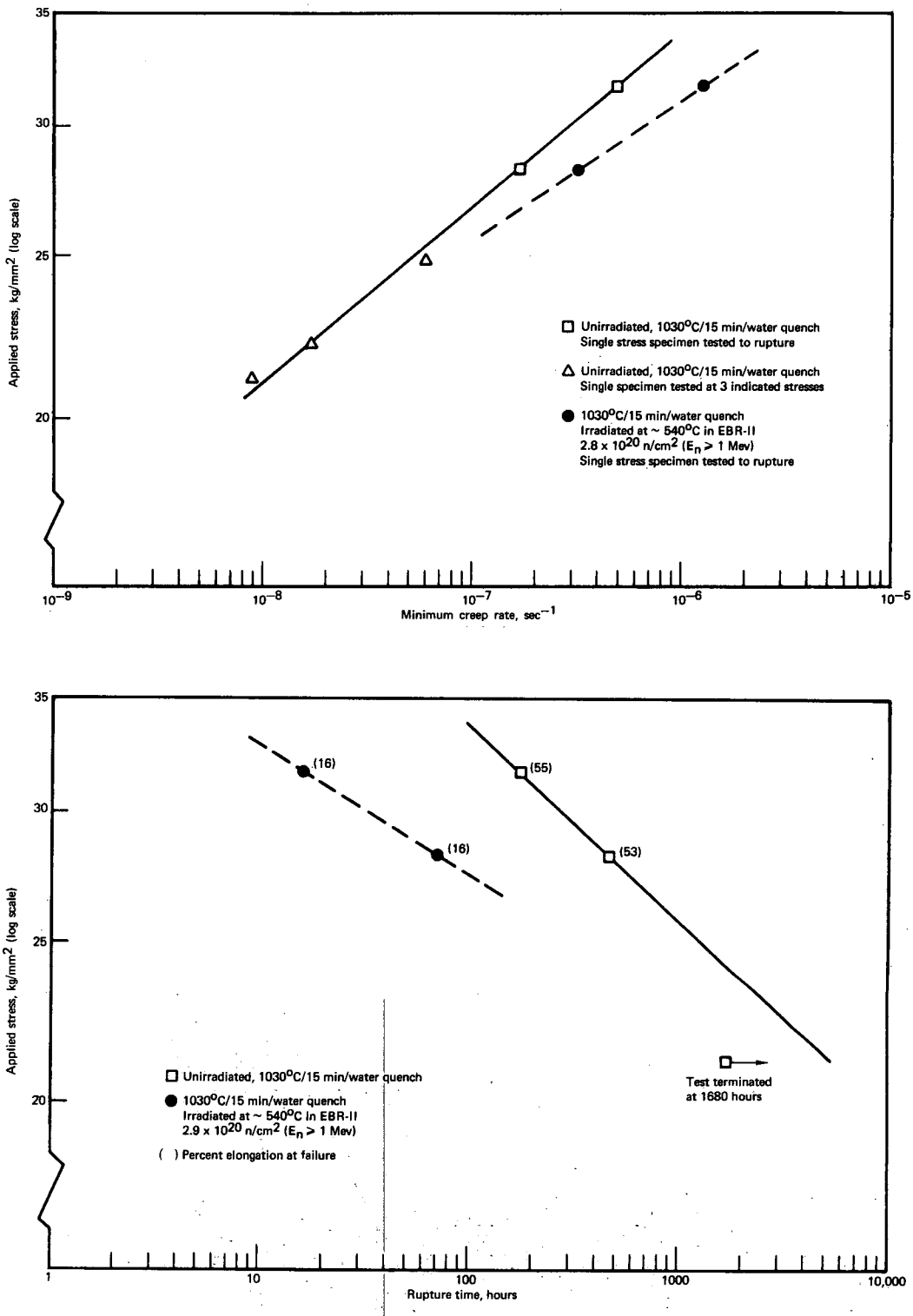

Fig. 2.1 — Minimum creep rate and stress-rupture strength for unirradiated and irradiated Incoloy 800 at 540°C

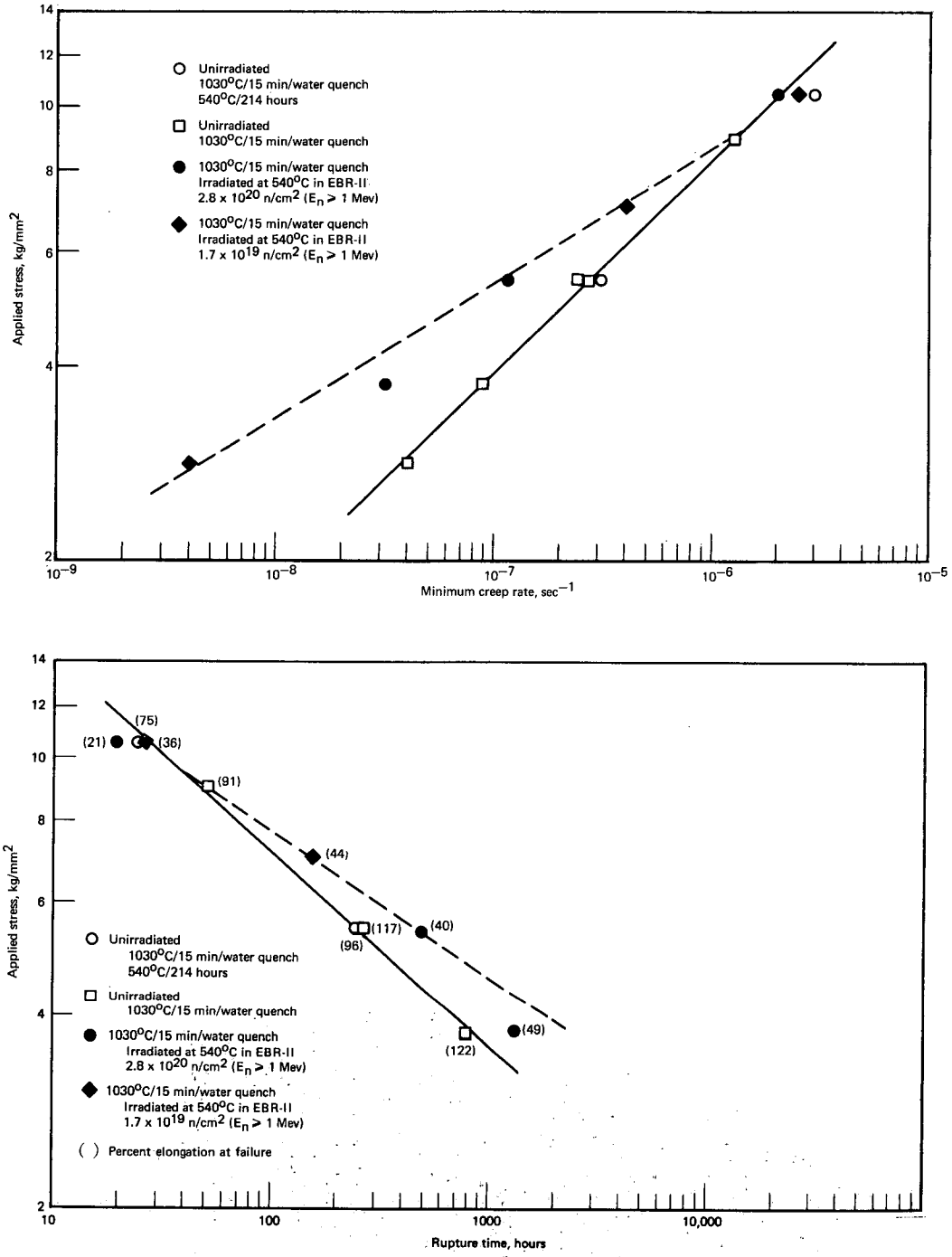

Fig. 2.2 – Minimum creep rate and stress-rupture strength for unirradiated and irradiated Incoloy 800 at 705°C

and irradiated 705°C properties (Figure 2.2) at low stress is not due solely to thermally activated migration or interaction of irradiation-induced defects; more tests are needed to determine the cause of the increased post-irradiation strength.

The creep curves for the 540°C and 705°C tests (Figure 2.3) indicate reduction in post-irradiation ductility. The major effect of radiation on ductility is the reduced third-stage creep strain.

The tests described above were of the creep-rupture variety performed at a fixed load to failure. Actual reactor operations do not result in this condition; instead, the stress varies over a rather wide range. To investigate the effects of varying stress and to determine accurately how radiation affects the low strain part of the creep curve, tests were performed in which the stress on a given specimen was varied and the strain was measured accurately with a cathetometer sighting directly on the gage length of the specimen. The low-strain range is of particular interest to designers since many cladding designs allow for 3 percent maximum strain. The procedure was to load a specimen to σ_1 and establish the linear creep rate; the load was then increased to σ_2 and again a linear creep rate was established; this was repeated for three stress levels. Finally the load was re-

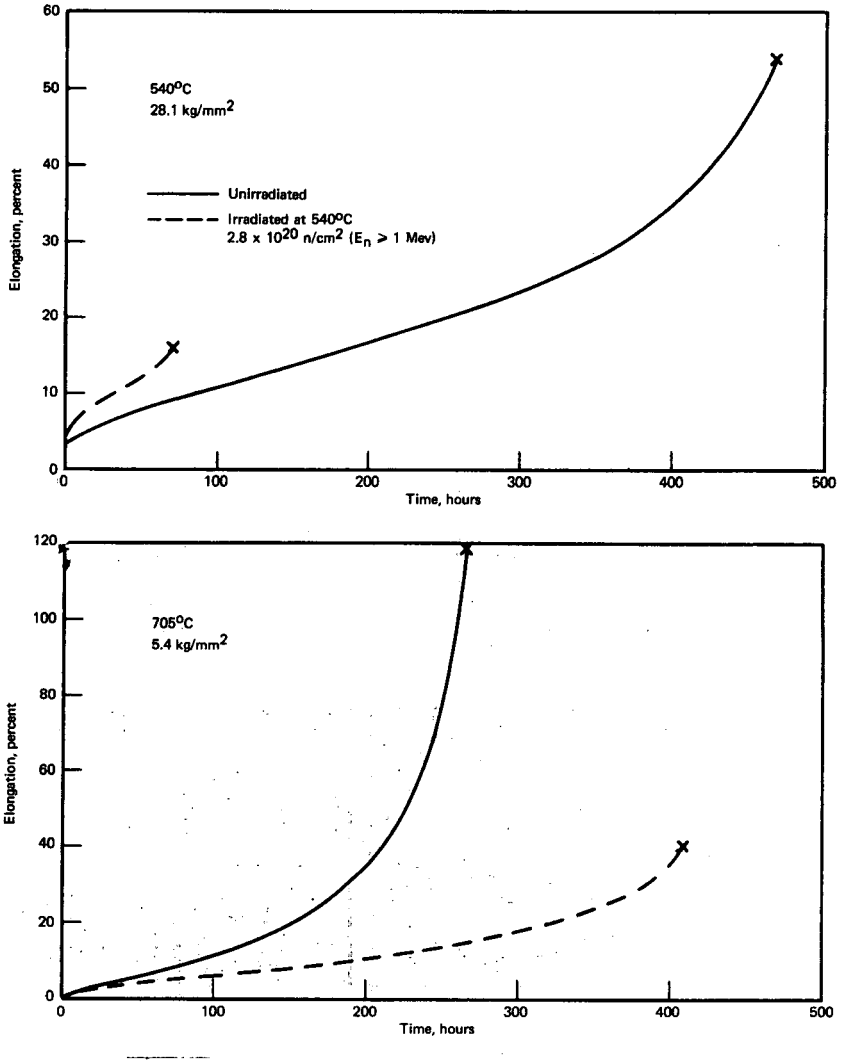

Fig. 2.3 — Creep curves for irradiated and unirradiated Incoloy 800 at 540°C and 705°C

duced to σ_1 to compare with the original creep rate at σ_1 and to determine whether the substructure had been altered. Creep data were obtained for irradiated and control specimens and are shown in Figures 2.4 and 2.5. For the unirradiated specimen (Figure 2.4) the minimum creep rate is apparently a function of prior stress or strain history, based on the fact that second-stage creep rate ($\dot{\epsilon}_s$) for σ_1 final is significantly higher than for σ_1 initial. In the case of the irradiated specimen (Figure 2.5) the $\dot{\epsilon}_s$ is essentially identical for σ_1 initial and final. In the unirradiated results, for σ_1 initial, two separate linear portions $\dot{\epsilon}_s$ appear to be present. The exact cause of this is not known; it has been observed on post-test metallography of other ruptured specimens that recrystallization is probably occurring during test since the grain size near the fracture is very fine and becomes progressively coarser in low-strain areas. This recrystallization could explain the two linear portions of the initial σ_1 and the decreased creep resistance of the final σ_1.

The result on the irradiated specimen indicates that irradiation "freezes in the structure" and that stresses or strains in the region investigated do not alter this structure.

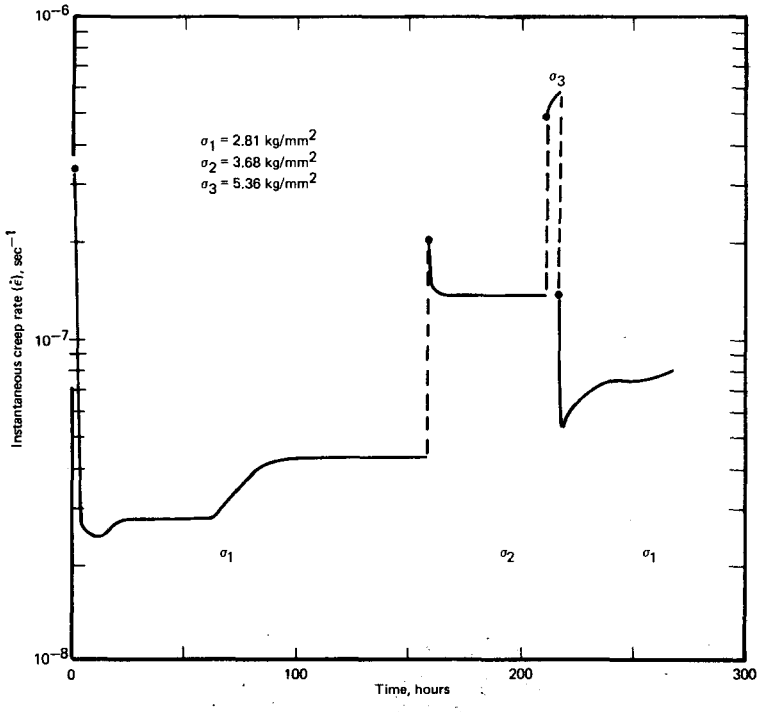

Fig. 2.4 — Instantaneous creep rate at 704°C of unirradiated Incoloy 800 as a function of creep time for various stress levels

Metallography and transmission electron microscopy will be performed to help evaluate results.

A similar series of tests was initiated at 540°C. Creep rates for the unirradiated specimens at the three lower stress levels of Figure 2.1a were all determined from one specimen; they are in good agreement with tests performed at a constant load to failure.

To more fully evaluate all available test data, correlations are being made between creep and tensile data. Tensile data discussed here were generated at GE-APO[1] on samples from the same heat and irradiation as for the specimens described above. Figure 2.6 demonstrates a reasonably good correlation of the tensile and creep data both for strength and ductility. Of particular interest were (1) the effect of fluence on the ductility but not on the strength, and (2) the minimum in the ductility curve for the irradiated specimens.

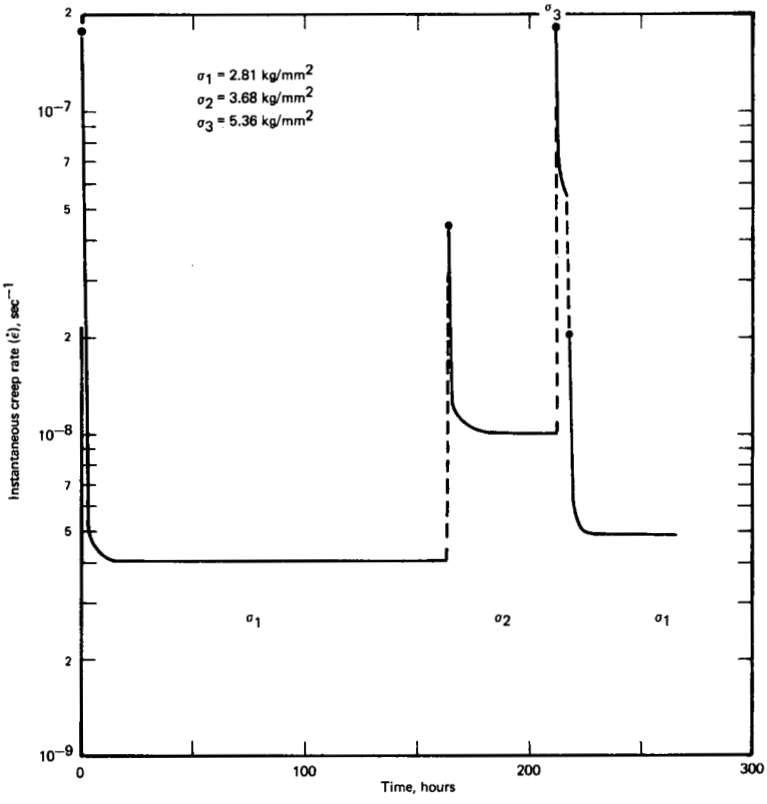

Fig. 2.5 — Instantaneous creep rate at 704°C of irradiated (2.4×10^{19} n/cm^2, $E_n \geq 1$ Mev) Incoloy 800 as a function of creep time for various stress levels

Stiegler and Weir[2] reported such a minimum for Hastelloy N. A unique approach to correlating the tensile and creep data is the application of the Monkman-Grant relationship[3] (log $\dot{\epsilon}$ vs log t_R) as shown in Figure 2.7. At both temperatures, data fall on lines close to the predicted slope of -1, and available tensile data fit the curve quite well. The effective t_R for the tensile data was obtained by calculating $\epsilon/\dot{\epsilon}$ for each test where ϵ is the fracture strain. Refinements can probably be made, such as using uniform strain, although the above technique appears to work quite well to a first approximation. The slope is unity; hence $\dot{\epsilon} \cdot t_R$ = constant. Although the units of this constant are strain, its physical significance is not known. It may be used as a guide to predict the minimum fracture strain since what it represents is the strain at failure obtained if no third-stage creep occurred. Since most unirradiated materials do exhibit a third-stage creep, the fracture ductility is generally somewhat higher than predicted by the Monkman-Grant relationship. On the other hand, many irradiated materials exhibit little or no third-stage creep and this relationship may predict quite closely the fracture ductility.

Hastelloy X*

Concurrent to the work described above, creep-rupture testing of Hastelloy X irradiated in EBR-II was performed in the range of 540° to 705 °C. Most data were generated at 650 °C since the primary intent was to compare these data with previously determined data from ETR irradiations. The 540 °C and 705 °C data are presented in Table 2.1 but will not be discussed because of the limited quantity. Stress-rupture life at 650 °C of the

*Specimens fabricated and irradiated by GE-APO.

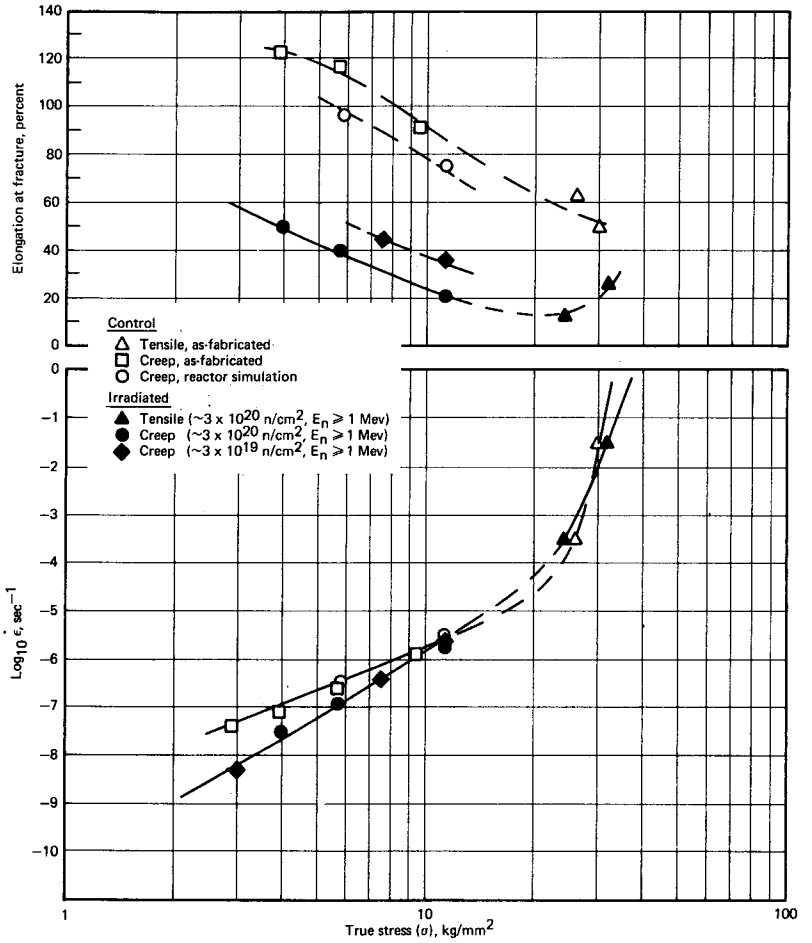

Fig. 2.6 – Strain rate and elongation as a function of true stress for Incoloy 800 tested at 705°C. To minimize structure differences due to work-hardening the true flow stress at about 6% true strain was used to correlate the tensile data with the creep data.

specimens from the EBR-II and ETR irradiations, as summarized in Figure 2.8, was essentially the same. Ductilities (not shown) from both irradiations were similar, but the EBR-II specimens showed slightly lower ductility due to the higher fluence. The point of convergence for control and irradiated lines is about 20 kg/mm^2. Creep data were not obtained for the ETR irradiated specimens. The strain rate-stress relationship for the EBR-II specimens (Figure 2.9) shows the creep rate to be reduced by irradiation; reduction is greater at lower stresses. The irradiated and control curves of Figure 2.9 converge at about 27 kg/mm^2, a stress higher than for the t_R-σ curves. Creep curves (not illustrated) for irradiated and control specimens at 650°C show that the major reason for the loss in ductility is the reduction of third-stage creep; the same was true of Incoloy 800 (Figure 2.3). The Monkman-Grant[3] relationship was also applied to these data as shown in Figure 2.10. Although the lines are not so close to a slope of -1 as the Incoloy 800 data, the control and irradiated lines are parallel. Based on the criterion discussed above that $\dot{\epsilon} \cdot t_R^k$ = constant, the constant $\cong$ 0.06. Irradiated Hastelloy X exhibited virtually no third-stage creep and the fracture ductility was 8 to 9 percent which is not much above predicted minimum of 6 percent.

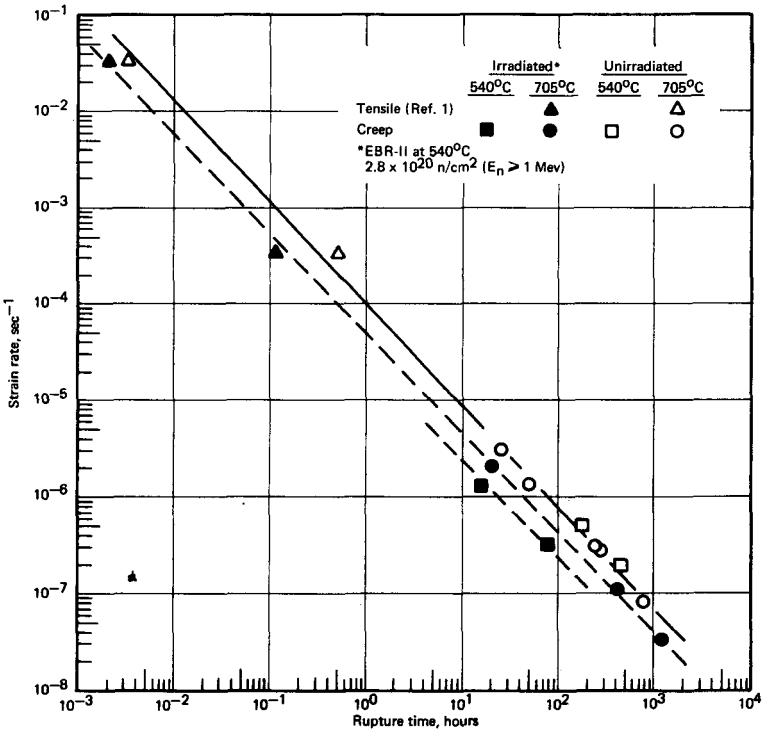

Fig. 2.7 — Monkman-Grant relationship for irradiated and unirradiated Incoloy 800 at 540°C and 705°C using tensile and creep data

TABLE 2.1

CREEP-RUPTURE DATA FOR IRRADIATED AND UNIRRADIATED HASTELLOY X

EBR-II Irradiation Conditions		Test Conditions				
Fluence, n/cm^2 ($E_n \geq 1$ Mev)	Temperature, °C	Stress, kg/mm^2	Temperature, °C	Rupture Life, hr	Minimum Creep Rate, sec^{-1}	Fracture Elongation, % in 2.54 cm
Unirradiated		39.4	540	On test	1.1×10^{-8}	–
3.2×10^{20}	540	39.4	540	On test		
1.7×10^{19}	540	39.4	540	636	1.7×10^{-8}	21.7
Unirradiated		15.7	705	355	3.0×10^{-7}	78
Unirradiated		17.1	705	229	3.6×10^{-7}	58
3.2×10^{20}	540	15.7	705	126	7.7×10^{-8}	5

Hastelloy R-235

Creep-rupture measurements are continuing on the special split heat of Hastelloy R-235 containing a total of 45 ppm boron with varying B^{10} concentration. Specimens were tested at 870 °C following irradiation in the ORR at 70 °C and in the ETR at 760 °C. Results of the post-irradiation creep-rupture tests are shown in Figure 2.11. Only two specimens of each type were available from the ORR irradiation. Data in Figure 2.11 indicate that (1) the 760 °C irradiated specimens exhibit slightly poorer properties than the 70 °C specimens, and (2) the stress dependency is not significantly changed by irradiation. The amount of damage appears to be definitely a function of the B^{10} concentration. One specimen of each heat from the ORR irradiation was re-solutioned and aged after irradiation and before testing; results are shown in Figure 2.11. As observed in other alloys, the rupture strength is further decreased by the re-heat treatment compared to the as-irradiated

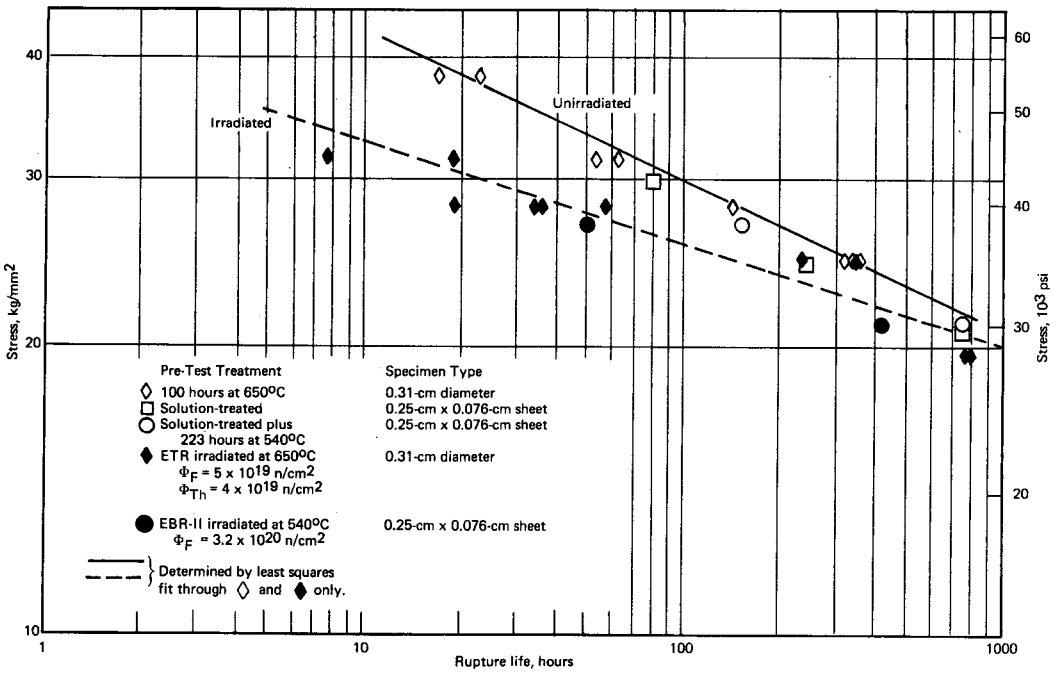

Fig. 2.8 — Stress-rupture properties of irradiated and unirradiated Hastelloy X at 650°C

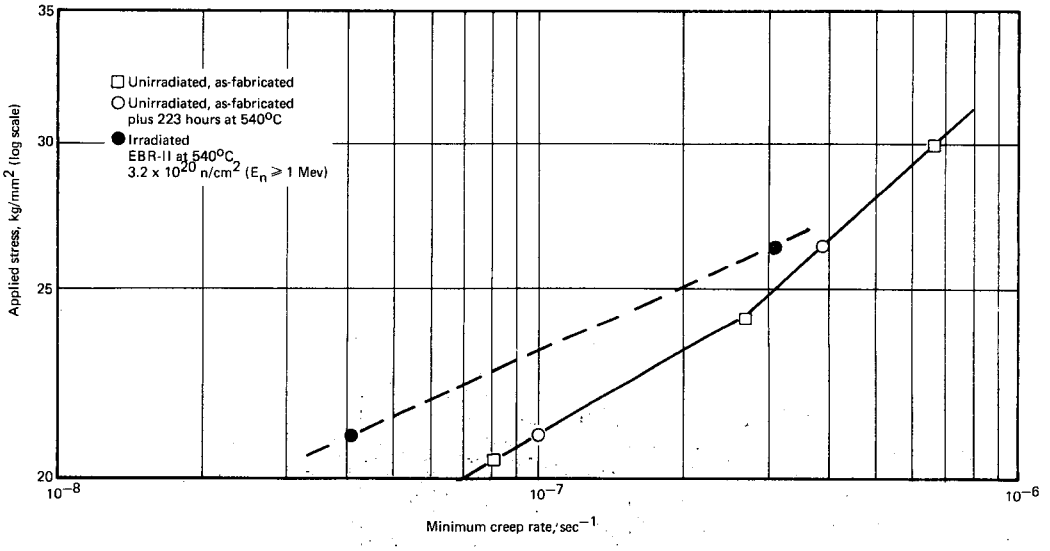

Fig. 2.9 — Minimum creep rate as a function of applied stress for unirradiated and irradiated Hastelloy X at 650°C

values. Analyses of these tests are continuing, to determine the relationship between creep rate, helium concentration, and defect density.

A-286

As discussed in a previous report,[4] Woodford[5] showed that the stress dependency, n, can be approximated from a single constant-load test for a fixed temperature. The expression $\dot{\epsilon} \approx A\sigma^n$ can be used in this analysis, with n, the stress dependency, equal to $(d \log \dot{\epsilon}/d \log \sigma)$ and inversely proportional to the strain rate sensitivity m; i.e., $m = 1/n =$

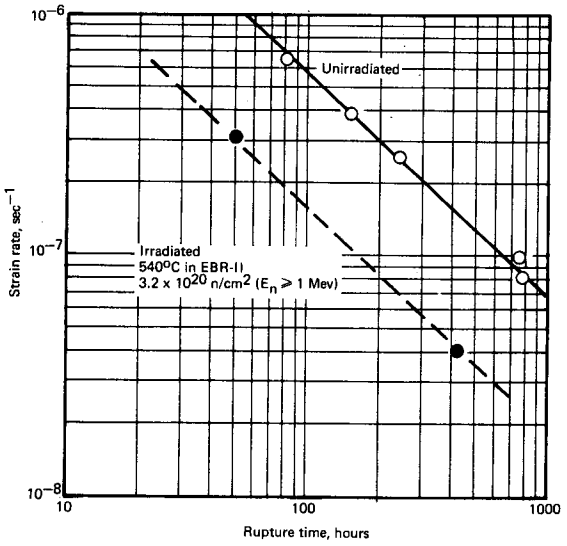

Fig. 2.10 – Monkman-Grant relationship for irradiated and unirradiated Hastelloy X at 650°C

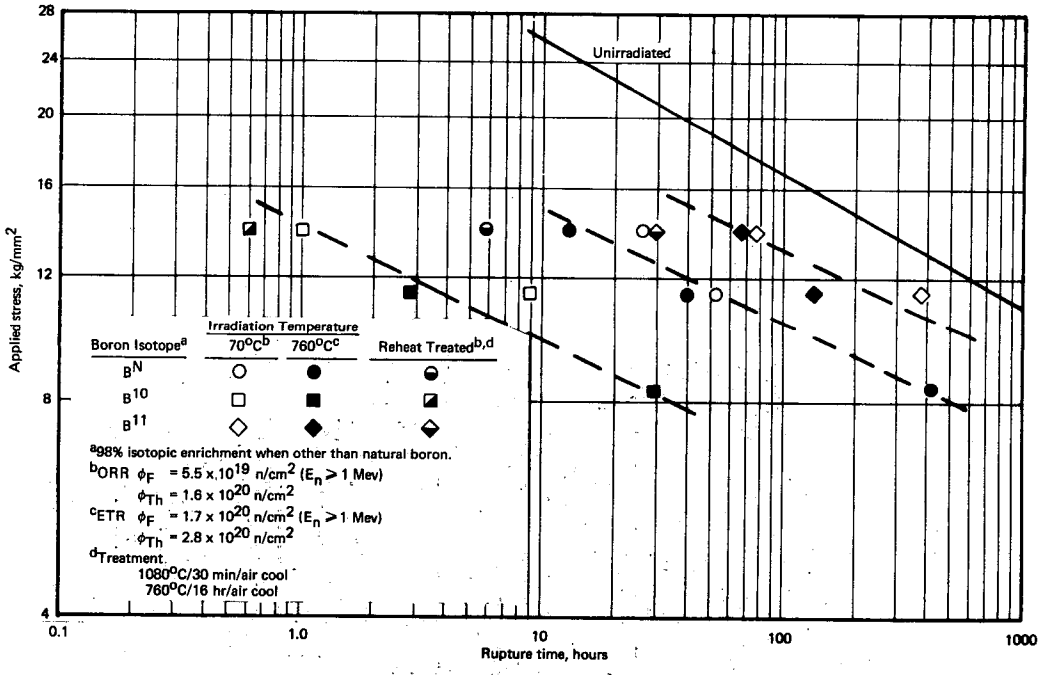

Fig. 2.11 – Creep-rupture strength and effect of post-irradiation reheat treatment on creep-rupture strength of Hastelloy R-235 at 870°C

(d log σ/d log $\dot{\epsilon}$). Data presented previously[4] showed that three different tests of Hastelloy X at 650 °C and various initial stress levels yielded essentially the same value of n. This type of analysis was applied to irradiated and unirradiated test results of A-286 specimens.

The results shown in Figure 2.12 indicate about a factor of 2 increase in the stress dependency. More significantly, the minimum creep rate decreases with increasing concentration of helium atoms as generated from the $B^{10}(n,\alpha)Li^7$ reaction. In this figure the stress notation is omitted from the abscissa because the comparison is for creep tests performed at the same applied stress. Since there is essentially no primary creep, the intercept represents the minimum creep rate.

The minimum creep rate is plotted as a function of the calculated helium atom concentration in Figure 2.13; there appears to be a fairly good linear relationship. Minimum creep rate could be a function of the number of $B^{10}(n, \alpha)Li^7$ reactions which occur and is probably a function of the helium atom concentration. Strain rate sensitivity (m) is independent of helium atom concentration in the range investigated as shown in Figure 2.12. The interaction of dislocations with helium bubbles may account for the increased creep resistance; this is consistent with transmission microscopy results reported previously.[4] The reduced ductility in irradiated A-286 could, however, be the result of decreased strain rate sensitivity (increased n or decreased m) which apparently is not a sensitive function of total helium atom concentration. The ductility change may also be a function of helium atom distribution; i. e., bubbles on those dislocations within grain boundaries may play a special role. Studies to correlate influence of changes in stress dependency and strain rate sensitivity on creep ductility and creep rates are continuing.

Fe - 15Cr - 4A1 - 1Y

Data for Fe - 15Cr - 4A1 - 1Y (1541 alloy) tensile and creep tests by ORNL,[6] Harwell,[7] and NMPO were compiled. Results of unirradiated tests are presented in Figure 2.14 as the temperature-compensated creep rate (Zenner-Holloman parameter) versus stress. The ultimate strength was used for the tensile data, although the yield strength could have been used since they are virtually the same for this alloy. The applied stress was used for creep data. Considering the variation in test technique among the different laboratories and the inclusion of both tensile and creep data, a good least-squares fit to the experimental data was obtained with relatively little scatter. Figure 2.15 shows the similar parameter plots for the irradiated specimen data. This plot shows that irradiation reduces creep rate slightly but consistently for all test conditions considered, and that the stress dependency (n) for this irradiated material is not significantly changed. This is in contrast to the results discussed above for Incoloy 800, Hastelloy X, and A-286. The Woodford technique[5] of calculating stress dependency from a single constant-load test was applied to the NMPO creep data, and the analysis predicted that the stress dependency (n) was essentially unchanged by the irradiation.

HOT HARDNESS (J. L. Kamphouse)

Incoloy 800

Hot hardness tests were performed on control and irradiated Incoloy 800 from the same material used to fabricate the control and irradiated specimens used for the creep and tensile results discussed above. A summary of the hot-hardness data is shown in Figure 2.16. There is very little difference in hardness between the irradiated and unirradiated material at any given temperature, especially from 500 °C and below. At 600 °C and above, the irradiated specimen appears to be slightly harder than the unirradiated specimen, possibly because the irradiation temperature was approximately 540 °C; hence significant changes in strength would not be expected below this temperature. Of significance is the fact that tensile data[1] on these

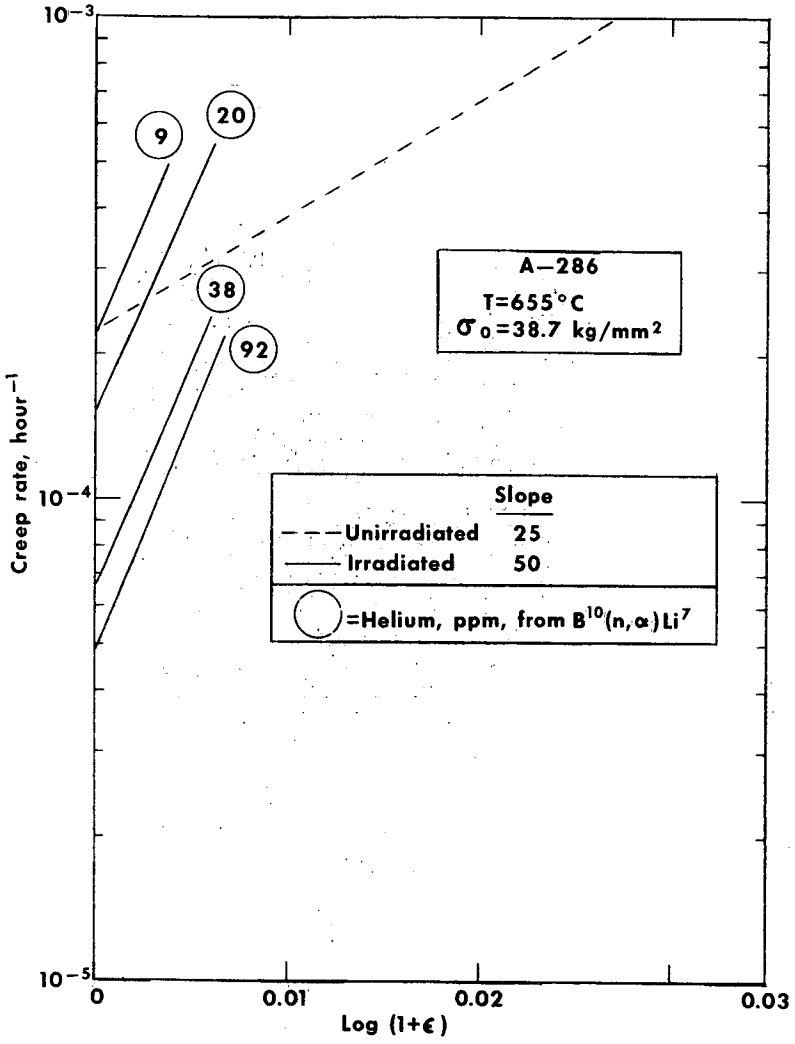

Fig. 2.12 – Creep rate as a function of Ln (1 + ϵ) for irradiated and unirradiated A-286 (AS-746F)

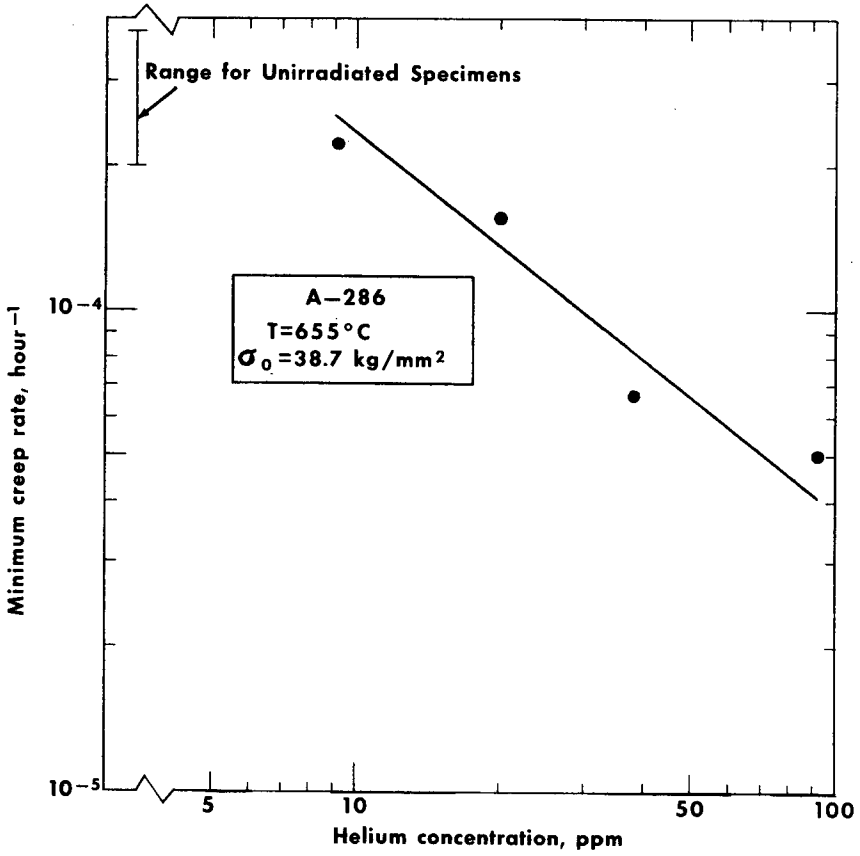

Fig. 2.13 – Minimum creep rate as a function of helium concentration for irradiated A-286 (AS-746H)

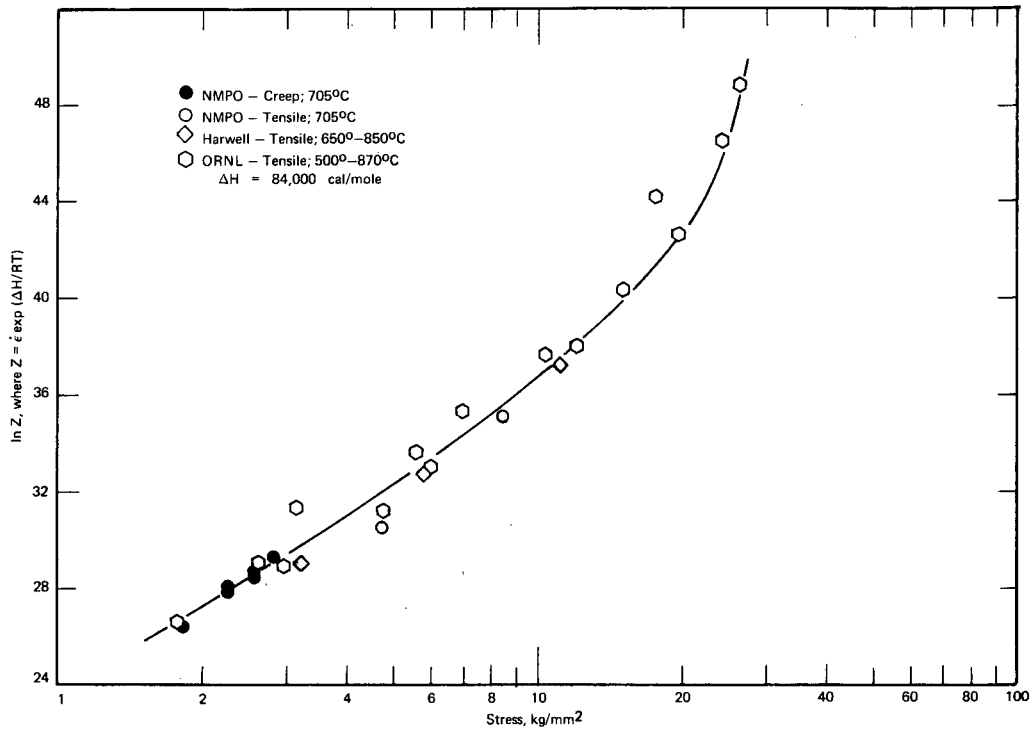

Fig. 2.14 – Variation of temperature-compensated strain rate (Z), Zenner-Holloman parameter, with stress for unirradiated Fe – 15Cr – 4Al – 1Y

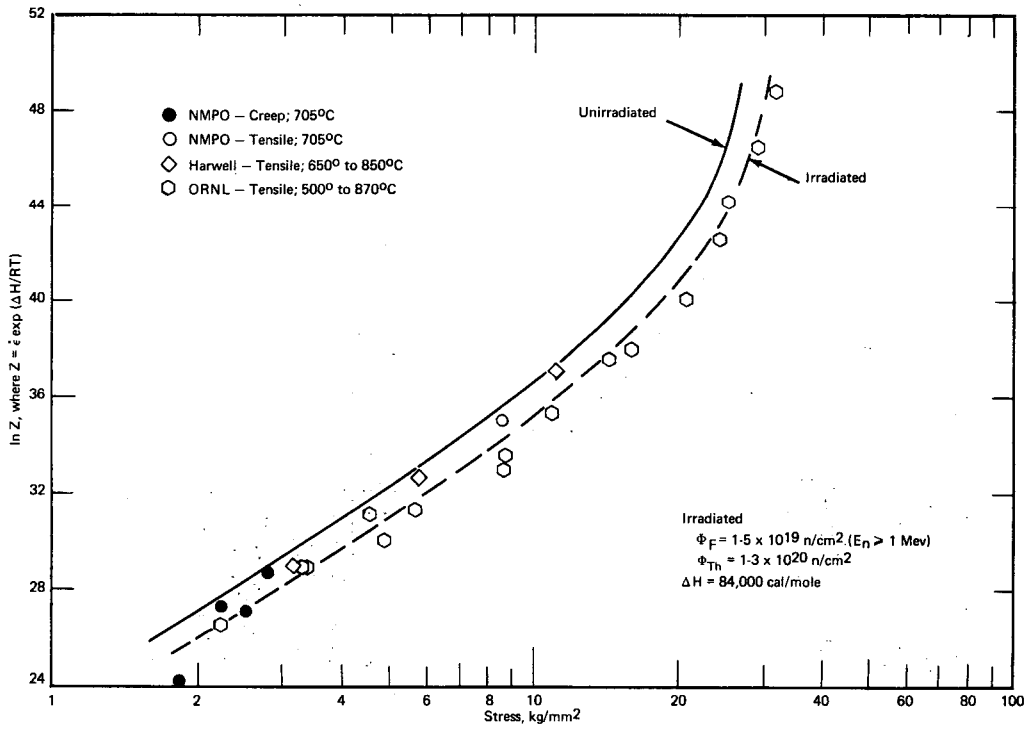

Fig. 2.15 – Variation of temperature-compensated strain rate (Z), Zenner-Holloman parameter, with stress for irradiated Fe – 15Cr – 4Al – 1Y

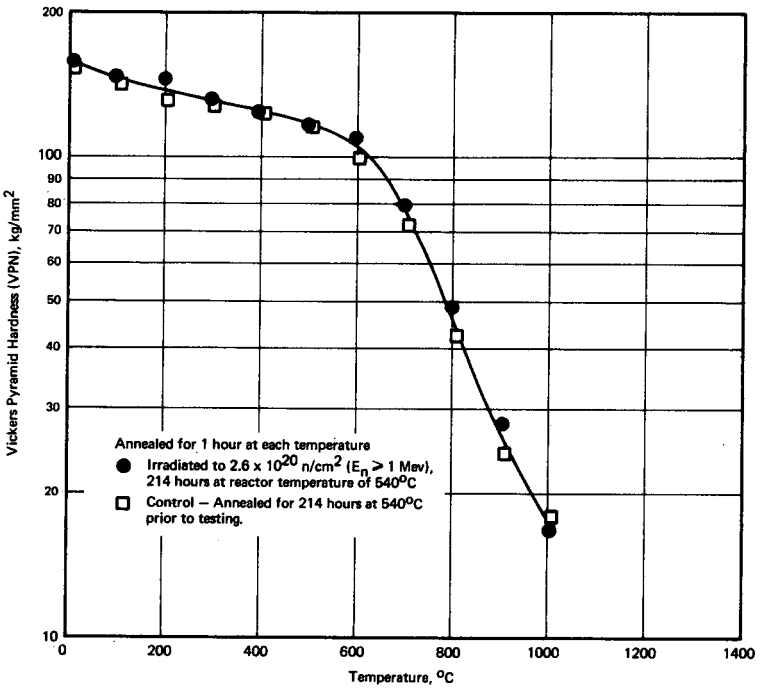

Fig. 2.16 – Hot microhardness of unirradiated and irradiated Incoloy 800

same specimens in the 600° to 700°C range show only a small strength reduction (~ 5 to 10%) due to irradiation; hence these two types of tests are in qualitative agreement.

The discontinuity at 200°C may be real because the tensile data[1] cited above show that the line through the data from the irradiated specimens crosses the line through the control data at about 200°C. That is, below 200°C the strength of the irradiated specimens is slightly higher than the control specimens, whereas above 200°C the strength of the irradiated specimens is generally lower than the control specimens.

ASTM-A302B

One unirradiated ASTM-A302B pressure vessel steel specimen and three irradiated in the IRL were hot-hardness tested from room temperature to 1000°C. During irradiation the three irradiated specimens were located at different distances from the core within a pressure vessel mock-up.[8] The spectrum changed somewhat from one side of the mockup to the other and the fluence decreased from the side nearest the core to the side farthest away. The three specimens showed essentially the same hot hardness regardless of position in the mockup and in fact showed the same hot hardness as the unirradiated specimen.

RESISTIVITY STUDIES (L. K. Keys, J. Moteff)

ASTM-A302B

Preliminary studies presented on the A302B steels[8] demonstrated a good correlation between mechanical properties and resistivity, although these studies were performed over a limited fluence range ($1 - 4 \times 10^{18}$ n/cm^2). A second series of irradiation studies were carried out in the ORR at reactor ambient temperature in which a fluence range of approximately 1×10^{18} to about $7{:}1 \times 10^{19}$ n/cm^2 was obtained, Table 2.2. In Figures 2.17 and 2.18 the fractional resistivity recovery, $\Delta\rho/\rho_o$, versus annealing temperature is given for the ORR and IRL irradiations. The general form of the recovery is the same. There are

TABLE 2.2

IRRADIATION CONDITIONS AND PRINCIPLE RECOVERY PARAMETERS FOR A302B STEELS

Sample No.	Capsule	Irradiation Conditions Fluence, nvt Fast ($E_n > 1$ Mev)	Thermal	$\Delta\rho/\rho$	$(\Delta\rho/\rho_o)$ min	$\Delta(\Delta\rho/\rho_o) = \lvert(\Delta\rho/\rho_o)\ \text{min} - \Delta\rho/\rho_o\rvert$
2-3	NRL-1-5[a]	4.8×10^{18}	6.9×10^{18}	−0.0223	−0.0258	0.0035
2-5	NRL-1-3	2.7×10^{18}	3.2×10^{18}	−0.0142	−0.0229	0.0087
2-7	NRL-1-1	1.1×10^{18}	2.2×10^{18}	−0.0004	−0.0098	0.0094
2-8	ORM-49-1[b]	1.0×10^{18}	9.0×10^{18}	−0.0093	−0.0160	0.0067
2-9	ORM-49-2	1.7×10^{18}	1.7×10^{19}	−0.0118	−0.0170	0.0052
2-10	ORM-49-3	6.0×10^{18}	3.9×10^{19}	−0.0098	−0.0280	0.0182
2-11	ORM-49-4	1.1×10^{19}	7.8×10^{19}	−0.0064	−0.0278	0.0214
2-12	ORM-49-6	7.1×10^{19}	4.6×10^{20}	−0.0427	−0.0567	0.0140
2-13	ORM-49-5	4.5×10^{19}	3.8×10^{20}	−0.0365	−0.0497	0.0132

[a]Industrial Reactor Laboratory (Plainsboro, New Jersey).
[b]Oak Ridge Reactor (ORNL).

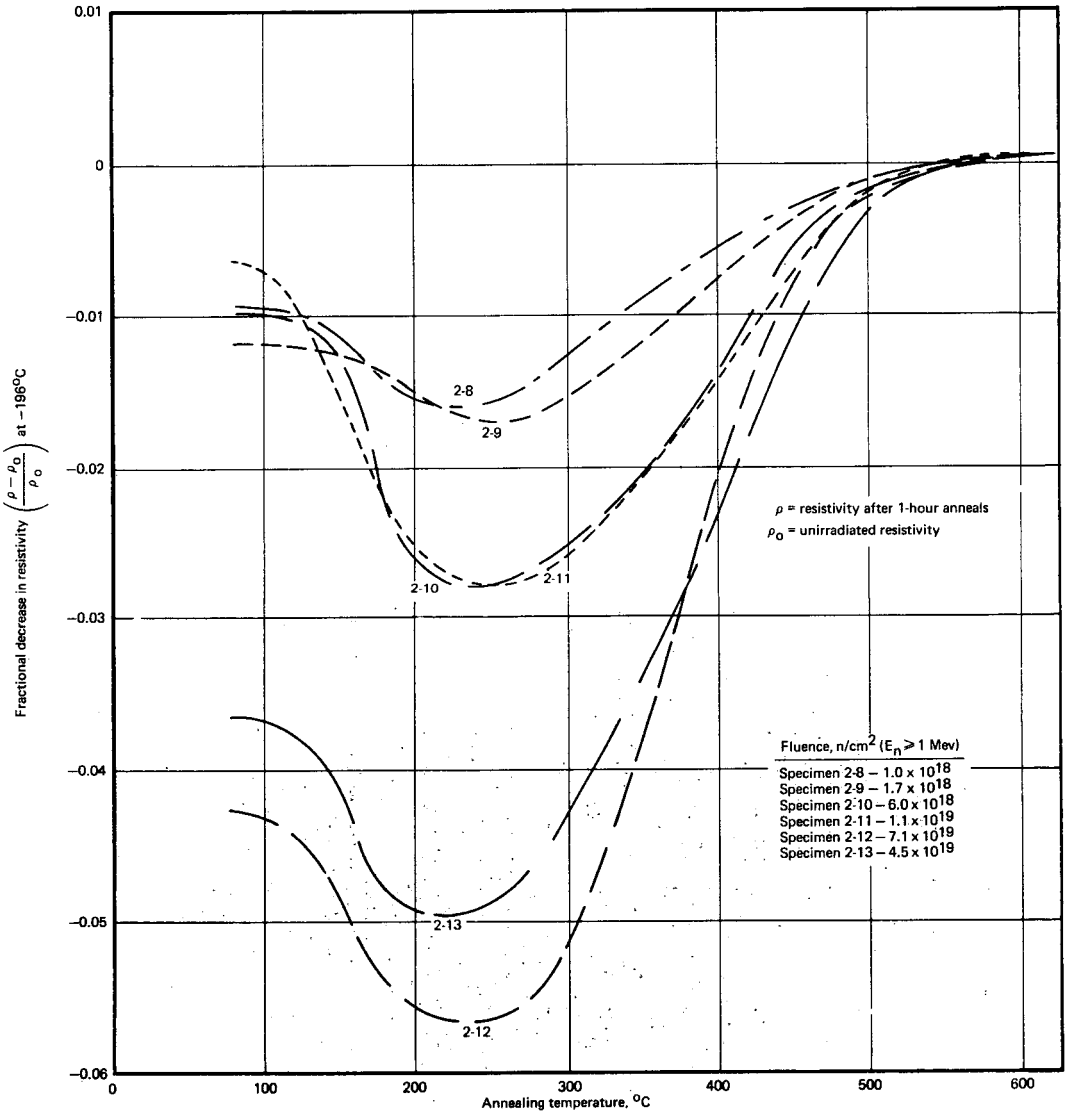

Fig. 2.17 – Isochronal fractional resistivity recovery of irradiated A302B steel as a function of annealing temperature

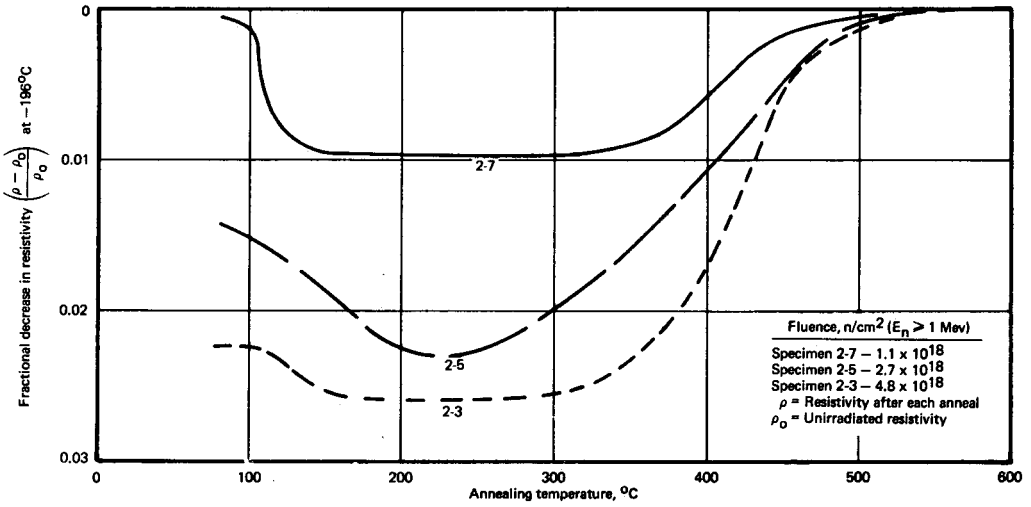

Fig. 2.18 – Isochronal fractional resistivity recovery of IRL neutron irradiated A302B steel as a function of annealing temperature

three important regions of resistivity change: (1) an initial negative resistivity change as a result of the reactor irradiation, (2) a further decrease occurring upon annealing to about 250 °C, and (3) a region of increasing resistivity and recovery up to about 500 °C above which recovery is complete and the resistivity behavior resembles that of the control specimens. The recovery minimum at about 250° C represents the maximum negative resistivity change due to the irradiation of these specimens. This minimum resistivity dependence $(\Delta\rho/\rho_o)$ on the fast neutron fluence is shown in Figure 2.19. The value $(\Delta\rho/\rho_o)$ minimum is defined as the largest negative $\Delta\rho/\rho_o$ value observed, i.e., $\Delta\rho/\rho_o$ at about 250° C. These values show a relatively smooth linear dependence on the fluence except for the lowest fluence IRL value.

Based on the work of others,[9,10] the decrease in resistivity presumably results from the precipitation of carbon from solution by the formation of a carbon-defect complex. With increasing temperature, the carbon returns to solution and the vacancies recover and are annihilated at various sinks including carbide precipitate particles, causing the resistivity to return to its original value. Although carbon has been considered the only important interstitial impurity (because of its high concentration), other interstitials such as nitrogen may have similar effects.

In Figure 2.20 the dependence of the radiation-induced resistivity increment $\Delta\rho/\rho_o$ on the fast neutron fluence is presented for the two different irradiation experiments. Both the IRL and ORR irradiations show a negative dependence of the resistivity increment fraction on the fast neutron fluence over the total fluence region rather than the normal positive dependence expected for radiation-induced defects (vacancies and interstitials). The IRL specimens, however, show a somewhat higher fluence dependence than the ORR specimens. Several factors can contribute to the difference: (1) differences in the metallurgical conditions between the two sets of samples, (2) differences in the reactor spectrum between these irradiations, and (3) differences in the temperatures of the irradiation.

Based on the known location of the test specimens within the original block of steel and on annealing studies of unirradiated specimens, the difference in fluence dependency is believed due primarily to variations of solutioned carbon from specimen to specimen. These annealing studies indicate that the IRL specimens were probably cut from a section which had more carbon in solution; hence more was available for radiation-induced precipitation. Carbon

analysis will be obtained to verify the implications of these resistivity studies. The effects of spectra and temperature were evaluated, but are probably minor compared to effects of pre-irradiation heat treatment. Other investigators[11] have also shown that the heat treatment of A302B and other mild steels has a major effect on the sensitivity to fast neutron irradiation.

Figure 2.21 shows the dependence of the nil ductile transition temperature (NDT) on the fast neutron fluence for A302B steel,[12] and illustrates a good correlation with the resistivity fluence dependence.

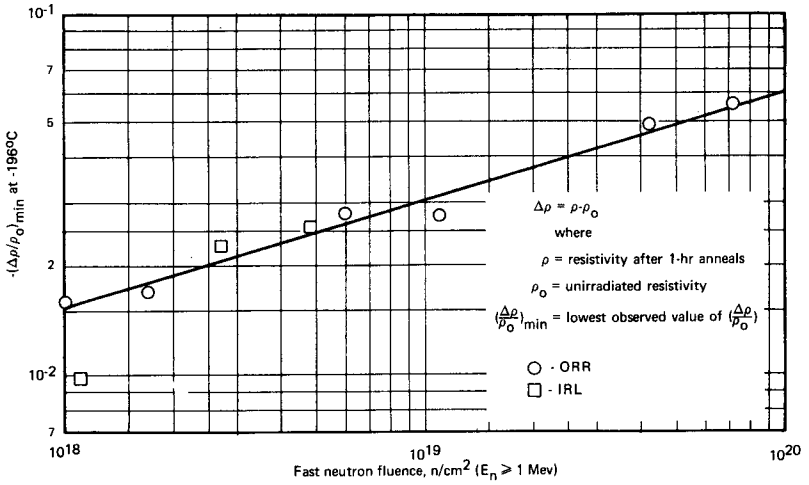

Fig. 2.19 — Dependence of the fractional resistivity minimum, $(\Delta\rho/\rho_o)_{min}$, of irradiated A302B steels on the fast neutron fluence

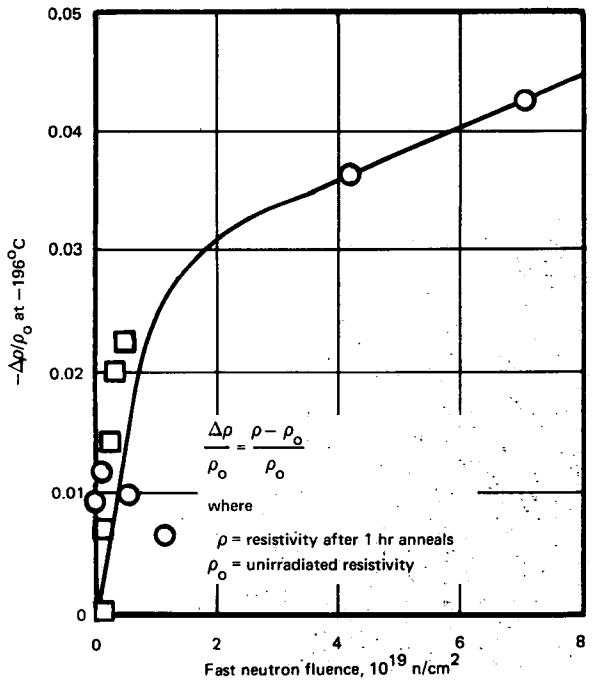

Fig. 2.20 — Fractional decrease in resistivity of IRL and ORR irradiated A302B steel as a function of fast neutron fluence

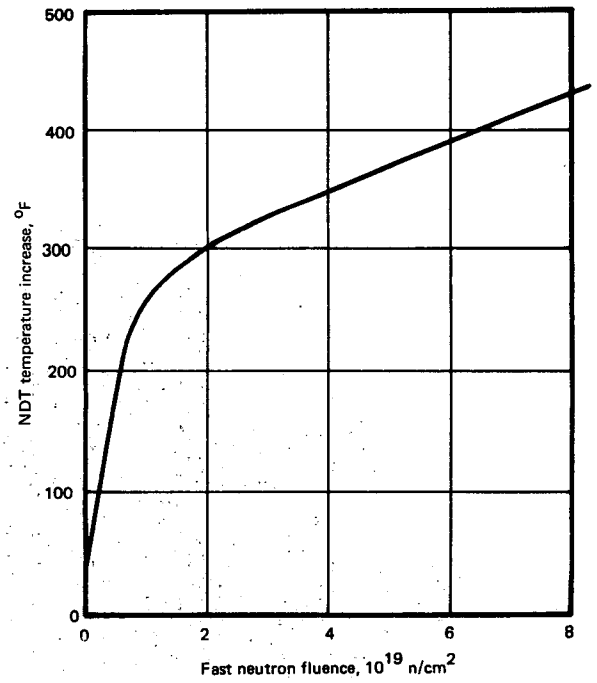

Fig. 2.21 — Increase in the nil ductility transition temperature[15] of irradiated A302B steel as a function of fast neutron fluence

TRANSMISSION ELECTRON MICROSCOPY (R. C. Rau, D. A. Woodford,* J. P. Smith, J. Moteff)

Previous results[13] on irradiated unstressed A-286 containing 0.001 and 0.010 weight percent natural boron indicated that all observable helium gas bubbles were associated with dislocations. There was no preference for bubbles to move to grain boundaries on post-irradiation thermal treatments up to 955 °C. To determine whether the combined effects of stress and temperature altered helium distributions, sections were cut from the stressed portion of the same specimens which had been creep-rupture tested at 660 °C and previously evaluated in the unstressed condition. The specimens were sectioned within 0.2 cm of the fracture and heat treated at 760°, 845°, and 955 °C. Examination of the sections from the as-tested specimens revealed very few bubbles, too few and too small in diameter to evaluate. The post-test heat-treated specimens, however, had many bubbles large enough to be evaluated. The size and size distribution appeared to be unaffected by the combined effect of stress and temperature; i.e., the results were the same as found on the specimens which were only thermally treated and not stressed. The size distribution as a function of boron content and anneal temperature is shown in Figure 2.22. There is no systematic difference between the stressed and unstressed sections taken from the specimens.

Figure 2.23 shows an area containing a grain boundary triple point and numerous matrix dislocation lines. Of significant interest are the dislocations leading into the grain boundaries; there appears to be no driving force for the helium on these dislocations to migrate to the boundary, although one would expect the dislocation to be a good diffusion pipe. Several small bubbles are present at the triple point. Figure 2.24 represents an area containing a rather high matrix bubble density compared to the few bubbles seen on the grain boundary. Significantly, all bubbles in the boundary also lie on dislocation lines within the boundary; these would probably impede dislocation movement within the boundary and thereby restrict grain boundary sliding.

The presence of shells with a high bubble density around certain precipitate particles was reported previously for A-286.[13] Recent investigations on another alloy, Hastelloy R-235 containing 50 ppm boron enriched in B^{10} isotope, revealed a similar post-irradiation microstructure. Figure 2.25a illustrates the relative number of atom displacements as a function of recoil distance for both the alpha-particle and lithium. Essentially all damage is produced at the end of the recoiling particle path. The relative number of displacements caused by the lithium is somewhat higher than for the alpha-particle. Based on these factors one would expect two relatively narrow damage bands containing numerous atomic displacements as shown schematically in Figure 2.25b. Both bands (shells) were observed in A-286 and Hastelloy R-235 as shown in Figure 2.26. Figure 2.26a shows shells around three separate precipitate [Ti(N, B)] particles. For two particles an inner and outer shell are apparent. The bubbles in the outer shell are probably helium bubbles precipitated on dislocations; bubbles on the inner shell could be helium or vacancy clusters. The highly damaged matrix could limit the normal range of an alpha-particle by minimizing channeling, or the high vacancy concentration resulting from the high damage state around the lithium atom may form large voids visible on post-irradiation heat treatment. Figure 2.26b shows a similar condition in Hastelloy R-235 but probably in a different stage of development; all that is observed are concentric dislocation shells. Higher-temperature annealing will presumably reveal voids or bubbles.

*General Electric Company, Materials and Processes Laboratory, Schenectady, New York.

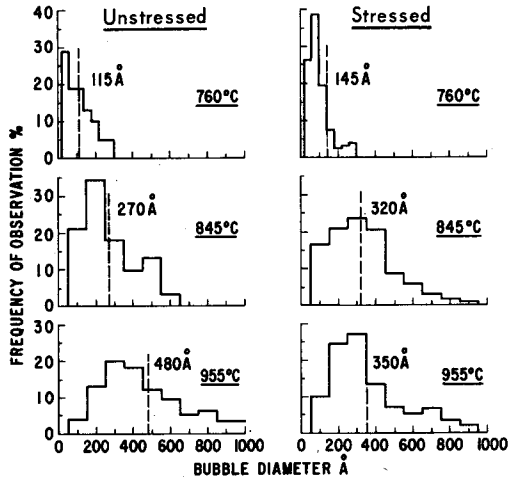

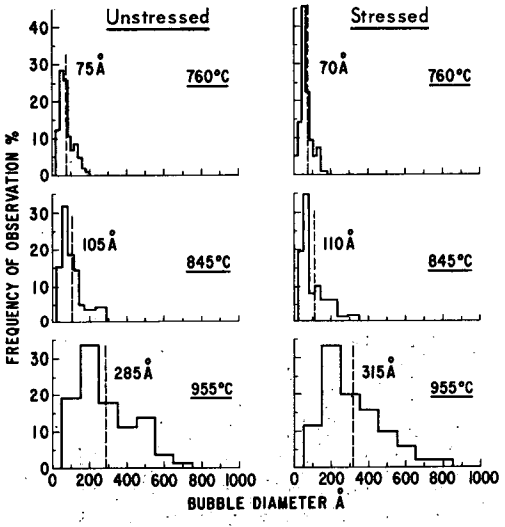

Fig. 2.22 — Size distribution of helium bubbles as a function of boron content and annealing temperature in stressed and unstressed A-286 alloy

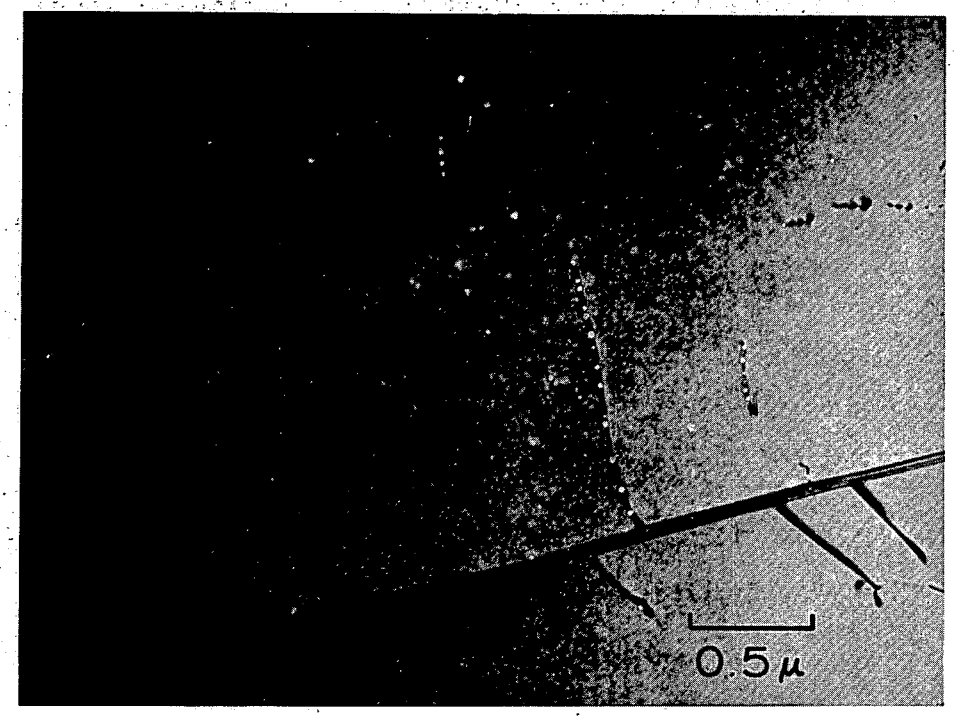

Fig. 2.23 – Transmission electron micrograph of irradiated A-286 showing helium bubbles on matrix dislocation lines and several small bubbles at the triple point

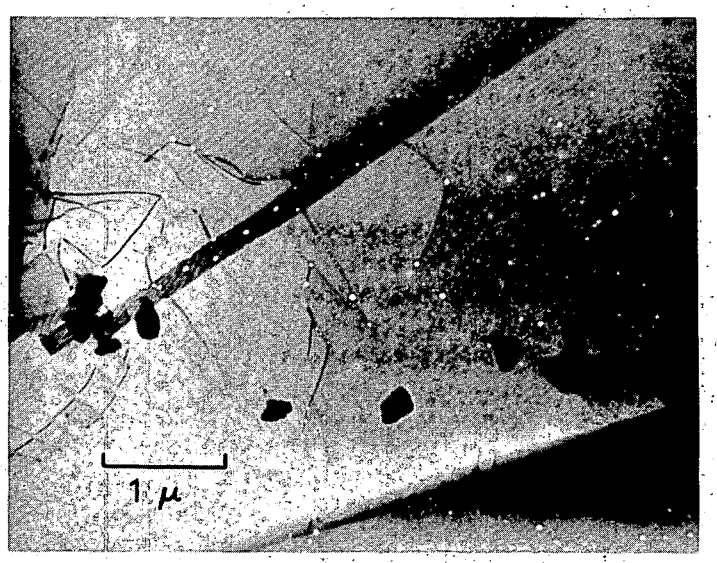

Fig. 2.24 – Transmission electron micrograph of irradiated A-286 showing bubbles attached to dislocation lines in the matrix and in the grain boundary

To fully explain radiation-induced changes in metals it is first necessary to describe deformation mechanisms of unirradiated alloys. An important phase of the current work is the examination of unirradiated specimens which have the same history as the irradiated specimens except for neutron exposure. Transmission electron microscope observation of unirradiated Hastelloy R-235 specimens indicates that deformation at 870°C was accompanied by the pairwise motion of dislocations through both the matrix and the coherent γ' particles.[14] A good example of a slip band containing paired dislocations in a low-stress region of a tested specimen is seen in the micrographs of Figure 2.27. As discussed previously,[15] this pairing is due to the creation and annihilation of an antiphase boundary by successive dislocations as they pass through the ordered γ' particles. This process retards the motion of the first dislocation and accelerates the motion of the second, causing them to draw together and move as pairs. The mobility of dislocations is largely controlled by the energy requirements for creating and annihilating an antiphase boundary; hence strengthening of coherent γ'-hardened alloys depends upon the distribution and volume fraction of γ' present.[16,17]

The effect of strain on the interaction of dislocations with γ' particles was examined in detail, by cutting foils from three different parts of the deformed region; deformation is defined as the reduction in cross-section area. This technique involved examining foils from sections deformed at 870°C to 1, 7, and 12 percent strain.

Figure 2.28a shows the microstructure in a foil taken from a region of relatively low strain (~1% reduction in area). Most γ' particles have lost coherency and are encircled by one or more dislocations. Figure 2.28b shows the microstructure in a region of intermediate strain, approximately 7 percent. At this strain level, all the γ' particles are encased in dislocation networks. The dislocation density within these networks, however, is lower than in those surrounding γ' in the high-strain (~ 12%) region, as shown in Figure 2.28c. Similar dislocation networks surrounding γ' particles were reported recently[18] in strained Inconel X-750, but were not discussed.

This stress-induced formation of dislocation networks at the interface between γ' particles and matrix is believed to arise from the pinching off of loops from moving dislocations which bow around and are forced past the particles, leaving a loop for each passing dislocation. Increasing deformation deposits additional loops at the interface, adding to the dislocation density within the networks. As this dislocation density increases, mutual repulsive forces between the dislocations within the networks make it more difficult to add further loops, and thus lead to a hardening effect in the alloy.

In regions of high-stress concentration, dislocations would be expected to bow around coherent γ' particles rather than to shear them if the retarding force on the leading dislocation, i.e., the antiphase boundary energy of the γ', were high enough. This is apparently true of Hastelloy R-235; no areas were observed which showed massive shearing of γ' particles by glide dislocations, as have been observed in other alloys by Copley and Kear[17] and Gleiter and Hornbogen.[19] The mode of dislocation immobilization in γ' precipitation hardening alloys is probably very sensitive to the alloy composition and heat treatment, since these factors influence the composition and degree of ordering of the γ' phase which in turn determine the antiphase boundary energy.

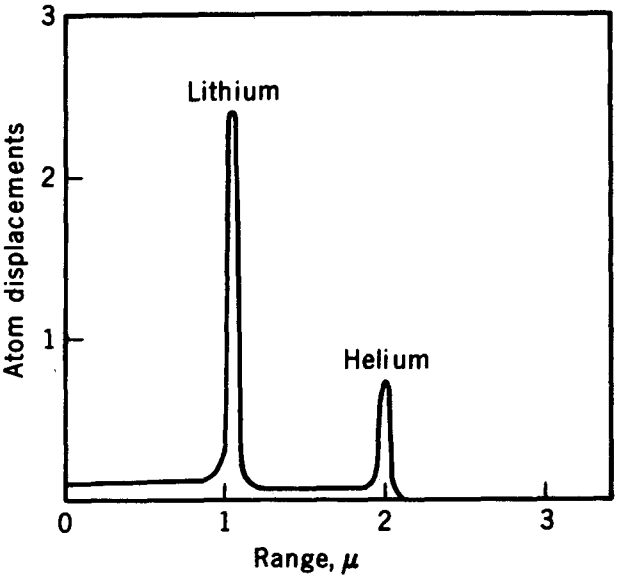

a. Relative displacement

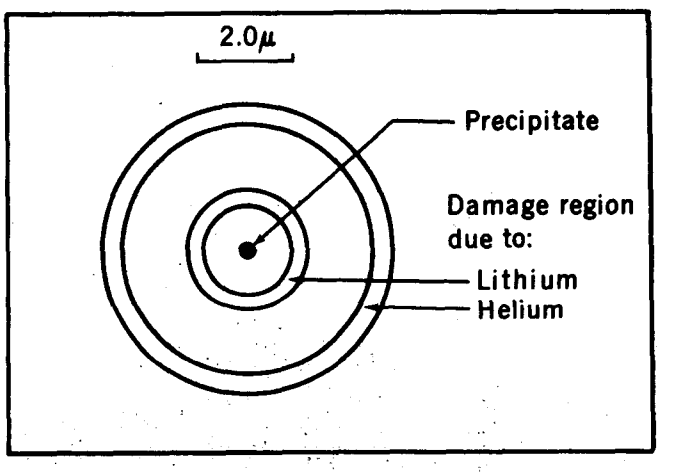

b. High-damage regions

Fig. 2.25 – Relative atom displacement and expected high-damage regions

In addition to the transmission electron microscopy discussed above, surface replication and electron microscopy is also being performed on these same Hastelloy R-235 specimens. Primary emphasis is being placed on the appearance of the structure immediately adjacent to the fracture, since past experience with similar alloys has shown that the microstructures in the unstressed condition are essentially identical before and after irradiation. Comparison of replicas from the stressed areas reveals significant differences between irradiated and unirradiated specimens, as illustrated in Figure 2.29. Of interest is the alignment of γ'

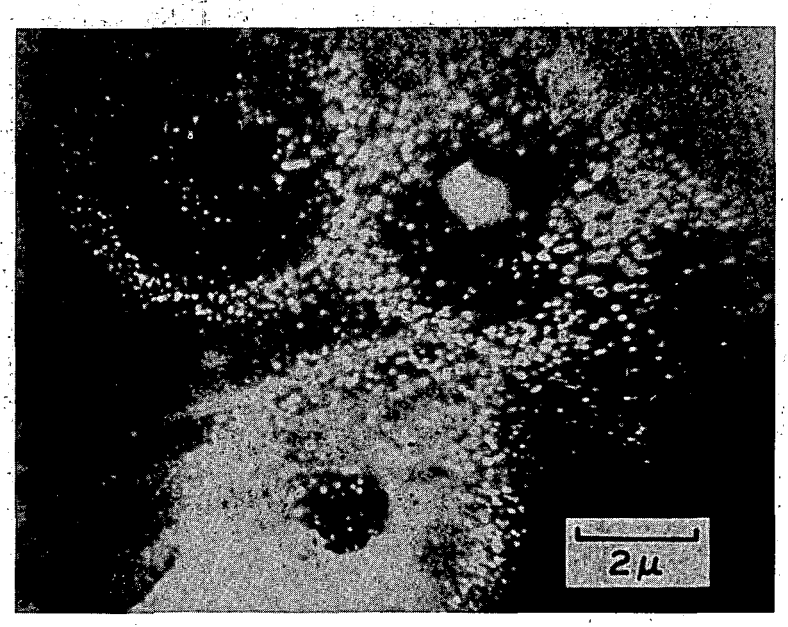

a. Helium bubbles around precipitate particles in irradiated A-286

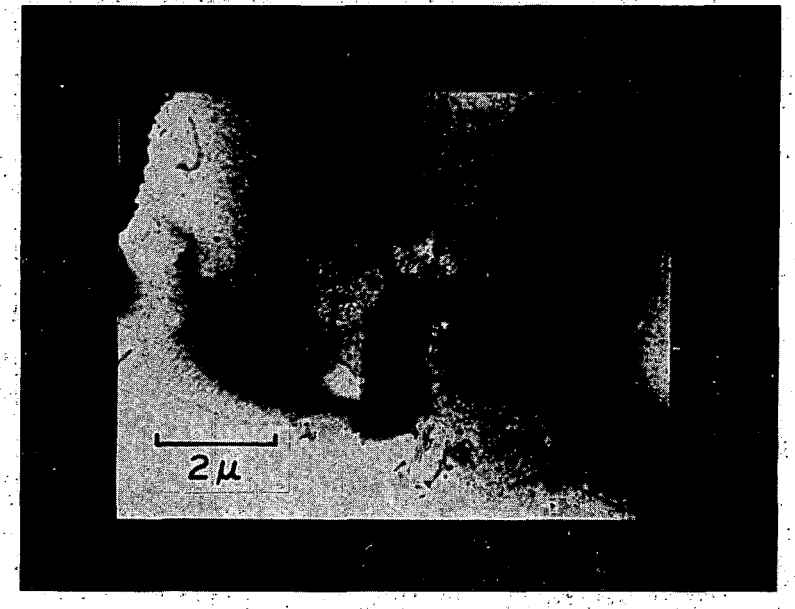

b. Shell of dislocations around precipitate particle in irradiated Hastelloy R-235

Fig. 2.26 — Helium bubbles and shell of dislocations around precipitate particles in irradiated A-286 and Hastelloy R-235

within each grain of the unirradiated specimen (Figure 2.29a); in the irradiated specimen (Figure 2.29b) there is no tendency for alignment. This rearrangement of γ' is apparently associated with grain deformation since the unirradiated specimen exhibited approximately 18 percent elongation at rupture, but the irradiated specimen elongated only 1 percent prior to fracture. No tendency for γ' alignment was observed in the unstressed, unirradiated specimen (thermally treated but not stressed) as shown in Figure 2.30, which supports the above conclusion that the alignment is strain induced.

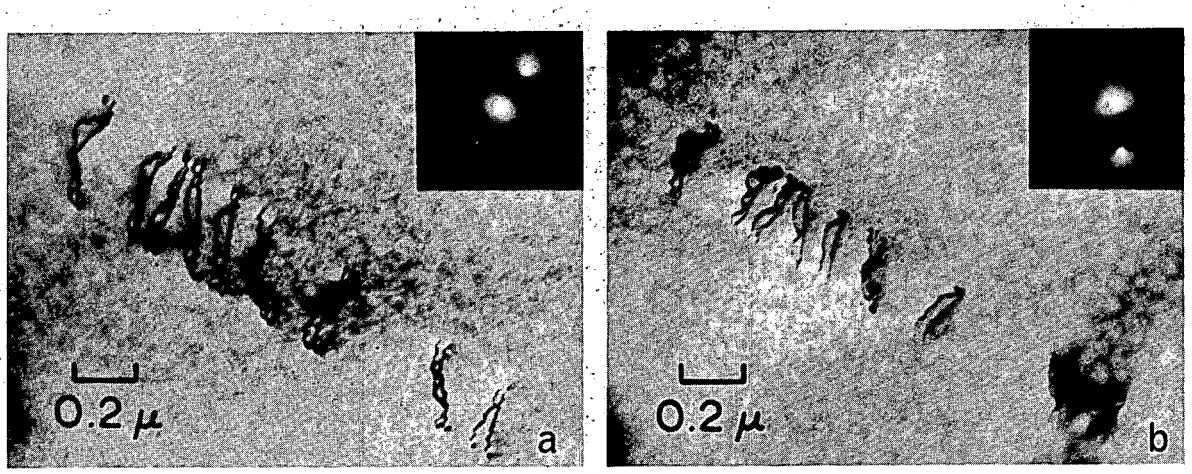

Fig. 2.27 — Slip band containing paired dislocations in low-stress region in Hastelloy R-235. (a) (111) reflection operating. (b) ($\bar{2}$00) reflection operating.

The microstructures in Figures 2.30a and b are from the same specimen; the difference is the etchant. The structure in Figure 2.30a was obtained by using Marbles etchant; 2.34b was obtained by electro etching with 10 percent H_3PO_4 in H_2O. The H_3PO_4 etchant gives a much better definition of γ' structure, particularly in grain boundaries, where it is shown in Figure 2.30b that virtually all carbide particles (matrix as well as grain broundary) are coated with γ'. This does not occur with the Marbles etchant. Further work will emphasize the H_3PO_4 etchant because it more truly illustrates the structure. The lack of alignment of γ' in the irradiated specimen indicates that grain deformation is reduced or eliminated by irradiation. It cannot be directly concluded that this indicates matrix stiffening, since it could be the result of premature grain boundary failure.

2.3 REFRACTORY METALS AND ALLOYS PROGRAM

Data are presented on the creep-rupture properties of molybdenum specimens of two carbon levels. Tests were performed on specimens irradiated to neutron fluences greater than 1×10^{20} n/cm^2 ($E_n \geq 1$ Mev) at 70°, 700°, and 1000°C. In several cases specimens were post-irradiation annealed at various temperatures and times to determine the effect of annealing on the neutron-induced changes in the creep-rupture properties.

Elevated-temperature and room-temperature tensile test results on niobium, Nb – 1Zr, and molybdenum are discussed. Post-irradiation anneals were given to a few specimens to study thermal hardening and recovery phenomena. Hot-hardness tests on several refractory metals and alloys were completed and are compared. The recovery of radiation-induced defects in molybdenum was investigated by isochronal resistivity studies. Studies continued on the effect of changes in defect structures upon the mechanical properties. An understanding of these effects will help to define the mechanisms of neutron-induced radiation changes in refractory materials.

CREEP-RUPTURE TESTING (F. Kingsbury, R. Treinen, J. Moteff)

Molybdenum Rod

A study of the effect of irradiation temperature on the creep-rupture properties of molybdenum at 750°C was conducted. The material used in this study contained a relatively high carbon content, approximately 220 ppm. The effect of irradiation temperature was studied on recrystallized, polycrystalline specimens irradiated at 70° (reactor-ambient), 700°, and 1000°C, to fast fluences in the range 1.3×10^{20} to 1.5×10^{21}

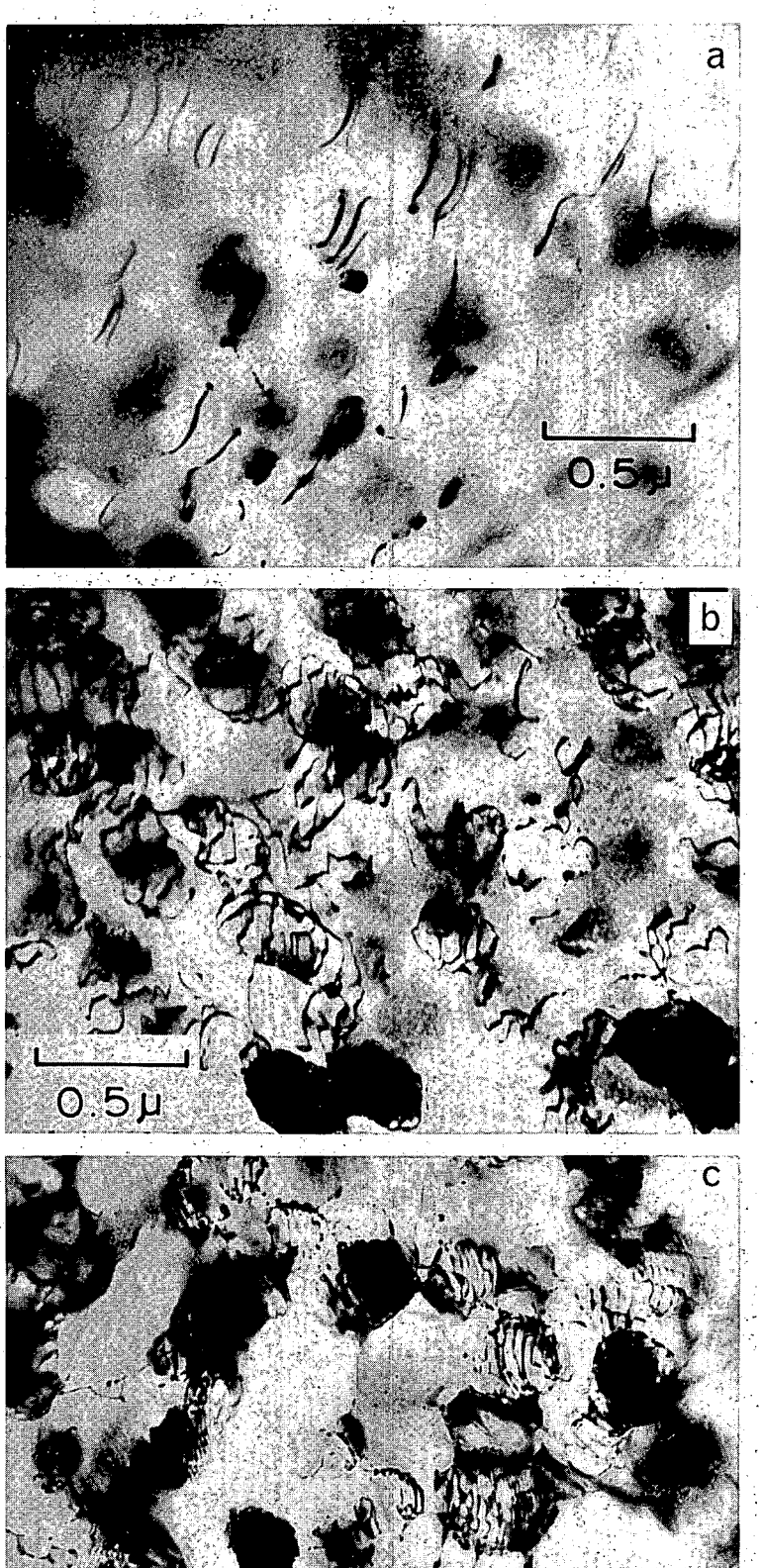

Relatively low-strain (~1%) region

Medium-strain (~7%) region

High-strain (~12%) region near fracture

Fig. 2.28 – Electron micrographs showing formation of dislocation networks around γ' particles as a function of strain in creep-tested Hastelloy R-235

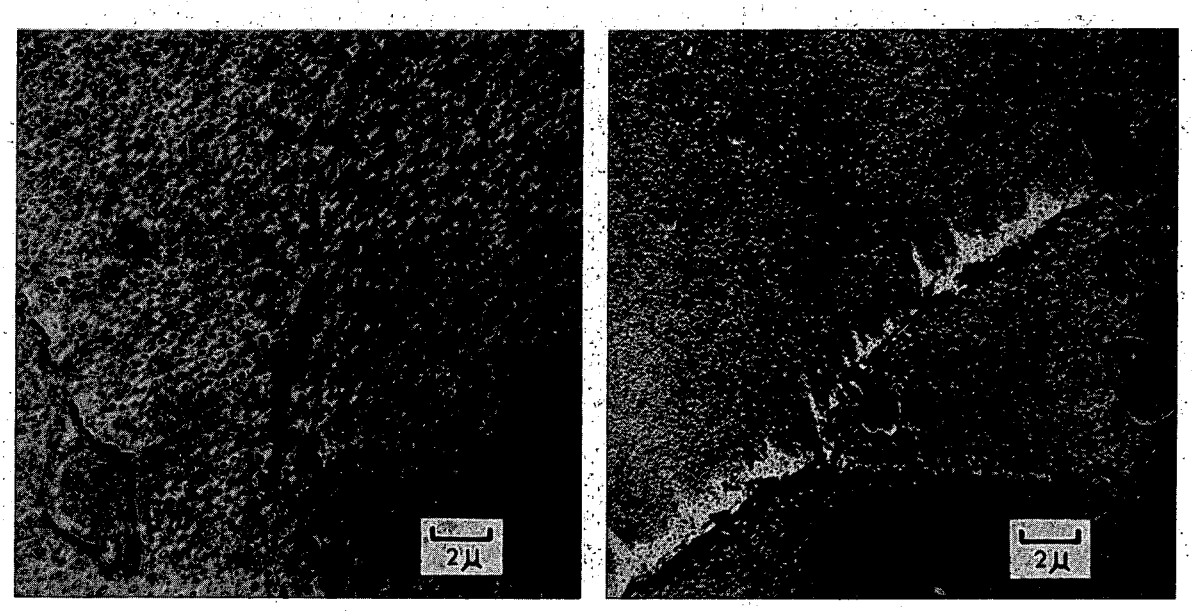

a. Unirradiated, 21% strain, t_R 200 hours

b. Irradiated, 0.6% strain, t_R 1 hour
$\phi_F = 2.5 \times 10^{19}$ n/cm^2 ($E_n \geqslant 1$ Mev)
$\phi_{Th} = 1.6 \times 10^{20}$ n/cm^2 at 70°C in ORR

Fig. 2.29 — Longitudinal sections of creep-rupture-tested Hastelloy R-235 immediately adjacent to fracture. Creep tested at 870°C, 14.1 kg/mm^2. (Marbles etchant)

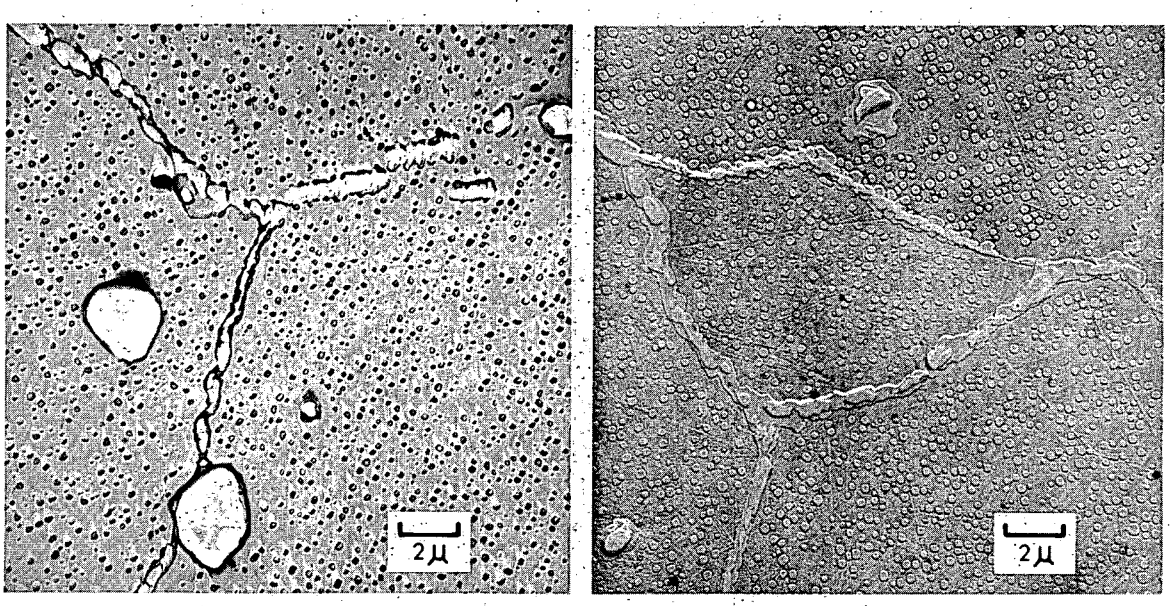

a. Marbles etchant

b. 10% H_3PO_4 electro-etch

Fig. 2.30 — Unirradiated Hastelloy R-235 exposed 200 hours at 870°C, unstressed

n/cm^2 ($E_n \geq 1$ Mev). All irradiated specimens were tested at a common initial stress level of 18.00 kg/mm^2 (Table 2.3). Two irradiated specimens were given 1-hour post-irradiation anneals at 1000°C. A test temperature of 750°C, based on the transmission electron microscope studies of Mastel and Brimhall,[20] was selected for this study. Their work showed that the observable spot and loop defect density in recrystallized molybdenum, irradiated at reactor-ambient temperature to a fast neutron fluence of about 1×10^{19} n/cm^2 ($E_n \geq 1$ Mev), decreased rapidly following post-irradiation anneals in the temperature region above 750°C. Thus it was thought that the irradiation of molydenum above and below this temperature ($\sim 0.35\ T_m$) would result in significant differences in post-irradiation creep-rupture properties. Creep-rupture properties of molybdenum at 750°C for specimens irradiated at three different temperatures are compared with a control specimen in Figure 2.31. Irradiation at the lower temperature (~ 70°C) resulted in the least effect on the time to rupture. There was, however, an initial period of "delayed" creep in which the creep rate remained very low for about 5 hours. The specimens irradiated at 700°C and 1000°C show a factor of 12 and 18 increase, respectively, in rupture life, with a slight decrease in ductility at the higher temperature. There is a relatively long second-stage creep behavior which increases with increasing irradiation temperature.

Two irradiated specimens were post-irradiation annealed at 1000°C in vacuum for 1 hour and creep-rupture tested. The effects of these anneals are shown in Figures 2.32 and 2.33. Annealing an ambient-temperature irradiated specimen altered the creep-rupture properties; the period of delayed creep was shortened, creep rate was reduced, and time to rupture was increased compared to the as-irradiated specimen. Changes produced by a 1000°C anneal in the creep properties of a 700°C irradiated specimen were not so pronounced. The minimum creep rate did not show a significant change, rupture life was increased by 25 percent.

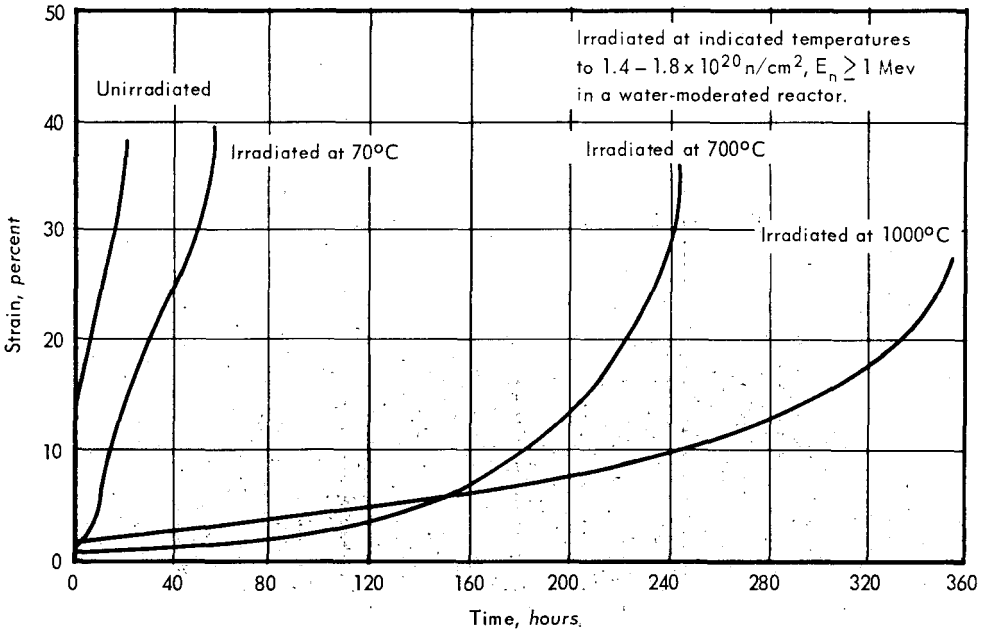

Fig. 2.31 – Creep-rupture properties of polycrystalline Mo at a test temperature of 750°C and an initial stress level of 18.00 kg/mm^2 following neutron irradiations at temperatures of 70°, 700°, and 1000°C

TABLE 2.3

MOLYBDENUM ROD[a] CREEP-RUPTURE TESTS AT 750°C

Specimen No.	Fluence, n/cm^2 Thermal	Fluence, n/cm^2 Fast ($E_n > 1$ Mev)	Irradiation Temperature, °C	Post-Irradiation Annealing	Stress, kg/mm^2	Stage I (Delayed) Creep Rate, sec^{-1}	Duration of Stage I Creep, hr	Stage II Creep Rate, sec^{-1}	Rupture Life, hr	Elongation,[b] %	Reduction in Area, %
High-Carbon (220 ppm) Rod[c]											
1606	None	None	–	None	14.00	–	–	5.7×10^{-8}	997.0	51.0	93.9
1615	None	None	–	None	17.00	–	–	5.4×10^{-7}	(120.2)[d]	–	–
1610	None	None	–	None	18.00	–	–	2.13×10^{-6}	20.4	39.5	95.7
1617	None	None	–	None	19.00	–	–	1.5×10^{-6}	35.6	40.3	94.3
1599	None	None	–	None	20.00	–	–	4.5×10^{-6}	8.68	38.4	92.4
1594	4.5×10^{20}	1.35×10^{20}[e]	~70	None	18.00	$\sim 1.4 \times 10^{-7}$	0.5–5	1.2×10^{-6}	56.1	40.4	92.8
1597	4.5×10^{20}	1.35×10^{20}[e]	~70	1000°C–1 hr–vac	18.00	$\sim 2.8 \times 10^{-7}$	0.5–1.5	8.3×10^{-7}	(87.5)[d]	(41.7)[d]	–
1591	2.7×10^{21}	1.5×10^{21}[f]	~70	None	18.00	$\sim 3.5 \times 10^{-8}$	~4–20	2.8×10^{-7}	253.4	44.6	94.3
1622	4.5×10^{20}	1.4×10^{20}[g]	~700	None	18.00	–	–	2.3×10^{-8}	244.1	37.6	94.4
1623	4.5×10^{20}	1.4×10^{20}[g]	~700	1000°C–1 hr–vac	18.00	–	–	2.1×10^{-8}	306.7	34.0	93.6
1612	4.3×10^{20}	1.3×10^{20}[h]	~1000	None	18.00	–	–	7.2×10^{-8}	355.1	31.1	95.2

[a]Specimens from 0.508-cm-diameter arc-cast Mo rod post-grind annealed at 1200°C for 1 hour in vacuum.
[b]Percent in 4.45-cm gage length.
[c]Heat KDM-10028, rod D.
[d]Specimen did not fracture; lever arm arrested against stop in latter portion of third-stage creep.
[e]Irradiation test 2-236 in ETR facility E-5NE.
[f]Irradiation test 2-234 in J-14NW facility.
[g]Irradiation test 2-154 in ETR facility E5SW during cycle 84.
[h]Irradiation test 2-136 in ETR facility E5NE during cycle 84.

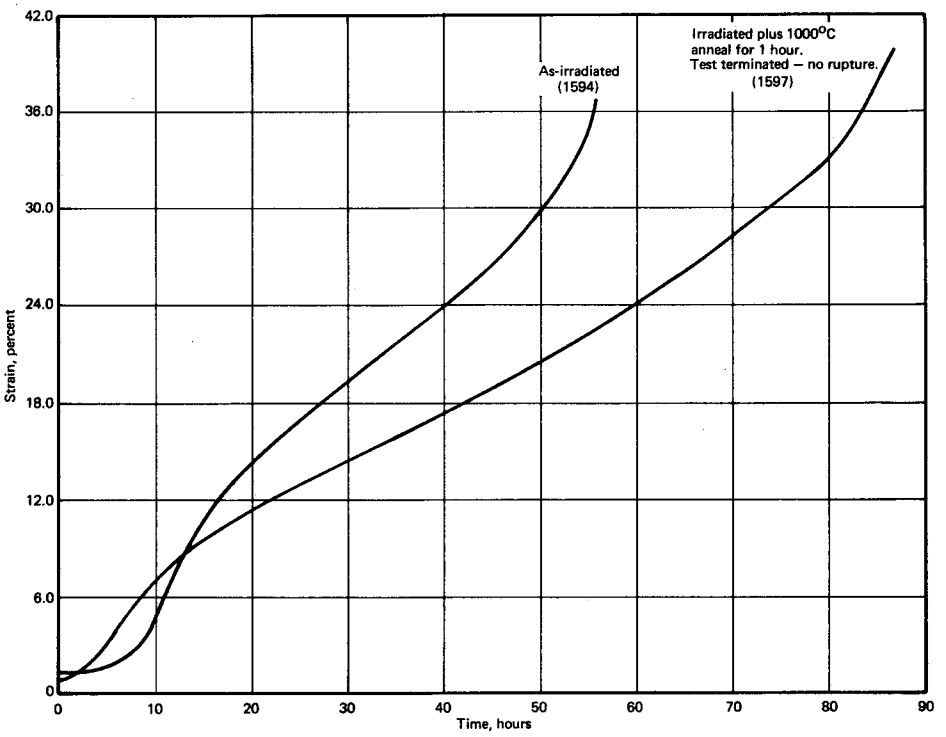

Fig. 2.32 — Effect of 1-hour 1000°C post-irradiation anneal on the creep-rupture properties of high-carbon Mo rod specimens irradiated at approximately 70°C to a fluence level of 1.35 x 10^{20} n/cm^2 ($E_n \geq 1$ Mev). Tests conducted at 750°C and 18.00 kg/mm^2.

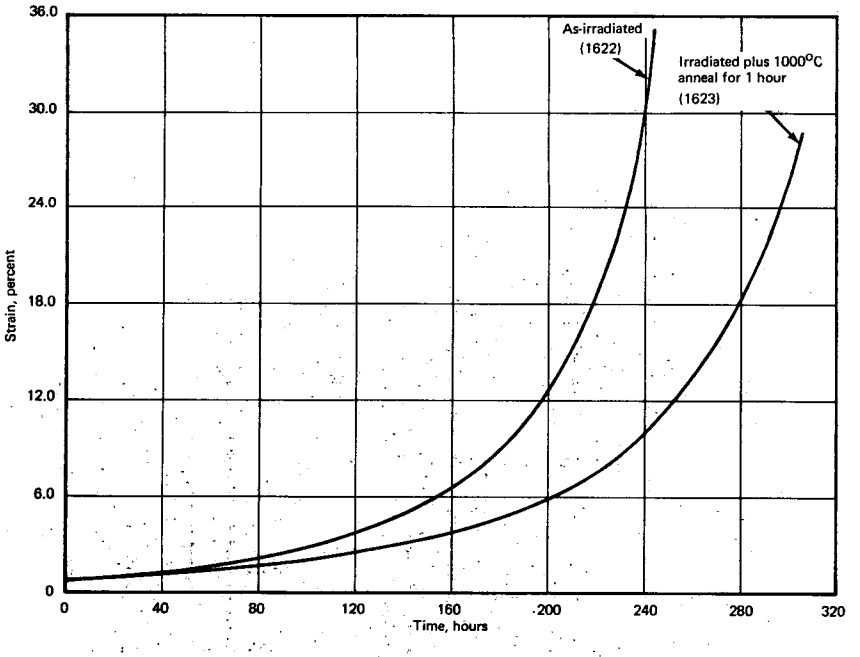

Fig. 2.33 — Effect of 1-hour 1000°C post-irradiation anneal on the creep-rupture properties of high-carbon Mo rod specimens irradiated at 700°C to a fluence level of 1.4 x 10^{20} n/cm^2 ($E_n \geq 1$ Mev). Tests conducted at 750°C and 18.00 kg/mm^2.

Specimen No. 1591 which was irradiated to a neutron fluence of 1.5×10^{21} n/cm^2 ($E_n \geq$ 1 Mev) at ambient temperature permits a comparison of the effect of neutron fluence. Compared to specimen No. 1594 (1.35×10^{20} n/cm^2), Figure 2.34, which was irradiated to a fluence an order of magnitude lower, specimen No. 1591 exhibited a factor of 4.6 increase in time to tupture and almost an order of magnitude decrease in creep rate. A portion of the greater rupture life was due to the increased length of the delayed creep period in the higher fluence specimen.

The differences in the creep characteristics between the various specimens can also be noted in the instantaneous creep rate versus plastic strain plots of Figures 2.35 through 2.37. Specimens irradiated at ambient temperature (Figure 2.35) all show a rapidly decreasing creep rate in the initial 0.2 percent strain. This is followed by a rapidly increasing creep rate which reaches a maximum value in the 2 to 6 percent strain region. After reaching this maximum value the creep rate decreases to the usually minimum second-stage creep rate. An expanded plot of the initial 1 percent strain (Figure 2.36) shows the ordering of the inflection points in the creep rates. The initial rate of decrease is approximately constant and the minimum value at the inflection point shifts to higher strain values at decreasing creep rates.

The creep-rate strain behavior of specimens irradiated at elevated temperatures (Figure 2.37) showed two differences in the characteristics compared to the ambient-temperature irradiated specimens. No maximum is observed in the creep rate following the initial inflection point. The three specimens exhibited an increase in creep rate with increasing strain following the initial decrease in creep rate. Irradiation at 1000°C did not produce the marked inflection at the minimum creep rate observed in the 700°C irradiated specimen or the 700°C irradiated specimen with the 1000°C post-irradiation anneal. The 700°C irradiated specimens have higher creep rates over a greater range of strain (and hence time) than the 1000°C irradiated specimen. The 1000°C post-irradiated annealed specimens also showed creep rates lower than the 700°C as-irradiated specimen. These

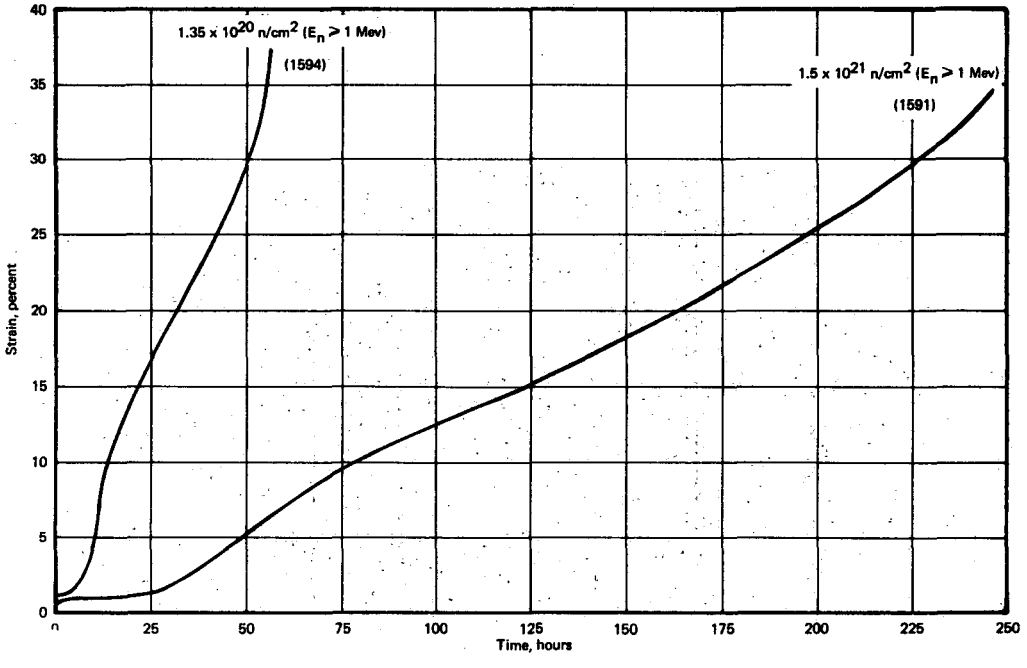

Fig. 2.34 — Creep characteristics of irradiated high-carbon Mo rod at two neutron fluence levels. Specimens irradiated at approximately 70°C and tested at 750°C and 18.00 kg/mm^2.

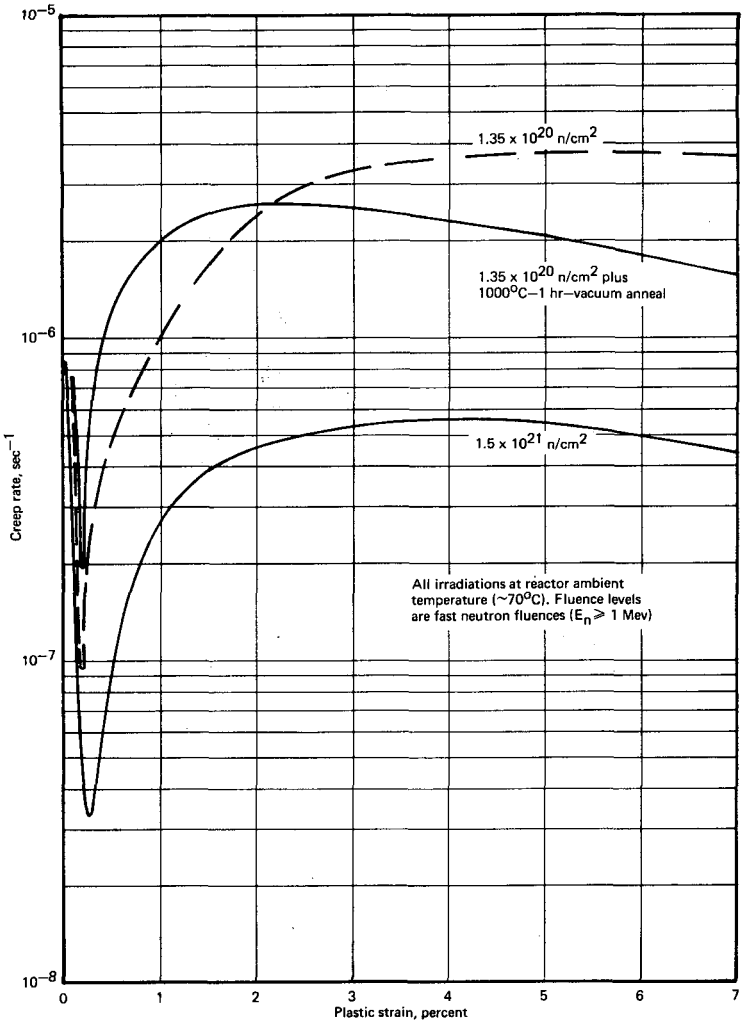

Fig. 2.35 — Creep rate versus plastic strain for ambient temperature irradiated high-carbon (200 ppm) Mo specimens tested at 750°C and 18.00 kg/mm^2

results suggest that some of the more stable defects are possibly formed between 700°C and 1000°C.

It is believed that the substructure, i.e., isolated dislocations, tangles, and subgrain boundaries formed during the initial straining establish the mode of deformation in creep. Structural studies are being conducted on these high-carbon molybdenum rod specimens, both optically and by transmission electron-microscope techniques. Initial electron microscope observations will be reported in a subsequent section.

Molybdenum Sheet

Creep-rupture testing of arc-cast molybdenum sheet was conducted to gain an understanding of the effect of changes in the defect structure produced by post-irradiation annealing on the mechanical properties. Preliminary tests[21] exhibited accelerated creep at 580°C and delayed creep at 700°C. Additional tests were conducted on material at two carbon levels, 205 ppm and 26 ppm, to confirm these results. Most tests were conducted at fixed stress levels and test temperatures; the irradiated specimens received various annealing treatments in the temperature range of 700° to 1600°C (0.34 to 0.65 T_m).

A composite strain – time plot for control, as-irradiated, and 750 °C post-irradiated low-carbon molybdenum specimens tested at 580°C is shown in Figure 2.38. The accelerated creep of the as-irradiated specimen is evident. The 750°C (0.36 T_m) anneal produced a lower creep rate and longer rupture life than the as-irradiated specimen, but did not fully restore the creep characteristics to the control values; hence the defects causing the accelerated creep were only partly removed at 750°C.

Tests at 700°C on low-carbon molybdenum included specimens which had two neutron fluence levels (Table 2.4). All irradiated specimens were tested at 17.50 kg/mm^2 except for specimens which had been post-irradiation annealed above 1400°C. These specimens were tested at lower stresses due to grain growth which had occurred in the annealing process. Originally all low-carbon specimens were annealed at 1200°C in vacuum for 1 hour following fabrication.

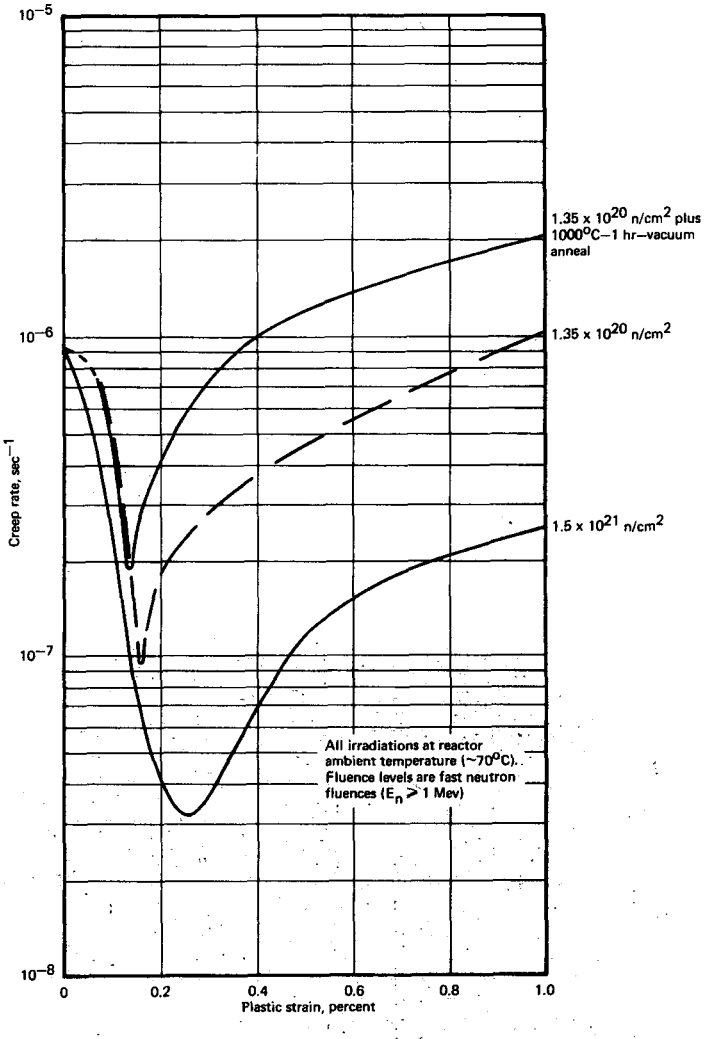

Fig. 2.36 – Creep rate versus plastic strain for irradiated high-carbon (200 ppm) Mo specimens tested at 750°C and 18.00 kg/mm^2

TABLE 2.4

LOW-CARBON MOLYBDENUM SHEET[a] TESTS AT 700°C

Specimen No.	Fluence, n/cm^2 Thermal	Fluence, n/cm^2 Fast ($E_n \geq 1$ Mev)	Post-Irradiation Annealing, °C	Stress, kg/mm^2	Stage I (Delayed) Creep Rate, sec^{-1}	Duration of Stage I Creep, hr	Stage II Creep Rate, sec^{-1}	Rupture Life, hr	Elongation,[b] %
2701		None	None	15.00	–	None	2.15×10^{-7}	237.1	43.5
2712		None	None	16.50	–	None	6.74×10^{-7}	96.8	47.9
2713		None	None	17.50	–	None	1.84×10^{-6}	37.5	58.3
2714		None	1200°C–1 hr–H_2	17.50	–	None	1.87×10^{-6}	33.3	51.2
2728		None	1200°C–1 hr–H_2	17.50	–	None	1.91×10^{-6}	31.0	50.3
2731		None	1450°C–1 hr–vac	14.50	–	None	8.03×10^{-7}	75.7	58.0
2716		None	1600°C–1 hr–H_2	13.0	–	None	1.15×10^{-6}	47.6	44.1
2700	9.3×10^{20}	3.1×10^{20}[c]	None	17.50	1.1×10^{-7}	2–16	5.78×10^{-6}	39.7	41.6
2702	9.3×10^{20}	3.1×10^{20}[c]	700°C–18 hr–H_2	17.50	1.52×10^{-7}	1–10	5.05×10^{-6}	37.6	40.4
2704	9.3×10^{20}	3.1×10^{20}[c]	800°C–1 hr–H_2	17.50	1.01×10^{-7}	0.5–8	4.53×10^{-6}	46.3	43.4
2705	9.3×10^{20}	3.1×10^{20}[c]	900°C–1 hr–H_2	17.50	1.11×10^{-7}	0.5–13	2.53×10^{-6}	69.8	45.0
2706	9.3×10^{20}	3.1×10^{20}[c]	1200°C–1 hr–H_2	17.50	–	None	3.75×10^{-7}	199.7	43.8
2718	3.9×10^{20}	1.2×10^{20}[d]	None	17.50	7.4×10^{-8}	0.5–18	6.47×10^{-6}	35.4	40.1
2723	3.9×10^{20}	1.2×10^{20}[d]	850°C–1 hr–H_2	17.50	6.4×10^{-8}	0.5–4	6.36×10^{-6}	30.6	–
2722	3.9×10^{20}	1.2×10^{20}[d]	900°C–1 hr–H_2	17.50	3.2×10^{-7}	0.5–8	3.24×10^{-6}	50.3	44.6
2721	3.9×10^{20}	1.2×10^{20}[d]	950°C–1 hr–H_2	17.50	2.0×10^{-7}	0.5–4	1.92×10^{-6}	74.1	40.5
2720	3.9×10^{20}	1.2×10^{20}[d]	1200°C–1 hr–H_2	17.50	–	None	1.02×10^{-6}	68.3	46.5
2725	3.9×10^{20}	1.2×10^{20}[d]	1450°C–1 hr–vac	14.50	–	None	3.0×10^{-7}	176.3	54.6
2726	3.9×10^{20}	1.2×10^{20}[d]	1600°C–1 hr–H_2	13.00	–	None	$\sim 3.1 \times 10^{-7}$	173.8	42.0

[a]Specimens from 0.05-cm commercial vacuum arc-cast Mo sheet (heat C-7722), post-grind annealed for 1 hour in vacuum at 1200°C (~30 micron grain size – DPH 193). Carbon content 26 ppm; O_2 – 18 ppm. All tests at constant load in H_2.

[b]Percent in 2.54-cm gage length.

[c]Irradiation test capsule ORM-46 in ORR facility F-2 at reactor-ambient temperature (~70°C).

[d]Irradiation test capsule GEFP2-235 in ETR facility E-5NE at reactor-ambient temperature (~70°C).

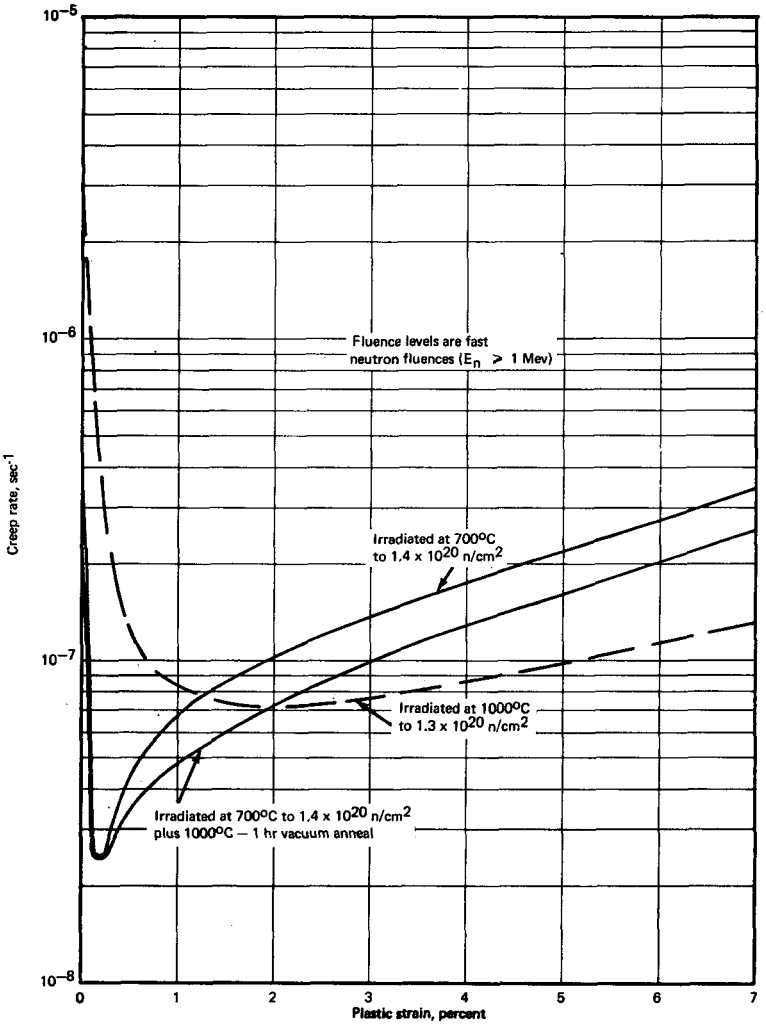

Fig. 2.37 – Creep rate versus plastic strain for elevated-temperature irradiated high-carbon (200 ppm) Mo specimens tested at 750°C and 18.00 kg/mm^2.

Specimens in the as-irradiated condition or post-irradiation annealed below 1000°C exhibited delayed creep (Table 2.4). The apparent length of this incubation period in which the creep rate is abnormally low tends to decrease upon annealing in the 700° to 950°C temperature range. The 700° to 800°C anneals produced only small changes in the creep rates or rupture times as shown (Figure 2.39) for the specimens irradiated to a fluence level of 3.1 x 10^{20} n/cm^2 ($E_n \geq 1$ Mev). Annealing at 900°C or 950°C produces little further changes in the incubation period but does decrease the steady-state creep rates and increase the times to rupture. A complete change in creep characteristics occurs upon annealing at 1200°C. The period of incubation (i. e., delayed creep) is not exhibited and the strain – time plots show the normal three stages of creep behavior. This is shown in Figure 2. 40 for specimens irradiated to 1. 2 x 10^{20} n/cm^2 ($E_n \geq 1$ Mev).

Tests at 700°C on specimens post-annealed above 1200°C are not directly comparable to the preceding results. Nevertheless, they may be compared to control specimens annealed at the same time and tested at the same stress level. Tests conducted on specimens annealed at 1450°C and 1600°C (0.60 and 0.65 T_m, respectively) did not show delayed

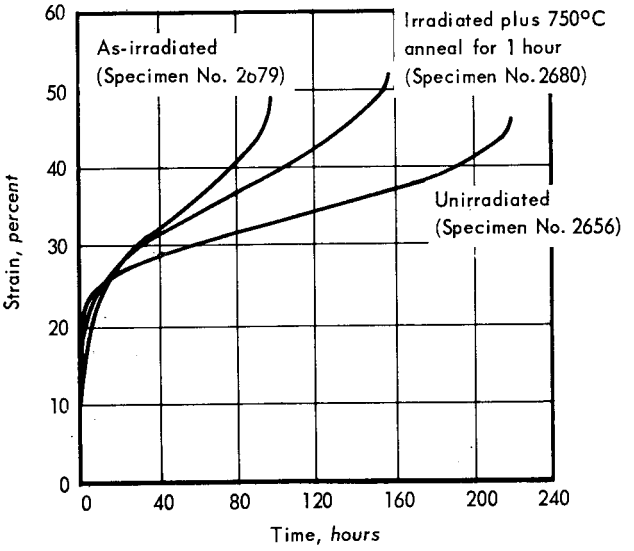

Fig. 2.38 — Effect of 750°C post-irradiation anneal on the accelerated creep of irradiated low-carbon molybdenum. Tests conducted at 580°C and 19.40 kg/mm^2 on sheet specimens irradiated at reactor ambient temperature to a fluence level of 4.8 x 10^{18} n/cm^2 ($E_n \geq 1$ Mev).

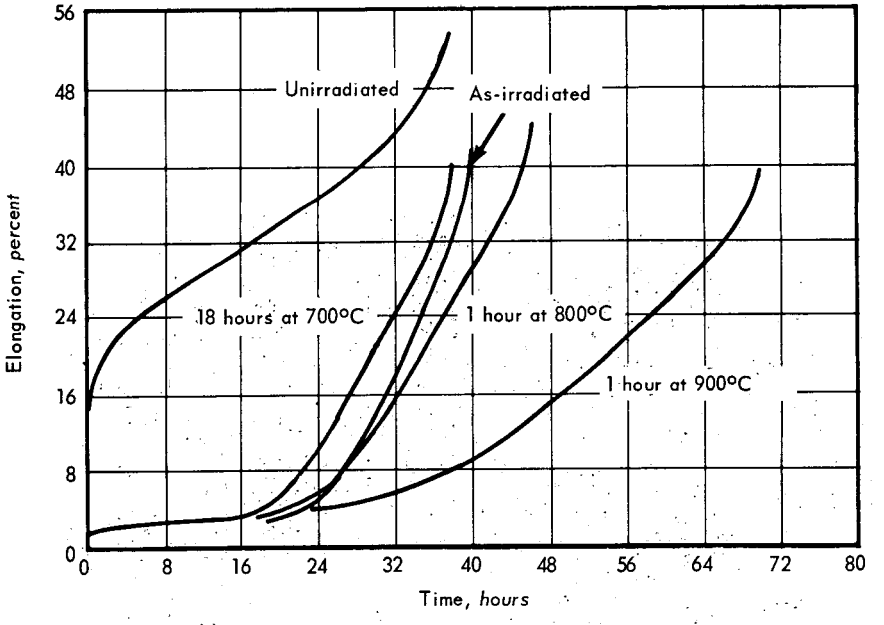

Fig. 2.39 — Effect of post-irradiation anneals at 700°, 800°, and 900°C on the creep properties of low-carbon molybdenum. Tests conducted at 700°C and 17.50 kg/mm^2 on sheet specimens irradiated at reactor ambient temperature to a fluence level of 3.1 x 10^{20} n/cm^2 ($E_n \geq 1$ Mev)

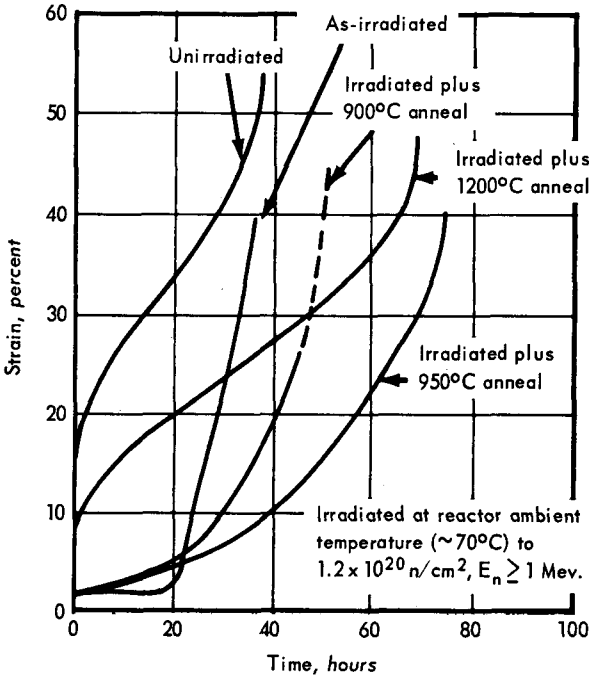

Fig. 2.40 – Effect of post-irradiation anneals at 900°, 950°, and 1200°C on creep properties of low-carbon Mo. Tests conducted at 700°C and 17.50 kg/mm^2 in a hydrogen atmosphere. Anneals performed at indicated temperatures for 1 hour in a hydrogen atmosphere.

creep. Pronounced neutron-induced strengthening still remains under these test conditions, as can be seen in the 1600°C annealed specimens, Figure 2.41.

A limited number of creep tests were also conducted at 700°C on high-carbon (~200 ppm) molybdenum specimens to observe the possible effect of particle – defect interaction on creep behavior. The differences in the two grades of material can be seen in the microstructures. The high-carbon molybdenum exhibited a dense, equiaxed, recrystallized grain structure with randomly distributed carbide particles. The particles were generally small but a few larger carbides were observed. Several larger carbides appeared to have voids associated with the ends of the particles (Figure 2.42). In contrast to the high-carbon molybdenum sheet, the low-carbon molybdenum microstructure (Figure 2.43) consisted of single-phase grains with no carbides observable at a magnification of 600X. The grain size of the low-carbon material was slightly larger (30-micron versus 22-micron grain sizes in the high-carbon Mo). The grains in the low-carbon material tended to be elongated in the direction of rolling.

A composite strain – time plot for the results of high-carbon molybdenum tests given in Table 2.5 is shown in Figure 2.44. The 1200°C annealed specimen exhibited no incubation period; creep rate was reduced significantly and rupture life increased 37 percent compared to the as-irradiated specimen. The 900°C anneal tended to remove the incubation period and produced a longer rupture life than the as-irradiated or 1200°C post-irradiation annealed specimen. This effect is believed related to the thermal hardening generally observed in tensile tests of irradiated body-centered cubic (bcc) materials following elevated-temperature anneals. In the present case, the thermal hardening can be related to rupture times (rupture strength) rather than to tensile strength.

The differences in the creep characteristics of the high-carbon molybdenum specimens can be readily observed in the instantaneous creep rate versus time plots of Figure 2.45.

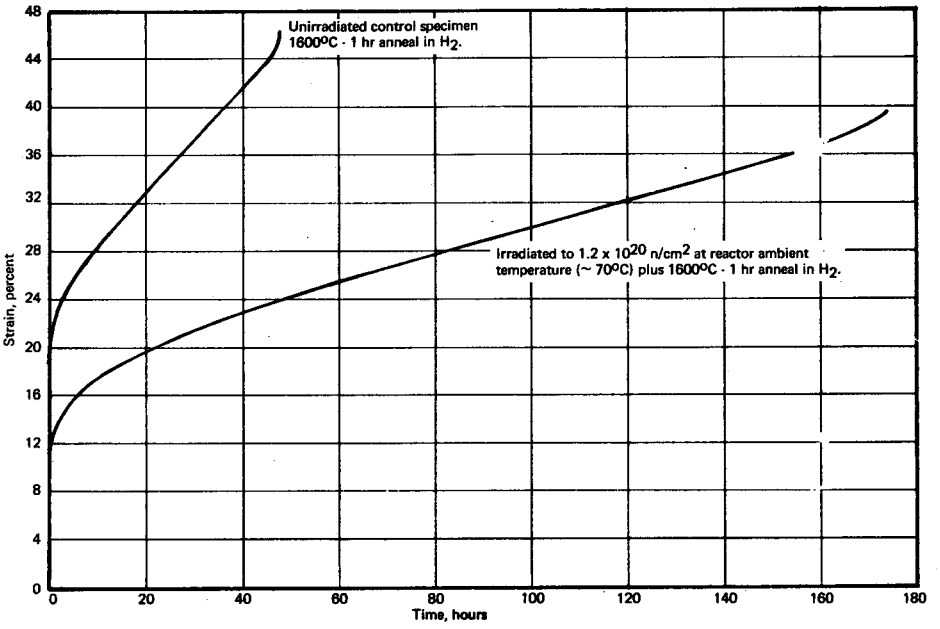

Fig. 2.41 — Strain versus time curves for low-carbon (26 ppm) Mo sheet specimens tested at 700°C and 17.50 kg/mm^2 in hydrogen.

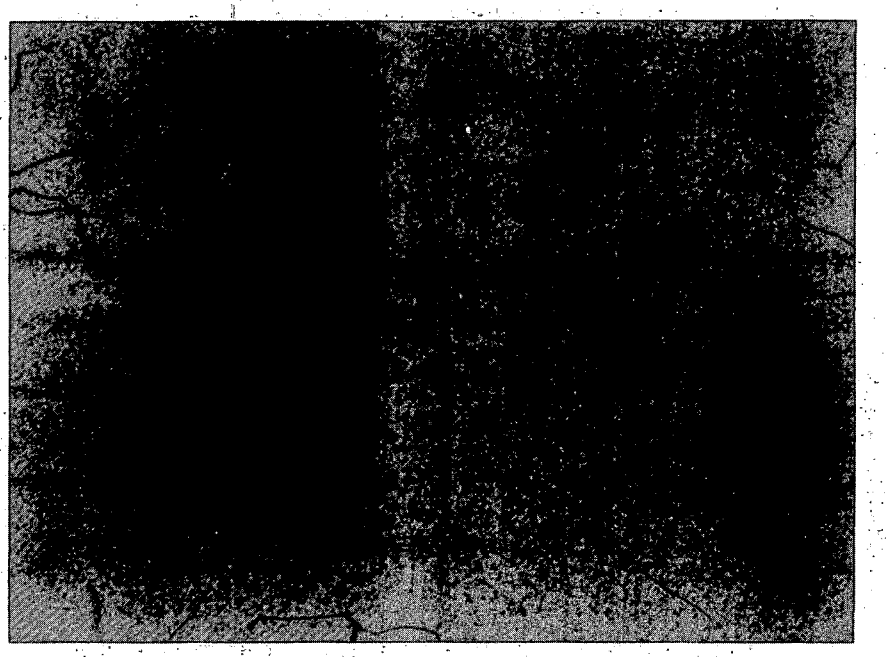

Fig. 2.42 — Photomicrograph of high-carbon (205 ppm) Mo sheet, heat C-6605, annealed at 1200°C for 1 hour in vacuum (Neg. 10280, 500X)

Fig. 2.43 – Photomicrograph of low-carbon (26 ppm) Mo sheet, heat 7722, annealed at 1200°C for 1 hour in vacuum (Neg. 10316, 250X)

TABLE 2.5

MOLYBDENUM SHEET CREEP RUPTURE TESTS AT 700°C AND 20.00 kg/mm^2

Specimen No.[a]	Condition	Post-Irradiation Anneal	Stage-I (Delayed) Creep Rate, sec^{-1}	Stage-I Creep Period, hr	Stage-II Creep Rate, sec^{-1}	Rupture Life, hr	Elongation,[b] %
2103	None	None	–	–	6.09×10^{-7}	118.9	49.2
2122	Irradiated[c]	None	$\sim 2.8 \times 10^{-8}$	1 to 10	4.11×10^{-7}	180.5	46.8
2126	Irradiated[c]	1200°C for 1 hr in H_2	–	–	2.6×10^{-7}	229.8	41.3
2127	Irradiated[c]	900°C for 1 hr in H_2	$\sim 2.8 \times 10^{-8}$	1 to 5	2.25×10^{-7}	271.4	43.1

[a]Specimens from 0.05-cm-thick commercial vacuum arc-cast Mo sheet (heat C 6605) post-grind annealed at 1200°C for 1 hour in vacuum (~22 micron grain size – DPH 191). Carbon content 205 ppm; O_2 content 3 ppm. All tests at constant load in hydrogen.
[b]Percent in 2.54-cm gage length.
[c]Irradiation test ORM-38 in ORR facility A-2 at reactor ambient temperature (~70°C) to a fluence of 1.1×10^{20} n/cm^2 ($E_n \geq 1$ Mev); thermal fluence of 5.2×10^{20} n/cm^2.

Normal creep-rate curves are exhibited by the unirradiated and 1200 °C annealed specimens; the 1200 °C curve is displaced into the lower creep-rate regions. The 1-hour anneal at 1200 °C probably did not remove all the radiation-induced defects (possible stable vacancy clusters). This view is supported by the results of the 1600 °C anneal in the low-carbon molybdenum test data. The lower creep rate following the 1200 °C anneal reflects dislocation interaction with the remaining defects.

The curves for as-irradiated and 900 °C annealed specimens show the nature of the changes in creep rate during the incubation and early stages of creep. The as-irradiated specimen shows a maximum in the creep-rate curve (at ~ 40 hours) following the initial rapid decrease in creep rate (delayed creep). This maximum is not observed in the 900 °C post-irradiation annealed specimen, and the specimen tends to show a continuous increase in creep rate following the delayed creep stage.

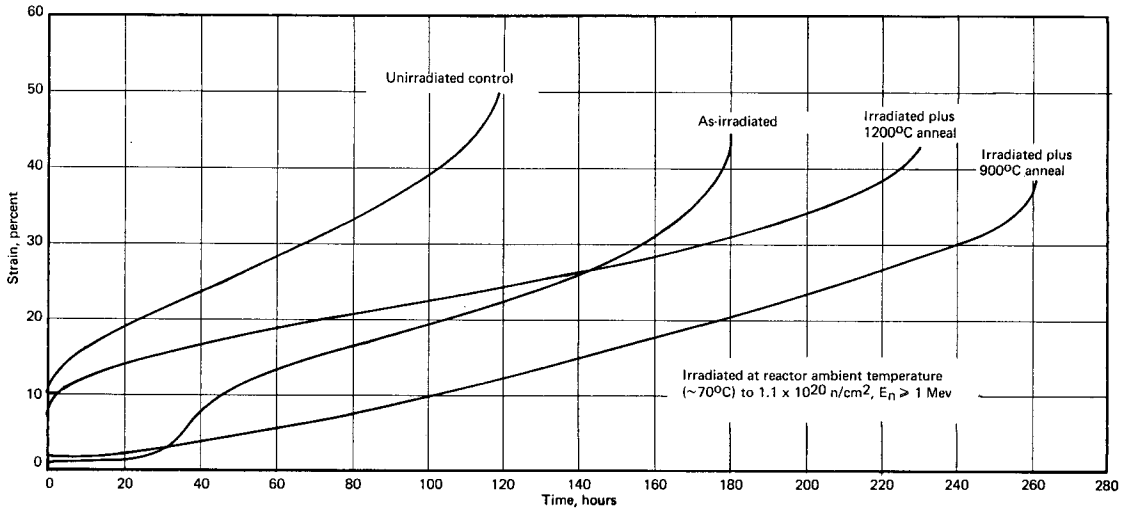

Fig. 2.44 – Effect of post-irradiation anneals at 900°C and 1200°C on creep properties of high-carbon Mo. Tests conducted at 700°C and 20.00 kg/mm^2 in a hydrogen atmosphere. Anneals performed at indicated temperature for 1 hour in hydrogen.

In general, the results between the low-carbon and high-carbon molybdenum sheet series of tests show agreement when compared at a similar fast-neutron fluence. The major difference between the two series exists in the effects of 900 °C and 1200 °C post-irradiation anneals. The 1200 °C anneal in the low-carbon molybdenum test produced a longer rupture life than the 900 °C anneal; the opposite was true in the high-carbon molybdenum. The temperature of maximum thermal hardening (i. e., longer time to rupture) is probably related to the carbon content since the fluence, grain size, hardness, and basic compositions of the two grades of molybdenum were very similar.

Fracture Examinations

Fracture areas of selected 700 °C creep-rupture tested specimens were examined metallographically to determine possible differences between the microstructure of the unirradiated, irradiated, and post-irradiation annealed specimens. In addition to the basic parameter of post-irradiation annealing temperature, the examination included a consideration of the two carbon content levels, 26 ppm and 205 ppm.

In general, the examinations did not reveal basic differences in fracture behavior between the various conditions. The basic difference between the two carbon levels at the immediate fracture tip was the presence of elongated voids associated with the carbide particles in high-carbon molybdenum. These voids were previously observed in the original material (Figure 2.42) but they were extremely small and localized. Nevertheless, the presence of the elongated voids did not impair the fracture ductility nor change the mode of fracture. The excellent ductility of the matrix, even in the as-irradiated specimens, is apparently controlling flow and fracture behavior. Fractures were all transgranular (Figure 2.46) and were accompanied by a relatively large amount of local plastic deformation (necking down to almost a knife edge).

Microstructures of regions away from the immediate fracture area varied considerably between the low-carbon and high-carbon molybdenum materials. Three differences were

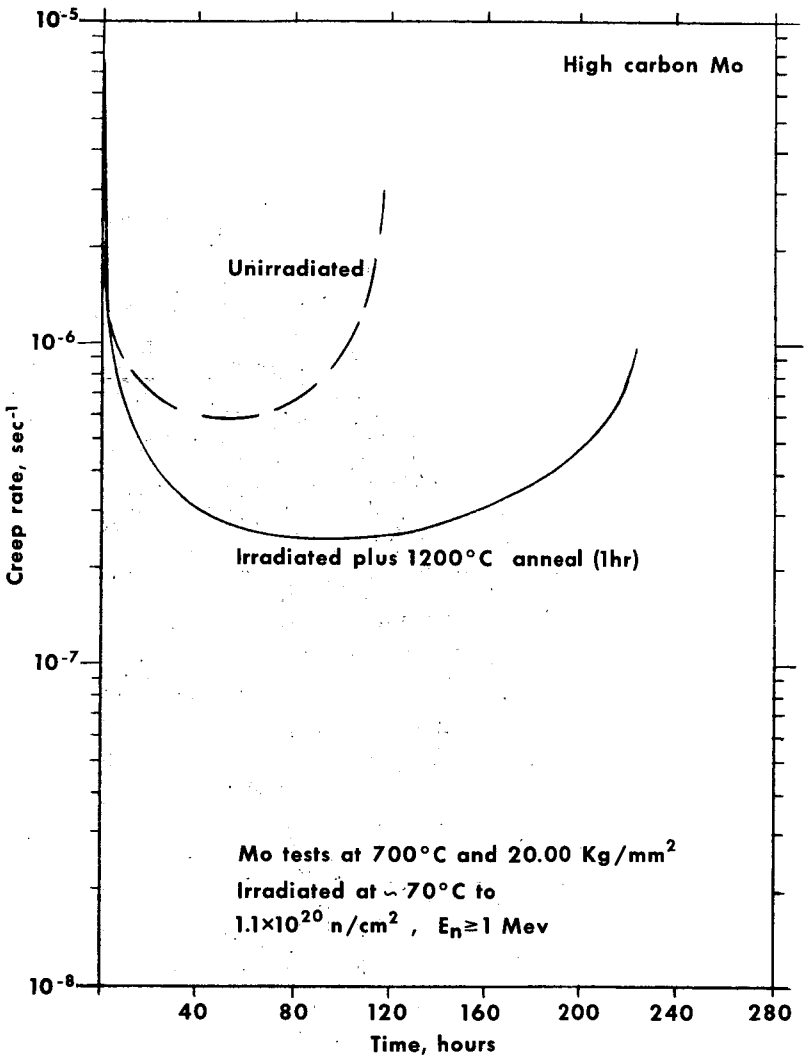

a. Unirradiated and 1200°C post-irradiation annealed specimens (AS-746K)

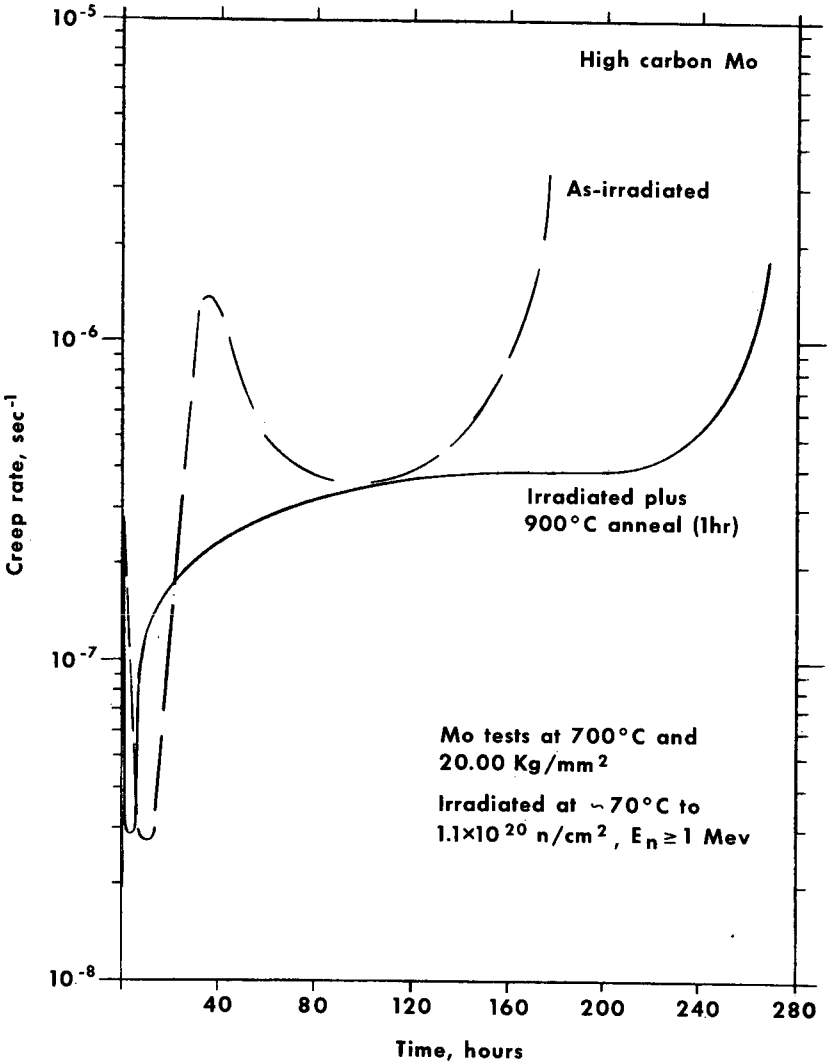

b. As-irradiated and 900°C post-irradiation annealed specimens (AS-746L)

Fig. 2.45 — Creep rate versus time curves for high-carbon Mo specimens tested at 700°C and 20.00 kg/mm² in hydrogen

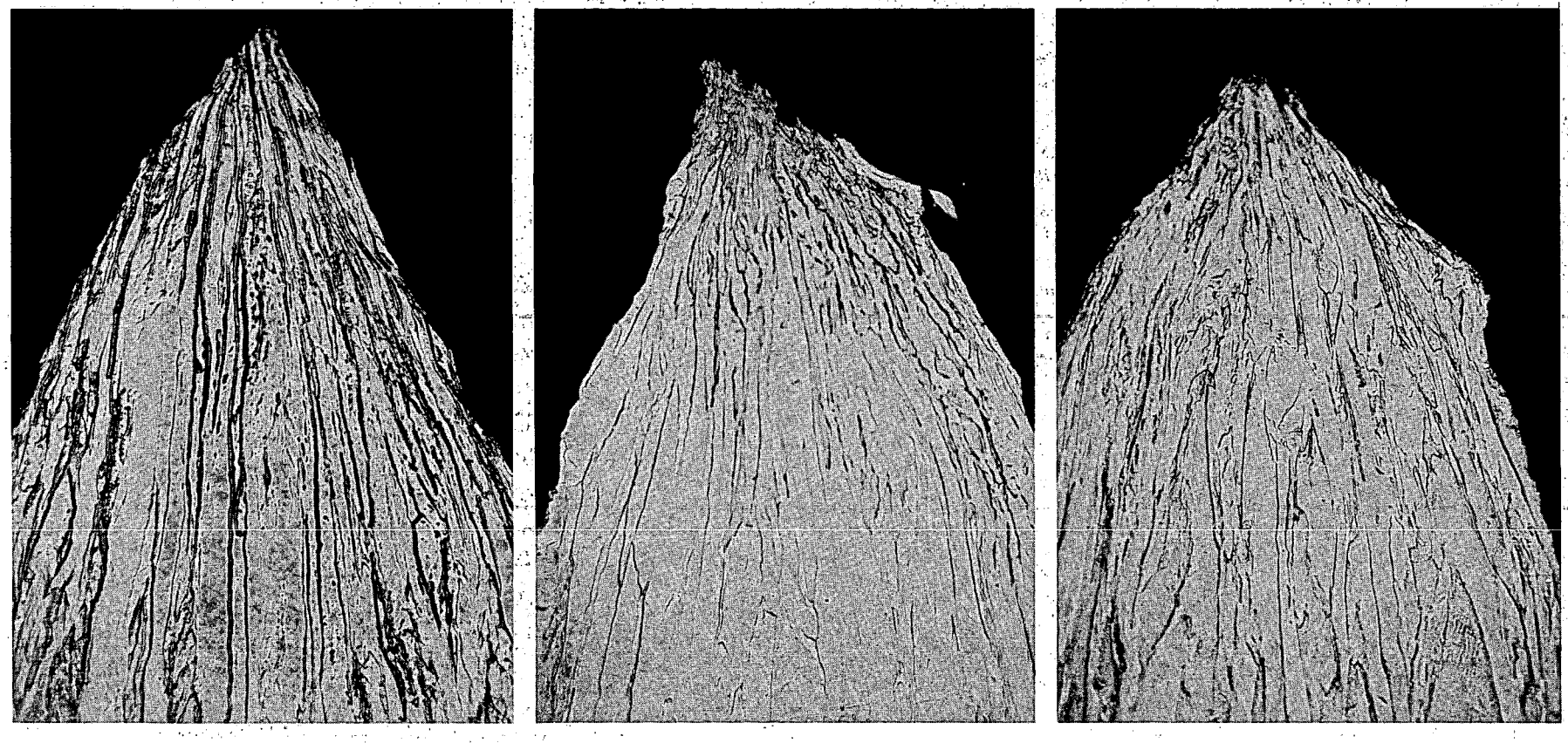

Unirradiated (Neg. R-2260)

As-irradiated – 1.2 x 10^{20} n/cm^2; $E_n \geq 1$ Mev (Neg. R-2250)

Irradiated (1.2 x 10^{20} n/cm^2) plus post-irradiation anneal at 1200°C for 1 hour (Neg. R-2254)

Fig. 2.46 – Photomicrographs of fracture area of low-carbon Mo sheet specimens creep-rupture tested at 700°C and 17.50 kg/mm^2 (500X)

noted: (1) A much finer plastically deformed grain size (Figure 2.47) in the high-carbon molybdenum due to differences in the grain sizes of the two original recrystallized molybdenum materials, (2) a considerably heavier density of low-angle grain boundary substructure in the high-carbon molybdenum, and (3) a concentration of relatively massive angular carbides in the high-carbon molybdenum (Figure 2.48a). Only a trace of carbides was noted in the low-carbon material (Figure 2.48b) and none of this carbide compared in size or shape to the chunky highly friable type present in the high-carbon molybdenum.

The grain growth which occurred in the 1600°C annealing of the low-carbon molybdenum is quite evident in the irradiated and unirradiated microstructures (Figure 2.49). When viewed at a higher magnification (Figure 2.50) the microstructure shows a relatively carbide-free matrix with agglomerated larger carbides distributed both intergranularly and intragranularly. The isolated particles of intragranular carbides are probably the result of grain boundary migration away from the particles in the grain growth process.

HOT HARDNESS (J. L. Kamphouse, J. Moteff)

Warm-Worked Tungsten

The objective of the hot-hardness study of warm-worked and irradiated tungsten was to determine the effect of substructure on the generation of radiation-induced defects as measured by changes in the hot hardness. Four specimens were prepared, each from sections of 73 percent and 98 percent warm-worked 0.51-mm-thick tungsten sheet. Two specimens of each worked condition were recrystallized at 1760°C for 1 hour in hydrogen. One specimen of each of the four conditions (73% worked, 73% worked plus recrystallization, 98% worked, and 98% worked plus recrystallization) was irradiated at reactor-ambient temperature in the ORR Rabbit 14 facility to a fluence level of 4.1×10^{19} n/cm^2 ($E_n \geq 1$ Mev). One specimen of each of the original unirradiated four conditions was used for comparison.

As shown by the microhardness increment fraction curves of Figure 2.51, 73 percent worked and recrystallized material and the 98 percent worked and recrystallized material showed about the same radiation-induced hardening, primarily in the athermal component. The 73 percent warm-worked material showed much less radiation-induced hardening and the 98 percent worked material showed virtually no additional hardening.

Studies[22] on the influence of dislocations on the damage structure in neutron-irradiated ($\sim 7 \times 10^{18}$ n/cm^2, $E_n \geq 1$ Mev) molybdenum show that the spot density is about a factor of two greater in the annealed material than in the material deformed 50 percent prior to irradiation. Assuming that this type of spot defect contributes to the hardness of the irradiated tungsten, it is believed that the increase in spot density in the recrystallized tungsten and the relative ineffectiveness of the spot defects to further harden the worked tungsten may account for the greater radiation-induced hardening in the recrystallized material compared to that observed in the worked tungsten.

A series of isothermal anneals was performed on 98 percent warm-worked tungsten. Results presented in Figure 2.52 show some scatter in the data because some data were obtained from single indents rather than from an average of three indents as is customary when obtaining isochronal data. Because of this unavoidable data scatter at annealing times less than 10^3 seconds, a very accurate activation energy for recrystallization could not be obtained. An attempt was made to calculate the activation energy using the crosscut method,[23] and a value of 4.8 ev was obtained using data from specimens annealed at 1300°C and 1373°C as shown in Figure 2.52.

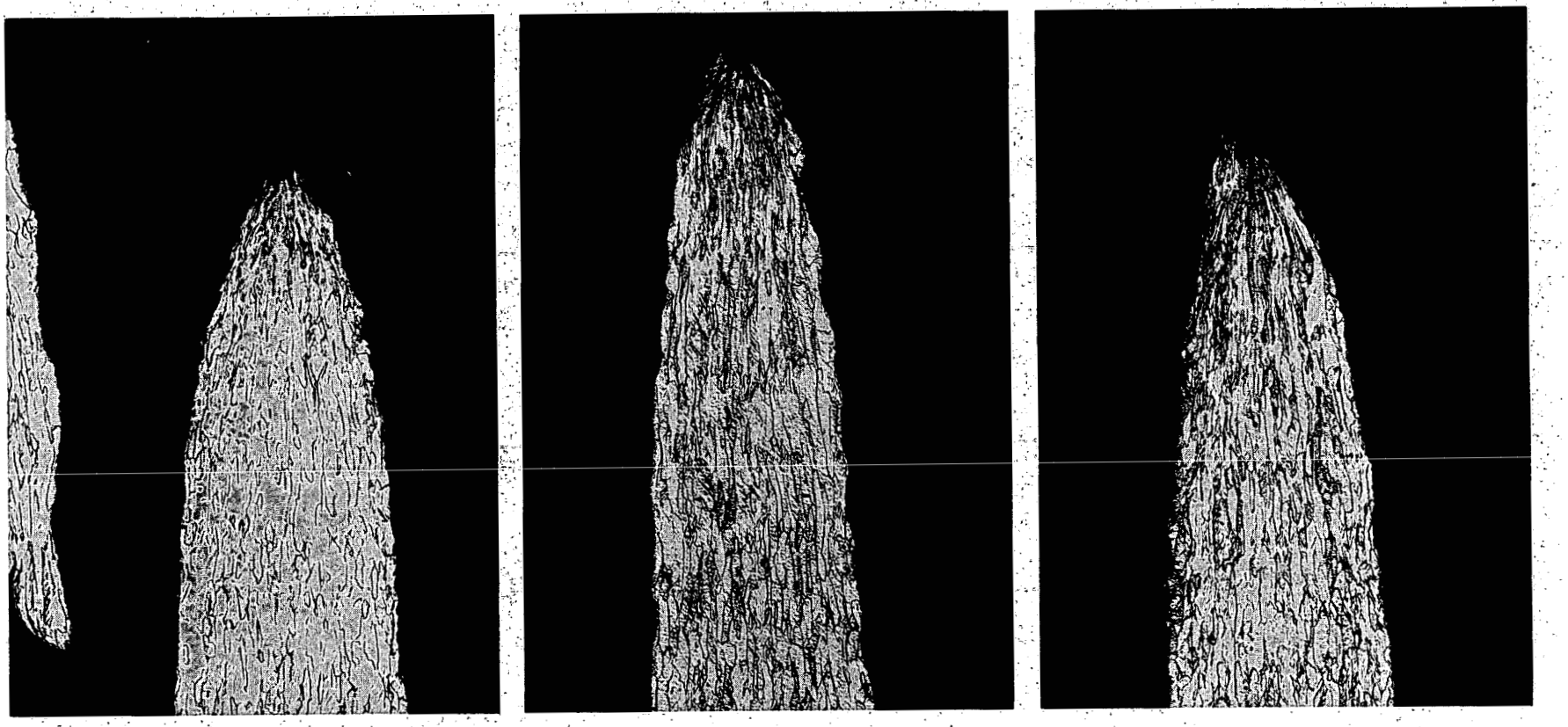

Unirradiated (Neg. R-2237)

As-irradiated – 1.1 x 10^{20} n/cm^2; $E_n \geq 1$ Mev (Neg. R-2239)

Irradiated (1.1 x 10^{20} n/cm^2) plus post-irradiation anneal at 1200°C for 1 hour (Neg. R-2241)

Fig. 2.47 – Photomicrographs of fracture area of high-carbon Mo sheet specimens creep-rupture tested at 700°C and 20.00 kg/mm^2 (100X)

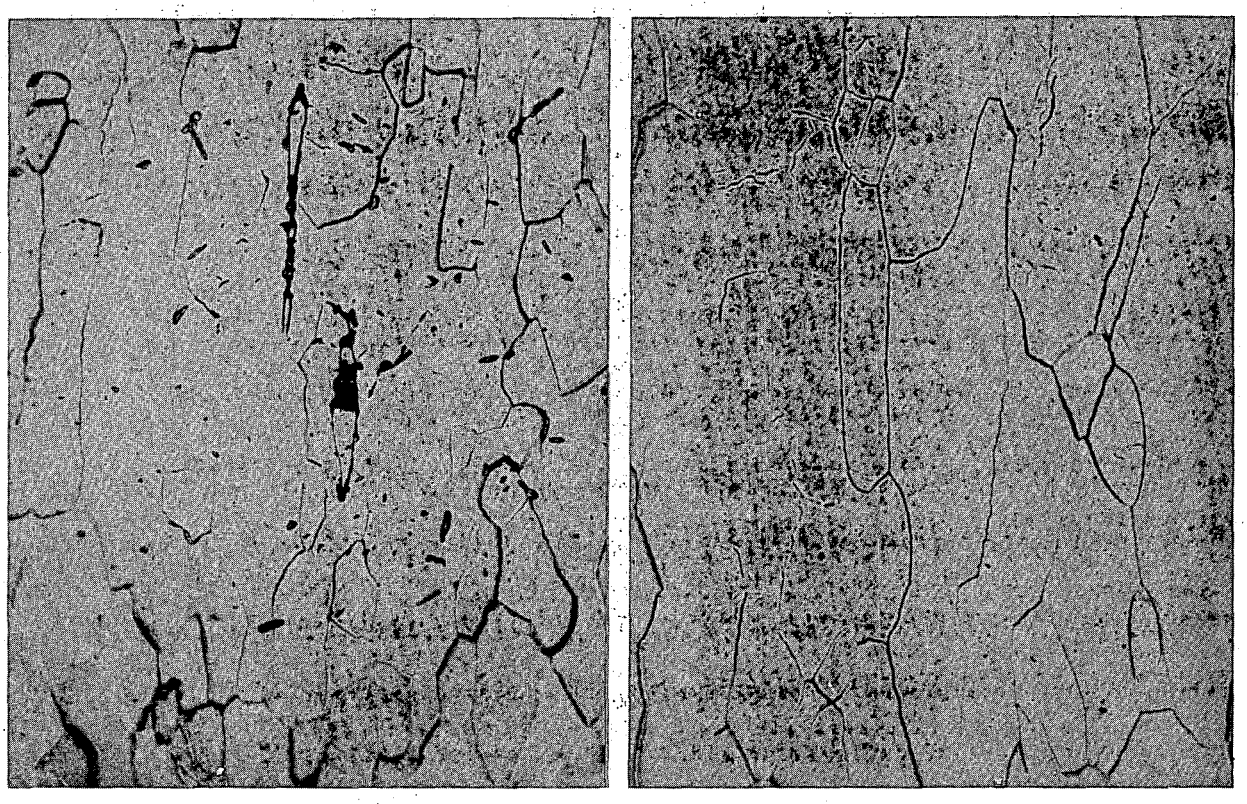

a. High-carbon Mo-heat C-6605 (Neg. R-2267)

b. Low-carbon Mo-heat C-7722 (Neg. R-2268)

Fig. 2.48 — Photomicrographs showing differences in carbide size and distribution in irradiated Mo sheet specimens post-irradiation annealed at 1200°C for 1 hour and creep-rupture tested at 700°C (500X)

Niobium and Nb – 1Zr

Hot-microhardness data were obtained on irradiated and unirradiated niobium and Nb – 1Zr. The Nb – 1Zr is harder over the entire temperature range due to solid-solution hardening and/or ZrC precipitation hardening. Some thermal hardening apparently started at a temperature of about 500°C and persisted at temperatures to 1000°C for the unirradiated material. These data are given in Figures 2.53 and 2.54, respectively, and the microhardness increment fraction curves obtained are shown in Figure 2.55. These curves show recovery at the same temperatures observed in ultimate tensile strength tests.

There are apparently peaks in the increment fraction curves for tungsten, molybdenum, and niobium at 0.16 T_m and approximately 0.35 T_m; the 0.16 T_m peak is the more prominent. Figure 2.56 gives a comparison on a homologous temperature basis of the increment fraction curves for W, Mo, and Nb[24], where it appears that the radiation-induced hardening of these unalloyed metals is recovered at temperatures above 0.35 T_m.[25]

Molybdenum Single Crystals

Hot-hardness data have been obtained on two single crystals of molybdenum of known orientations, {110} and {001}. There is a distinct difference in the data dependent on the crystallographic orientation (Figure 2.57). The specimen of orientation {110} showed little difference from polycrystalline molybdenum previously tested, although the specimen of orientation {001} was considereably softer at all temperatures. Photomicrographs (Figure 2.58) of the indents taken at 1200°C show markedly different flow patterns for the two orientations.

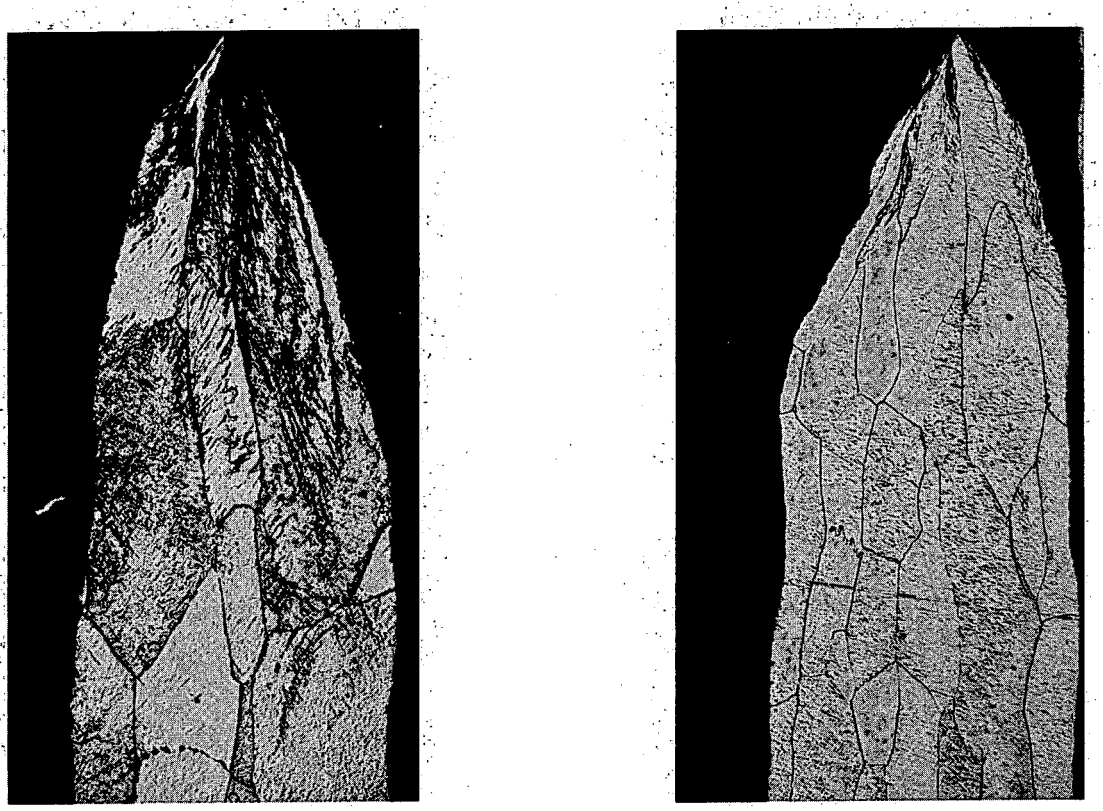

Unirradiated – 1600°C anneal for 1 hour in H_2 (R-2263)

Irradiated (1.2×10^{20} n/cm^2) plus 1600°C anneal for 1 hour (R-2255)

Fig. 2.49 – Photomicrographs of creep-rupture tested low-carbon Mo sheet specimens tested at 700°C and 13.0 kg/mm^2 (100X)

Other Refractory Alloys

Hot-microhardness data were determined[26] on five materials in the unirradiated recrystallized condition: Ta, Ta – 10W, W – 30Re – 30Mo (at.%; 306 alloy), W – 25Re – 30Mo (at.%; 256 alloy), and Mo – 0.5Ti. These investigations were conducted to study the effects of alloying and to provide comparison data for similar specimens being irradiated in the EBR-II.

A previous discussion[27] of the tantalum and Ta – 10W data noted an anomalous peak at approximately 300°C. Subsequent analyses show that the tantalum material contained 33 ppm oxygen prior to testing and 65 ppm after testing. Hence the peak may be due to interstitial impurities such as oxygen.[28]

HARDNESS AND ULTIMATE STRENGTH CORRELATION (J. L. Kamphouse, J. Moteff)

A relationship appears to exist[29-32] between hot hardness and other properties such as ultimate tensile strength and yield stress. Figures 2.59 through 2.61 show approximately linear relationships for several materials between the ultimate tensile strength, σ_u, in kg/mm^2 and the VPH number, H_v, in kg/mm^2. These linear relationships are not perfectly accurate, but they do give an estimate of the ultimate tensile strength of the material if the relatively convenient hot-hardness tests are performed first.

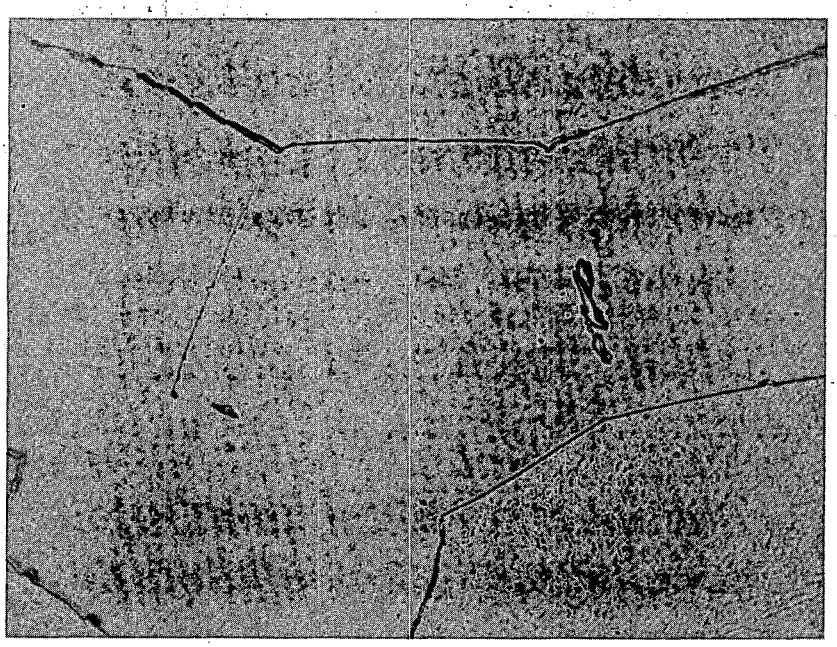

Fig. 2.50 — Photomicrograph of unirradiated low-carbon Mo sheet specimen (1600°C — 1 hour anneal) showing agglomerated carbides. Specimen creep-rupture tested at 700°C and 13.00 kg/mm^2. (Neg. R-2269, 500X)

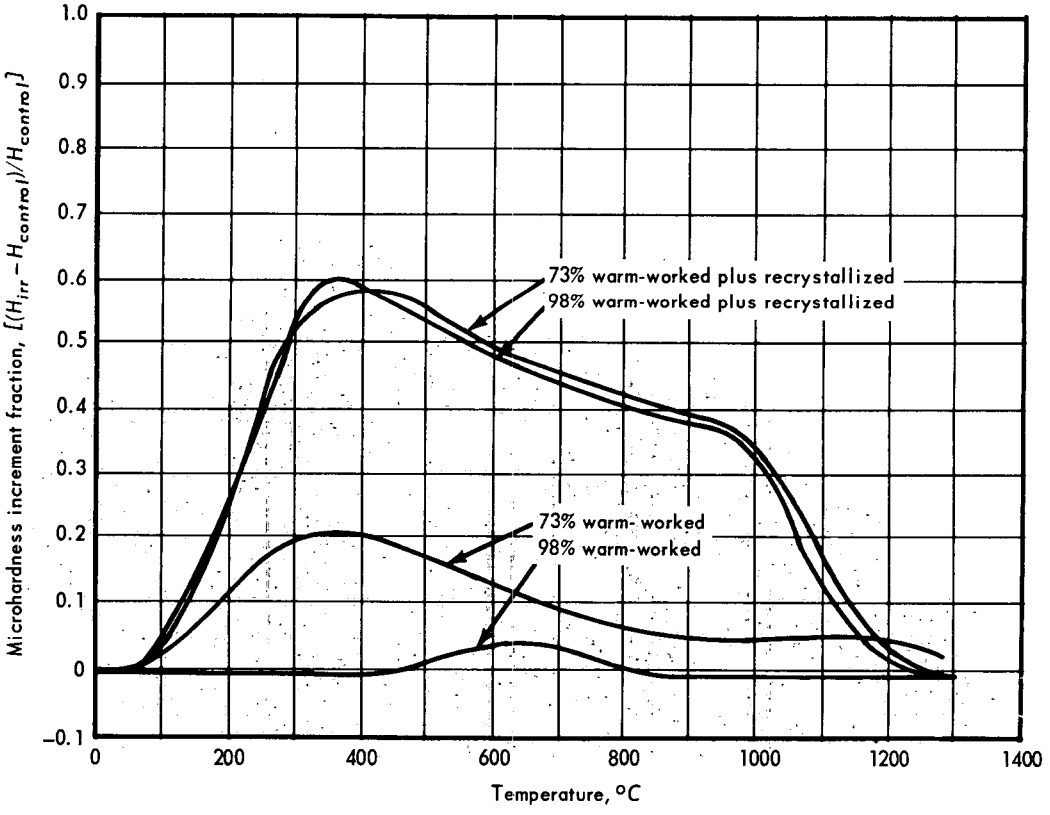

Fig. 2.51 — Hot-microhardness increment fraction for irradiated W in various conditions as a function of temperature. Specimens irradiated at ambient temperature (~70°C) in a water-moderated reactor to a fluence of 4.1 x 10^{19} n/cm^2 ($E_n \geq 1$ Mev). Recrystallized material annealed at 1760°C for 1 hour in H_2 prior to irradiation.

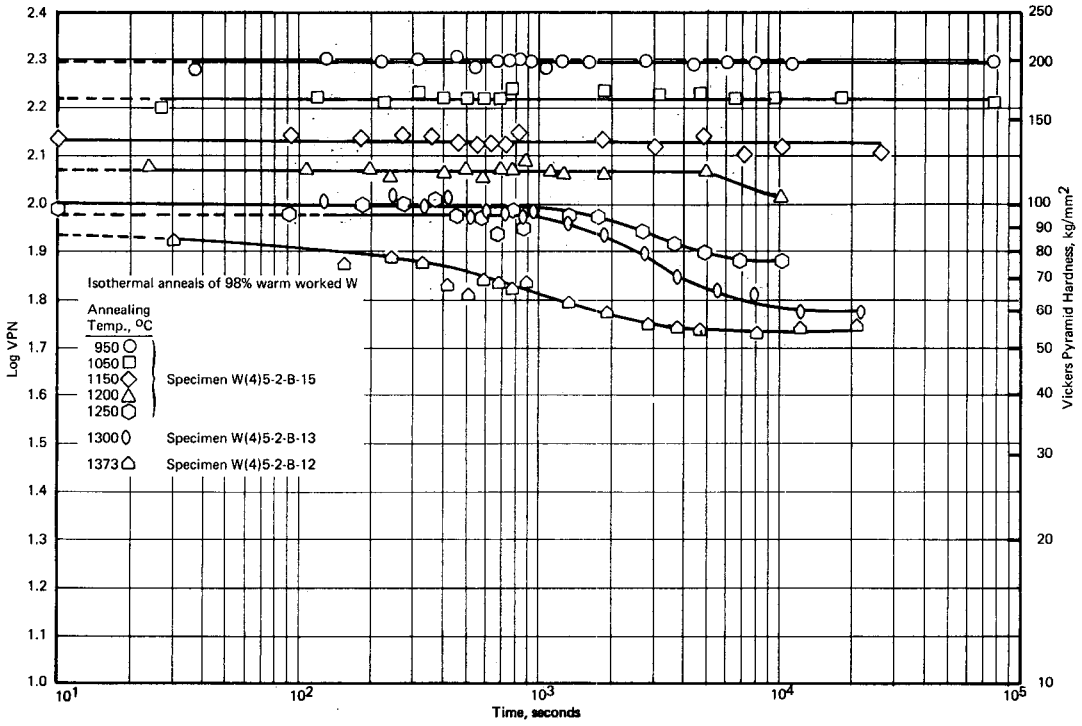

Fig. 2.52 – Isothermal hot-microhardness recovery of unirradiated 98% warm worked W as a function of annealing time.

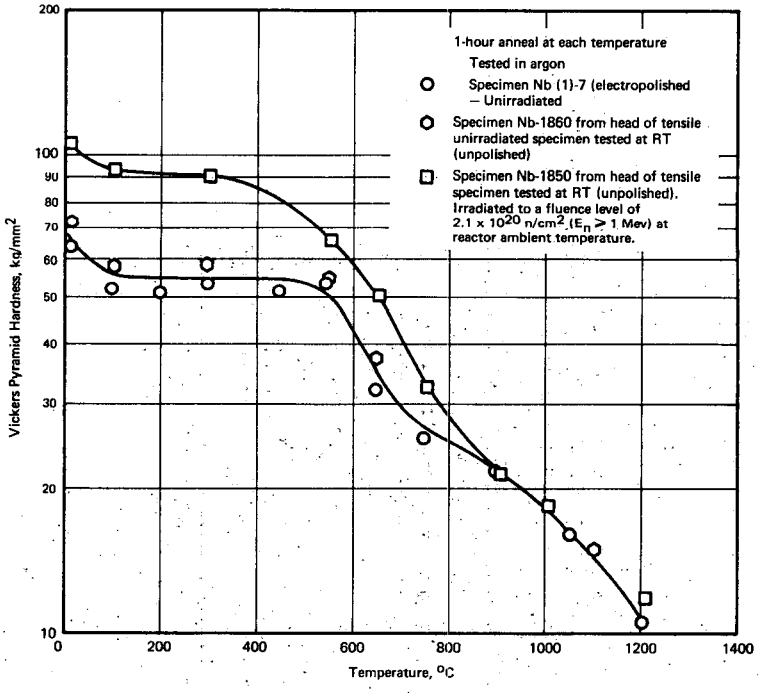

Fig. 2.53 – Hot microhardness of unirradiated and irradiated Nb as a function of temperature

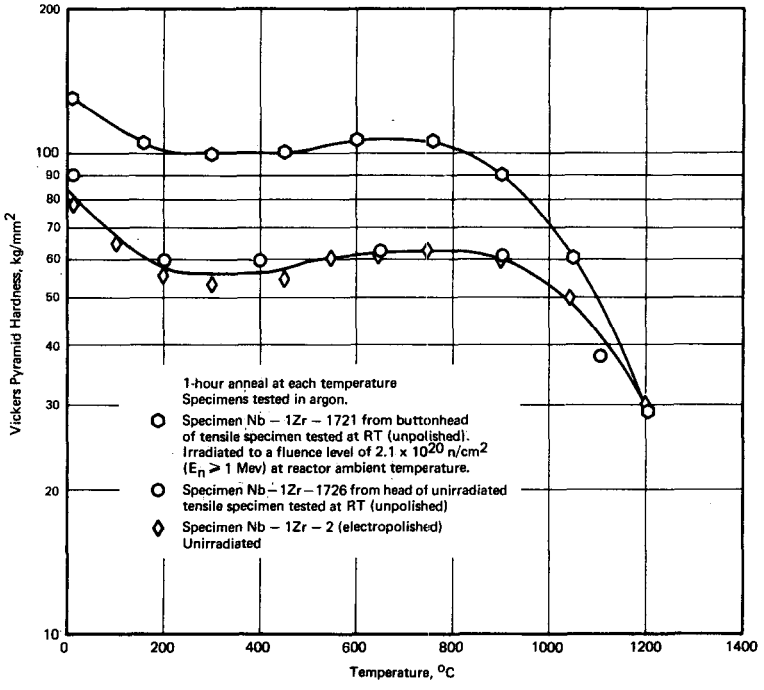

Fig. 2.54 – Hot microhardness of unirradiated and irradiated Nb – 1Zr as a function of temperature

TENSILE TESTING (W. J. Stapp, A. R. Begany)

Niobium and Nb – 1Zr

A study of the effect of annealing on the room-temperature and elevated-temperature tensile properties of irradiated (2.1×10^{20} n/cm^2, $E_n \geq 1$ Mev at ~ 70°C) recrystallized niobium and Nb-1Zr was conducted. Irradiated and control sheet specimens were post-irradiation annealed at temperatures determined by hot-hardness studies. The temperatures were selected to show most advantageously the room-temperature and elevated-temperature radiation-damage recovery behavior.

The effect of post-irradiation anneals on the room-temperature engineering tensile properties of niobium appears in Figure 2.62 and Table 2.6. Recovery was complete following the 1000°C anneal. In the hot-hardness studies recovery was complete (Figure 2.53) following the 900°C anneal. Comparison of the data shows that neutron irradiation increased ultimate strength less than yield strength. Irradiation drastically reduced the uniform elongation. The tensile behavior observed in the post-irradiation anneals is similar to that observed in irradiated molybdenum,[33,34] tungsten,[35] and niobium[36] in other studies, except that no evidence of lower yield points was observed.

The elevated-temperature (300°C and 650°C) tests were conducted after holding at test temperature for 1 hour, giving specimens, in effect, a 1-hour anneal at test temperature. The results (Figure 2.63 and Table 2.6) do not show any indication of thermal hardening, as might be suggested by an increase in the ratio of irradiated to unirradiated yield strength values at the elevated test temperatures. The dotted lines on the ultimate strength plots represent values determined from linear cross plots of hot hardness (DPH) versus ultimate tensile strength. Pronounced thermal hardening had been observed by Makin and Minter[36] in room-temperature tensile tests following 200° to 300°C anneals for 1 hour.

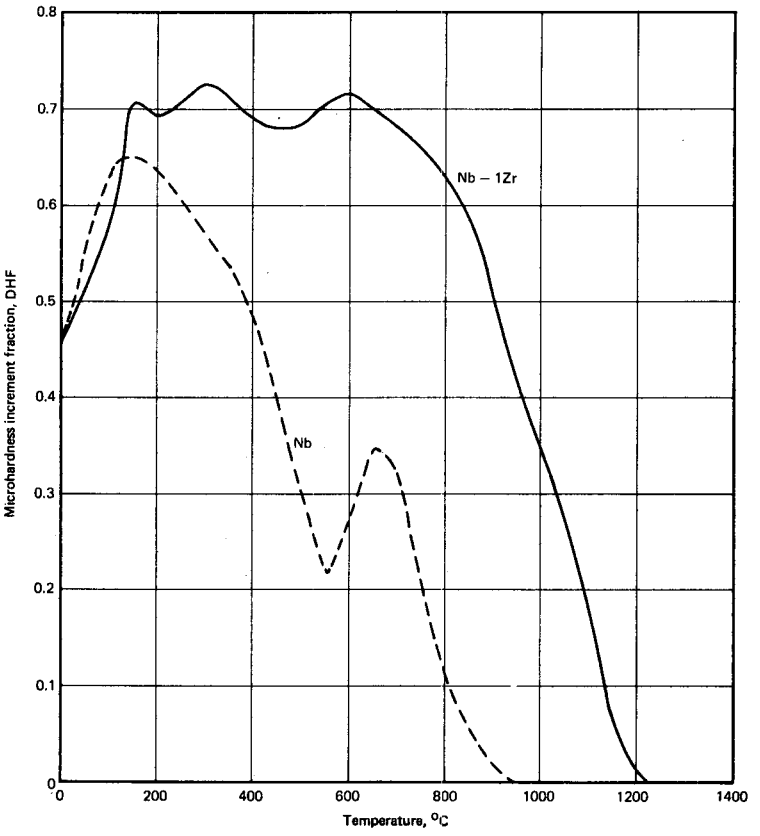

Fig. 2.55 – Hot-microhardness increment fraction for irradiated (2.1×10^{20} n/cm^2; $E_n \geqslant 1$ Mev) Nb as a function of temperature

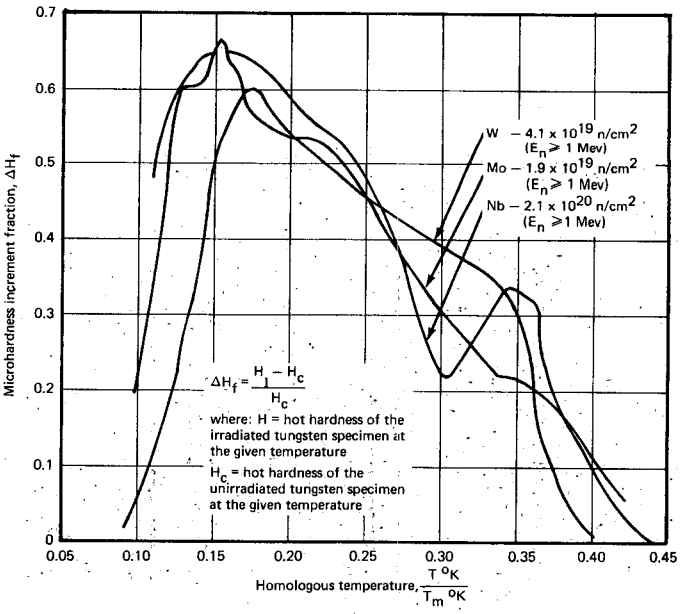

Fig. 2.56 – Microhardness increment fraction, ΔH_f, for W, Mo, and Nb compared on a homologous temperature basis

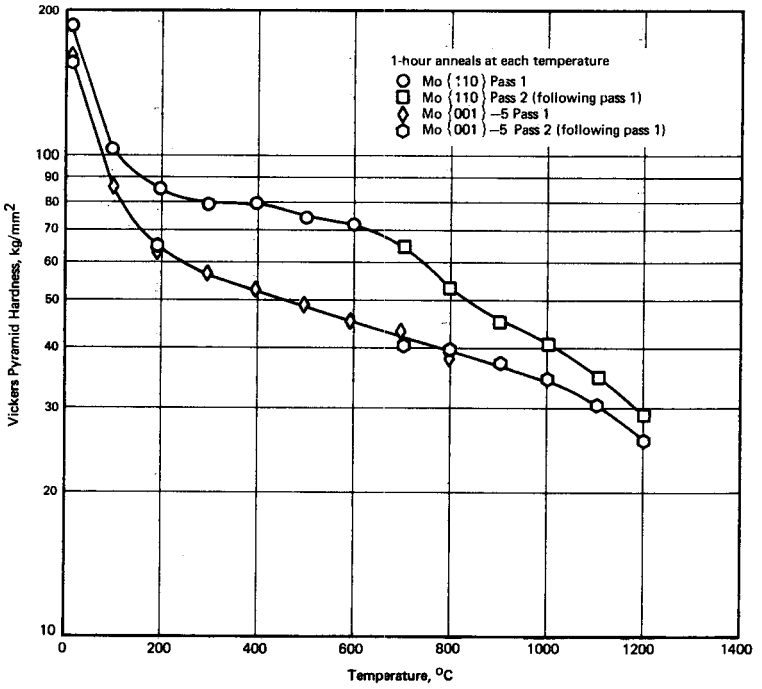

Fig. 2.57 – Hot microhardness of unirradiated single-crystal molybdenum of orientations {110} and {001}

The present results do not agree with the 600 °C temperature shown to produce complete recovery in the earlier work.[36] The NMPQ material contained 130 ppm oxygen compared to 1600 ppm oxygen in the earlier tests. This difference and a higher neutron fluence level probably account for the higher recovery temperature. The higher strength and lower ductility levels in the specimens containing the higher oxygen level may have masked out the influence of radiation-induced defects on the mechanical properties.

The effect of post-irradiation anneals on the conventional room-temperature tensile properties of Nb – 1Zr shown in Figure 2.64 and Table 2.7 exhibit a type of thermal hardening in the 300° to 600 °C range which agrees with hot-hardness results. Complete recovery of the radiation-induced defect structure occurs after the 1000 °C anneal. Complete recovery did not occur until 1200 °C in the hot-hardness studies.

Nb – 1Zr exhibited greater strength in the irradiated condition up to a test temperature of 600 °C (Figure 2.65). Reduced ductilities were observed in both irradiated and unirradiated specimens at the 300 °C and 600 °C test temperatures.

Molybdenum

A study of the effect of post-irradiation annealing on the room-temperature tensile properties of irradiated, recrystallized molybdenum was conducted and reported.[37] Data were examined[38] in terms of the true stress versus true strain relationship to evaluate strain-hardening characteristics. The analysis employed the empirical power law expression:

$$\sigma = k\,(\bar{\epsilon})^{n} \qquad (2.1)$$

where:

σ = true stress
$\bar{\epsilon}$ = true strain (or natural strain)
k = constant (strength coefficient at $\bar{\epsilon} = 1$)
n = constant (strain-hardening exponent)

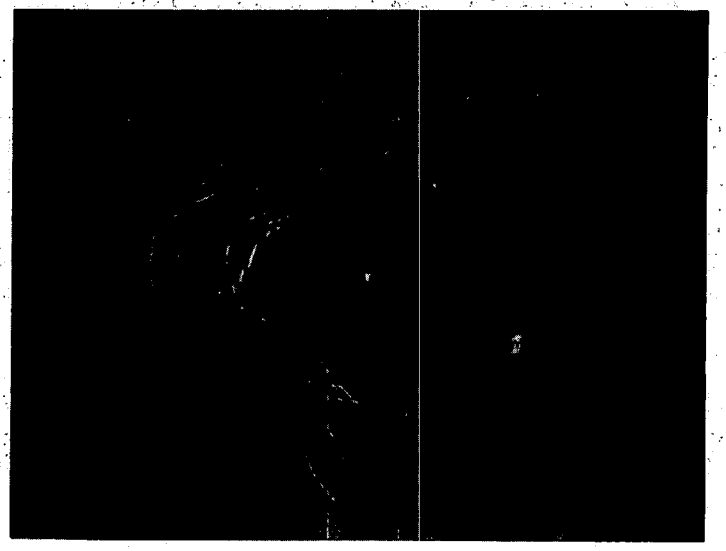

{100} orientation

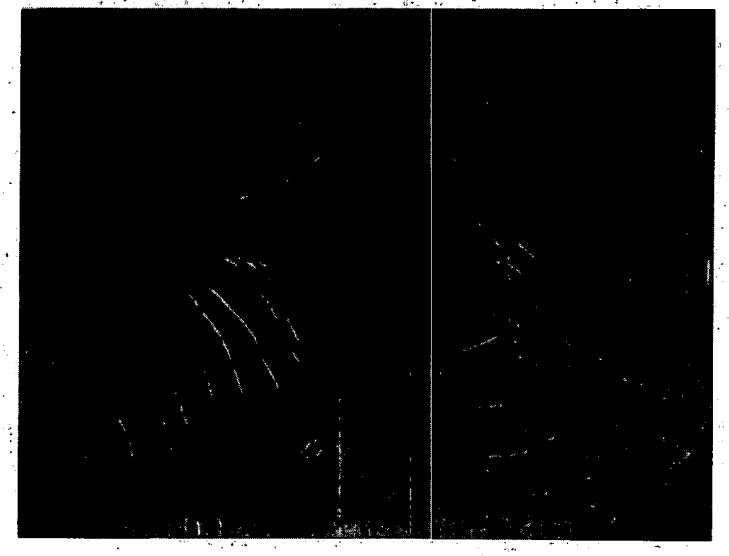

{110} orientation

Fig. 2.58 — Photomicrographs of hot-microhardness (1200°C) indents on Mo single-crystals of two orientations (200X)

It was concluded that the increase in strength of the irradiated molybdenum was due to both source and lattice defect mechanisms.

The data were re-examined in terms of the exponential function[42] relating true stress (σ) and true strain ($\bar{\epsilon}$):

$$\sigma = \sigma_\infty - (\sigma_\infty - \sigma_o) \exp(-\bar{\epsilon}/\epsilon_c)$$

where:

σ_o = stress at which plastic deformation begins
σ_∞ = asymptotic stress attained after deformation
ϵ_c = characteristic strain

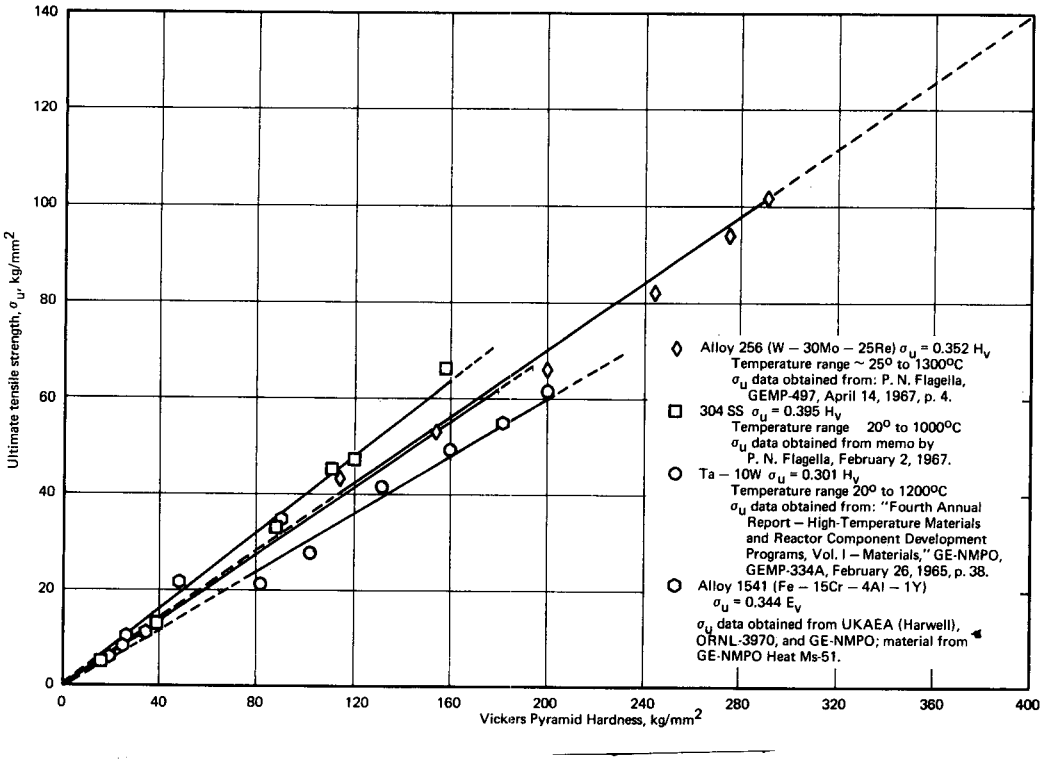

Fig. 2.59 – Ultimate tensile strength, σ_u, as a function of Vickers Pyramid Hardness, H_v, for various alloys

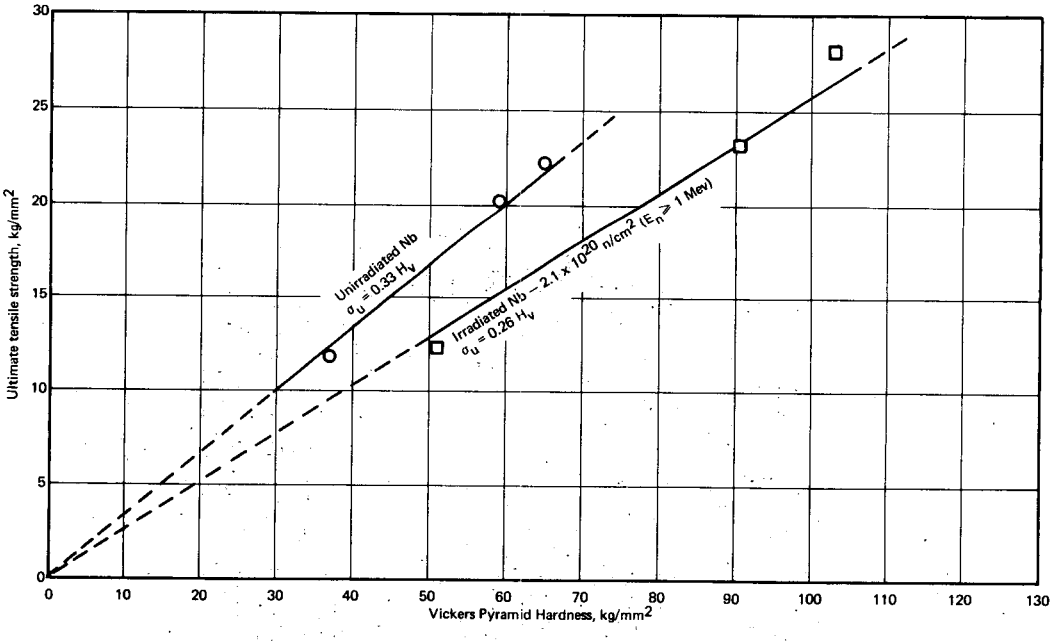

Fig. 2.60 – Ultimate tensile strength, σ_u, as a function of Vickers Pyramid Hardness, H_v, for Nb

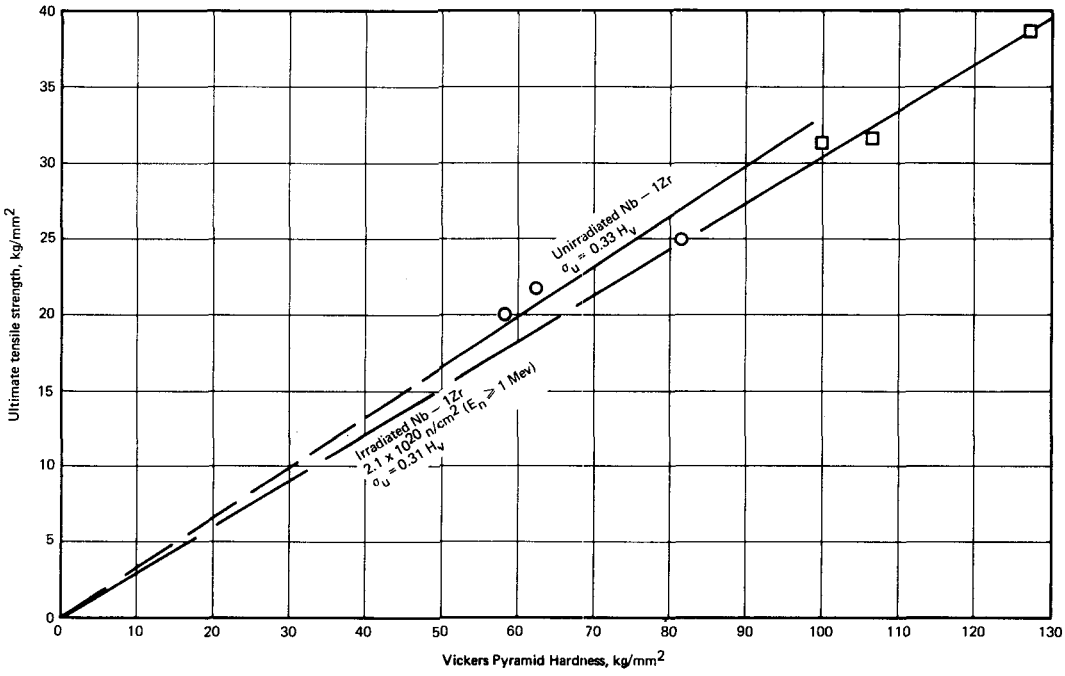

Fig. 2.61 — Ultimate tensile strength, σ_u, as a function of Vickers Pyramid Hardness, H_v, for Nb — 1Zr

Results (Table 2.8 and Figure 2.66) of the exponential function show that:

1. σ_o is increased by radiation-induced defects to a point of elastic fracture and decreased by post-irradiation annealing to the σ_o value of the nonirradiated material. σ_o may be considered the lattice friction stress at zero strain or slip propagation stress.
2. Molybdenum will elongate and work-harden by the generation of dislocations. Size and/or number of radiation-induced defects are varied by annealing heat treatments, thereby affecting the characteristic strain, ϵ_c.
3. The asymptotic stress is not significantly sensitive to the number or size of the radiation-induced defects.

Hence it is again concluded that the radiation-induced increase in strength of recrystallized molybdenum is due to both the source-hardening and lattice-hardening defect mechanisms.

Fracture areas of selected room-temperature, tensile-tested molybdenum specimens were examined to determine possible differences in microstructural flow and fracture characteristics between the unirradiated, irradiated, and post-irradiation annealed conditions. Since mixed modes of fracture were expected in some cases, it was believed that optical fractography would complement the metallographic examinations and provide detailed insight into the differences in modes of fracture between the various conditions. Specifically, examination of the actual fracture faces for evidence of dimple rupture features characteristic of the ductile mode of fracture was deemed expedient. The fractographic studies were conducted at 500 diameters using dark-field illumination. Specimens in this study possessed irregular surfaces with varying amounts of localized necking on gage sections whose original dimensions were 0.5 by 6.3 mm. In general, irradiated specimens receiving a post-irradiation anneal lower than about 950°C displayed considerable embrittlement with little or no localized necking (Figure 2.67).

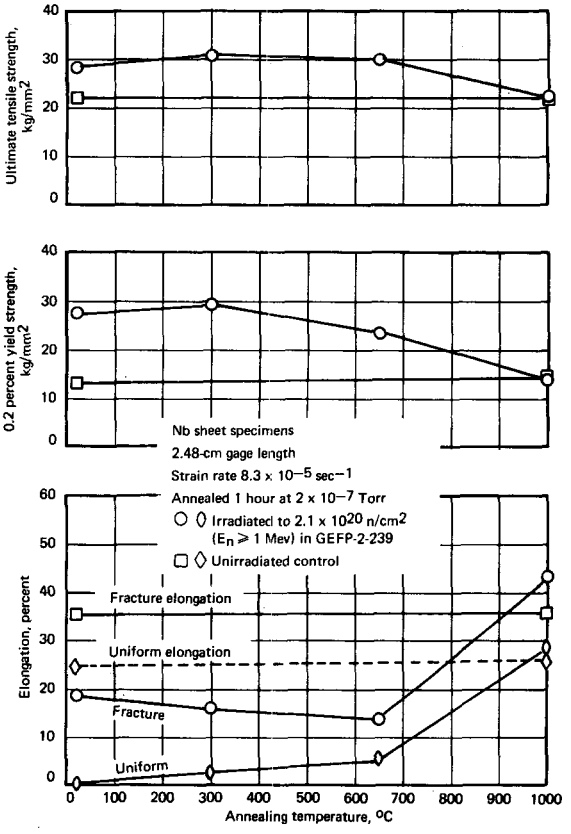

Fig. 2.62 — Room-temperature tensile properties of Nb sheet specimens versus post-irradiation annealing temperature

TABLE 2.6

NIOBIUM TENSILE TEST RESULTS

Specimen[a] No.	Condition	Post Irradiation Anneal Temperature, °C	Test Temperature, °C	Yield Strength 0.2% Offset, kg/mm^2	Tensile Strength, kg/mm^2	Uniform Elongation in 2.48 cm, %	Fracture Elongation in 2.48 cm, %
1860	Unirradiated	None	25	13.2	22.2	24.4	35.5
1862	Unirradiated	300—1 hr—vac[b]	300	13.2	20.2	9.2	13.4
1861	Unirradiated	650—1 hr—vac[b]	650	6.9	11.8	9.0	14.7
1850	Irradiated[c]	None	25	27.6	28.2	0.5	18.6
1848	Irradiated	300—1 hr—vac[b]	300	23.2	23.2	0.4	5.9
1849	Irradiated	650—1 hr—vac[b]	650	12.3	12.3	1.0	12.6
1859	Irradiated	300—1 hr—vac[e]	25	29.5	31.1	2.5	15.9
1852	Irradiated	650—1 hr—vac[e]	25	23.3	29.0	5.4	13.5
1854	Irradiated	1000—1 hr—vac[e]	25	13.8	23.4	28.3	43.0
1855	Unirradiated	1000—1 hr—vac	25	14.1	21.6	25.3	35.3

[a]Specimens from 0.5-mm-thick sheet No. 80B792, vacuum annealed at 1150°C for 1 hour after fabrication. All tests conducted in vacuum ~8 x 10^{-5} Torr.

[b]Heating rate to test temperature 20°C/min, annealed for 1 hour prior to load application. Power turned off upon specimen fracture.

[c]Irradiation test GEFP2-239 in ETR facility at reactor-ambient temperature (~70°C) to a fluence of 2.1 x 10^{20} n/cm^2 ($E_n \geq 1$ Mev) and 4.7 x 10^{20} n/cm^2 (thermal).

[d]Elastic fracture.

[e]Annealed for 1 hour in a vacuum of 2 x 10^{-7} Torr.

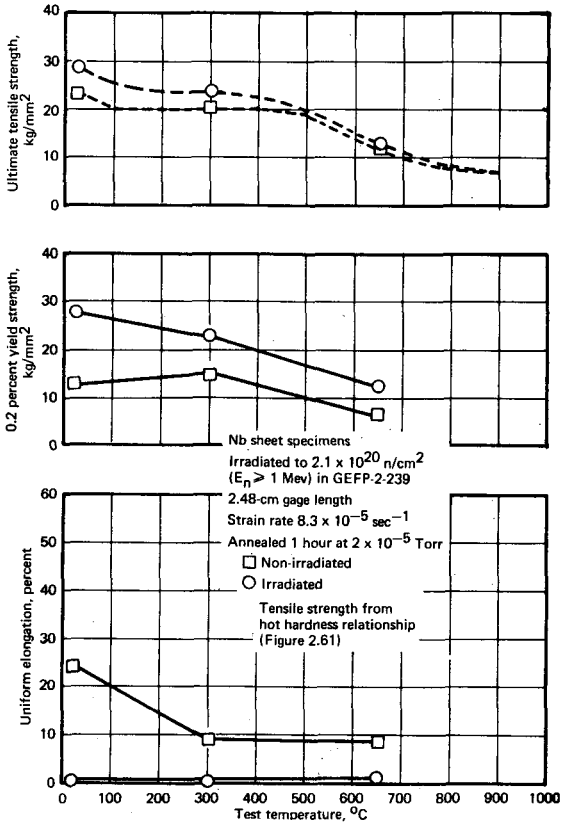

Fig. 2.63 — Elevated-temperature tensile properties of unirradiated and irradiated niobium sheet specimens

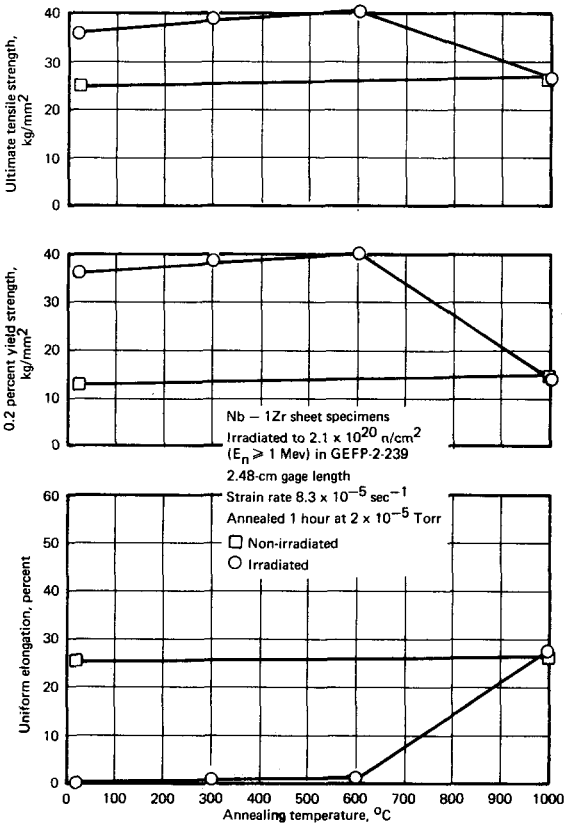

Fig. 2.64 — Room-temperature tensile properties of unirradiated and irradiated Nb – 1Zr sheet specimens

TABLE 2.7

Nb – 1Zr TENSILE TEST RESULTS

Specimen No.[a]	Condition	Post Irradiation Anneal Temperature, °C	Test Temperature, °C	Yield Strength 0.2% Offset, kg/mm²	Tensile Strength, kg/mm²	Uniform Elongation in 2.48 cm, %	Fracture Elongation in 2.48 cm, %
1726	Unirradiated	None	25	12.7	24.9	25.1	33.5
1729	Unirradiated	300–1 hr–vac[b]	300	8.3	20.0	10.9	15.5
1730	Unirradiated	600–1 hr–vac[b]	600	13.2	21.8	14.1	21.0
1721	Irradiated	None	25	38.7	38.7	0.2	0.4
1723	Irradiated	300–1 hr–vac[b]	300	27.4	31.3	1.6	1.6
1727	Irradiated	600–1 hr–vac[b]	600	27.8	31.5	1.5	2.6
1725	Irradiated	300–1 hr–vac[e]	25	38.7	38.6	0.7	4.9
1722	Irradiated	600–1 hr–vac[e]	25	40.0	40.5	0.9	8.0
1719	Irradiated	1000–1 hr–vac[e]	25	14.0	26.4	22.4	33.4
1724	Unirradiated	1000–1 hr–vac[e]	25	13.9	26.6	26.2	34.6

[a]Specimens from 0.5-mm-thick sheet (heat No. 27605), vacuum annealed at 1200°C for 1 hour after fabrication. All tests conducted in vacuum ~8 x 10^{-5} Torr.

[b]Heating rate to test temperature 20°C/min, annealed for 1 hour prior to load application. Power turned off upon specimen fracture.

[c]Irradiation test GEFP2-239 in ETR facility at reactor-ambient temperature (~70°C) to a fluence of 2.1 x 10^{20} n/cm² ($E_n \geq 1$ Mev) and 4.7 x 10^{20} n/cm² (thermal).

[d]Elastic fracture.

[e]Annealed for 1 hour in a vacuum of 2 x 10^{-7} Torr.

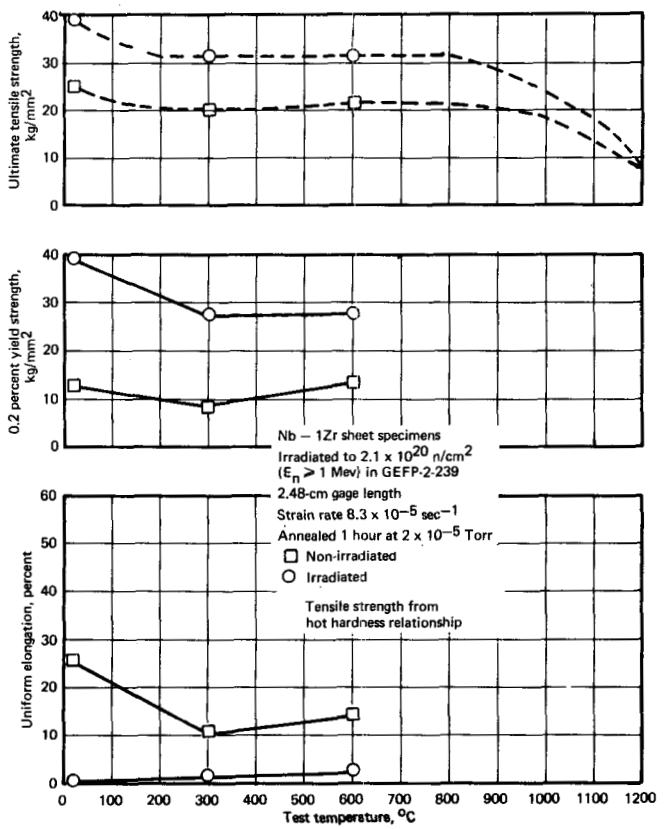

Fig. 2.65 – Elevated-temperature tensile properties of unirradiated and irradiated Nb – 1Zr sheet specimens

Metallographic examination of the unirradiated specimens showed failure to be entirely transgranular (Figure 2.68) without any trace of intergranular fracture. A moderate amount of plastic flow (necking) in the fracture area had occured. Fractographic study of these fractures indicated a condition of quasi-cleavage; i.e., the fracture displayed characteristics of feathery cleavage (little or no plastic deformation) while possessing some plastic deformation features such as tear ridges and stretching.

The as-irradiated specimen exhibited mixed mode of fracture with intergranularity slightly in preponderence. No evidence of any appreciable wedging or ductility was observed.

The fractographic study of the post-irradiated annealed specimens showed that fracture occurred predominately by cleavage. Specimens annealed at 1025 °C and higher tended to exhibit quasi-cleavage. No post-irradiated specimens exhibited evidence of ductile dimple rupture. Specimens annealed at 950 °C and lower displayed mixed modes of fracture. In general, lowering the annealing temperature resulted in increased evidence of intergranular fracturing.

Although these observations were substantiated during metallographic examination, a possible exception to this was the following microstructural anomaly: the secondary cracking condition possessed by the 830 °C post-irradiation annealed specimen was predominantly intergranular, whereas the secondary cracking within the 700 °C annealed specimen was predominantly transgranular (see Figure 2.69).

TABLE 2.8

MOLYBDENUM TENSILE TEST RESULTS

Specimen No.[a]	Condition	Post Irradiation Anneal Temperature,[b] °C	Test Temperature, °C	Yield Strength 0.2% Offset, kg/mm^2	Tensile Strength, kg/mm^2	Uniform Elongation in 2.54 cm, %	Fracture Elongation in 2.54 cm, %	True Stress at Zero Strain (σ_o), kg/mm^2	True Asymptotic Stress (σ_∞), kg/mm^2	Characteristic Strain (ϵ_c), cm/cm
2100	Unirradiated	None	25	37.6	50.2	18.4	40.0	31.66	67.03	0.110
2110	Irradiated[c]	830	25	68.6	71.3	0.8	1.2	69.2	72.20	0.001
2112	Irradiated[c]	950	25	44.4	63.1	8.7	9.6	52.15	71.63	0.050
2108	Irradiated[c]	1025	25	47.6	56.6	13.6	32.7	44.51	70.65	0.092
2106	Irradiated[c]	1100	25	34.4	52.8	16.9	49.9	36.00	67.11	0.108
2121	Irradiated[c]	1200	25	31.7	48.9	16.3	41.8	31.18	62.77	0.090

[a]Specimens from 0.5-mm-thick arc-cast Mo sheet (heat C-6605), post-grind annealed at 1200°C in vacuum for 1 hour.
[b]One-hour anneals in gettered argon up to 950°C, 1-hour anneals in purified hydrogen above 950°C, at temperature indicated.
[c]ORM-38; irradiated to 1.2×10^{20} nvt ($E_n \geq 1$ Mev) at reactor-ambient temperature.

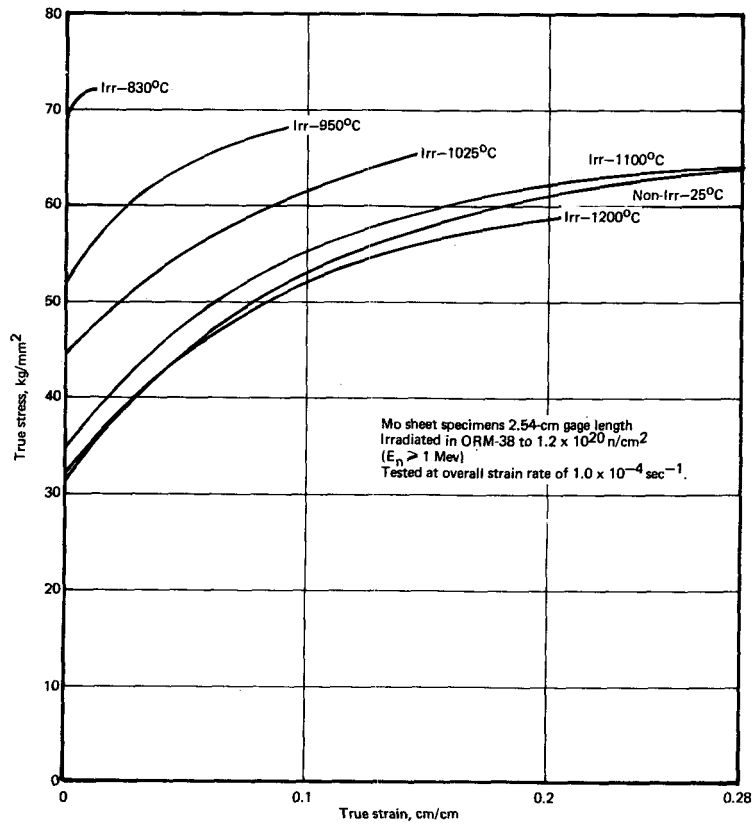

Fig. 2.66 — Room-temperature stress versus strain curves for irradiated (ORM-38) molybdenum post-irradiation annealed at indicated temperature

RESISTIVITY STUDIES (L. K. Keys, J. Moteff)

Molybdenum

The isochronal resistivity recovery of fast neutron ($E \geq 1$ Mev) radiation-induced defects in recrystallized molybdenum specimens has continued.[39] Six specimens were irradiated at reactor-ambient temperature (~70 °C) to fast neutron fluences ranging from 1.1×10^{19} to 1.5×10^{21} n/cm^2 ($E_n \geq 1$ Mev). The various samples used and the pertinent irradiation conditions are shown in Table 2.9. The dependence of the radiation-induced resistivity increment, $\Delta\rho$, on the fast neutron fluence (for NMPO studies as well as those of Peacock and Johnson[40]) is presented in Figure 2.70. The resistivity increment, $\Delta\rho$, is defined as $\Delta\rho = \rho_I - \rho_O$, where ρ_I is the as-irradiated resistivity and ρ_O is the pre-irradiation resistivity. The resistivity increment reaches a maximum between 5×10^{19} n/cm^2 and 2×10^{20} n/cm^2, then decreases by about a factor of 2 at 1.5×10^{21} n/cm^2. This result is somewhat surprising in view of the asymptotic approach to saturation considered in other investigations.[23,41] The slope of the linear portion of the curve (a slope of about 0.58) is in good agreement with that reported by Peacock and Johnson (0.54), although they observed what appeared to be saturation effects at about 3 to 4×10^{18} n/cm^2. Results of NMPO studies and those of Kissinger, Brimhall, and Mastel[42] yield saturation fluences much higher than those of Peacock and Johnson. Kissinger et al. observed saturation below NMPO saturation fluences. These differences result from different techniques of observation (X-ray parameter and length changes), as will be shown.

The recovery of the irradiation-induced defects in molybdenum is presented in Figure 2.71, in which the radiation-induced resistivity, $\Delta\rho$, is plotted versus annealing tempera-

Fig. 2.67 – Photomicrograph of fracture area of room-temperature tensile-tested Mo sheet specimen after irradiating to 1.1×10^{20} n/cm^2 ($E_n \geqslant 1$ Mev). Specimen given an 830°C anneal for 1 hour prior to testing. (Neg. R-2227, 100X)

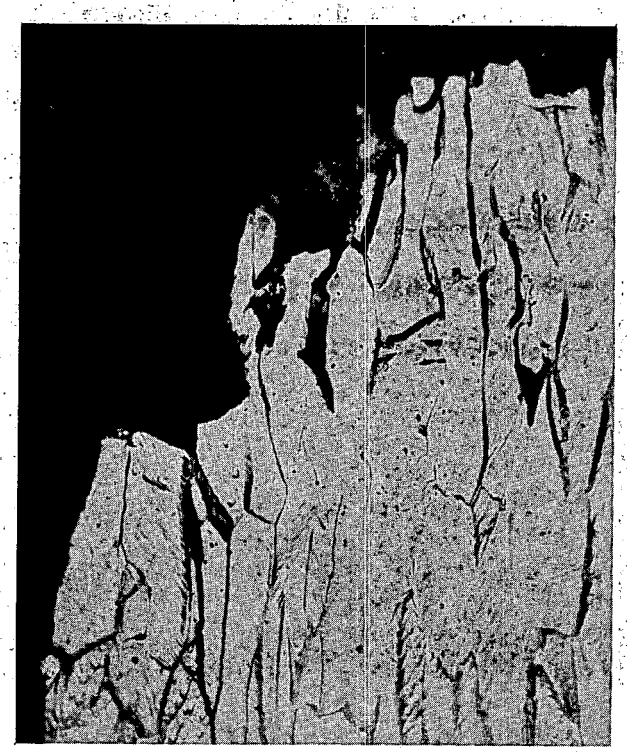

Fig. 2.68 – Photomicrograph of fracture area of unirradiated room-temperature tensile-tested Mo sheet specimen (Neg. R-2236, 500X)

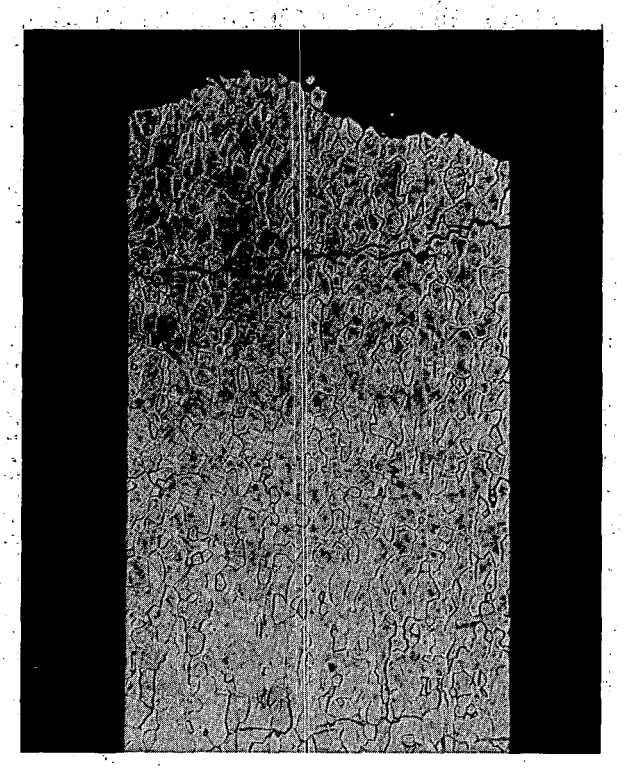

Fig. 2.69 – Photomicrograph of fracture area of room-temperature tensile-tested Mo specimen showing predominantly transgranular secondary cracking. Irradiated (1.1×10^{20} n/cm^2, $E_n \geq 1$ Mev) specimen given a 700°C anneal for 1 hour prior to testing. (Neg. R-2257, 100X)

TABLE 2.9

PRINCIPLE DEFECT RECOVERY STAGES IN NEUTRON-IRRADIATED MOLYBDENUM AS DETERMINED BY ISOCHRONAL RESISTIVITY STUDIES

Sample No.	Rod	Capsule	Irradiation Condition[a] Fluence, nvt Fast ($E_n > 1$ Mev)	Thermal	Peak Temperature of Recovery Spectra, and Area Under Respective Recovery Peak[b] 0.15 T_m, °C	($\Delta\rho_{III}$) Area, micro-ohm-cm	0.31 T_m, °C	($\Delta\rho_{IV}$) Area, micro-ohm-cm	($\Delta\rho_{III}/\Delta\rho_{IV}$) Area, micro-ohm-cm
520	C	ORM-14	1.1×10^{19}	9.3×10^{19}	153	0.396	624	0.163	2.43
527	C	ORM-18	2.3×10^{19}	1.1×10^{20}	163	0.476	620	0.227	2.10
2277	M	ORM-54	5.8×10^{19}	4.1×10^{20}	150	0.693	616	0.406	1.71
909	L	MT-138	9.8×10^{19}	3.7×10^{20}	160	0.608	619	0.536	1.13
923	L	ORM-38	1.1×10^{20}	5.2×10^{20}	157	0.701	620	0.567	1.24
914	L	MT 2-234	1.5×10^{21}	2.6×10^{21}	–	0	606	0.596	0

[a]Specimens irradiated at reactor-ambient temperatures in a water-moderated reactor (ORR or ETR).

[b]Peak temperature of recovery refers to temperature of maxima in the derivative of the recovery curves. This recovery maximun is related to the melting temperature, T_m, as shown.

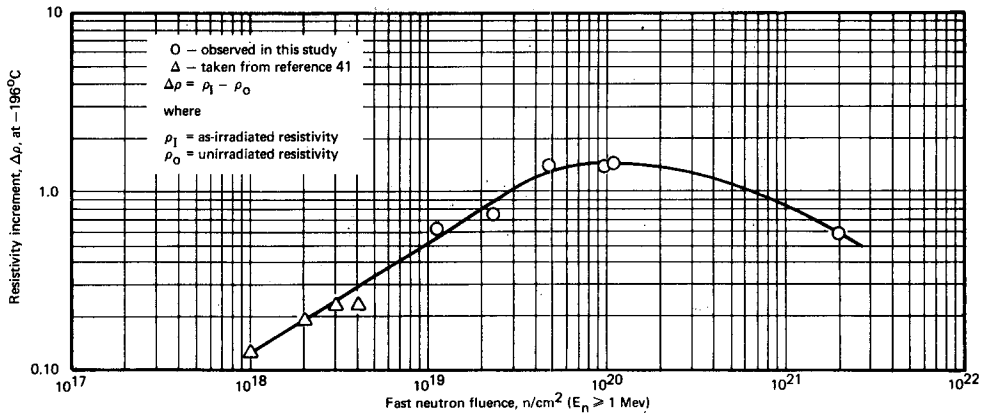

Fig. 2.70 – Total radiation-induced resistivity increment for Mo as a function of fast neutron fluence

ture. The recovery of radiation-induced defects after reactor-ambient (~70°C) irradiations resembles that for tungsten.[43, 44] Two principal recovery regions are evident in all but the highest fluence specimen. These recovery regions are more distinct in Figure 2.72, in which the derivative $d(\Delta\rho/\Delta\rho_o)/dT$ of the normalized resistivity increment is plotted versus annealing temperature. The two principle recovery regions centered at about 160°C and 620°C, respectively, occur at almost exactly 0.15 T_m (stage III) and 0.31 T_m (stage IV) and agree quite well with the recovery observed by Ibragimov et al.[45] after a 2 x 10^{20} n/cm^2 irradiation with fast neutrons. As for tungsten,[43] the lower temperature recovery region (0.15 T_m) is believed to represent the migration and recovery of self-interstitials, and the higher-temperature recovery region (0.31 T_m) represents the recovery of vacancies. (The term interstitial will be considered, for the remainder of this discussion, to mean self-interstitial unless specified otherwise.) Other smaller recovery regions are evident in some of the specimens, similar to tungsten.[46] The reproducibility of these smaller peaks is uncertain in NMPO studies and in the studies of others;[40,45,47] their importance should not be overlooked, however, since the defects responsible for these peaks apparently contribute to the thermal hardening in this recovery region.[48] In Figure 2.73 the resistivity recovered in stage III ($\Delta\rho_{III}$) and stage IV ($\Delta\rho_{IV}$) is presented. The stage III resistivity recovery completely saturates over this range, dropping to zero at the highest fluence. The stage IV recovery, however, shows a linear fluence dependence up to about 10^{20} n/cm^2, where a normal asymptotic approach to saturation is evident. These results are in relatively good agreement with those of Kissinger, Brimhall, and Mastel[42] who have investigated, by lattice parameter and length change studies, the fast-neutron, radiation-induced fluence dependence in molybdenum over a range of 10^{19} to 10^{20} n/cm^2. The results of the length change study indicate that vacancies saturate at about 10^{20} n/cm^2 or above, and that interstitials saturate at approximately 2 to 5 x 10^{19} n/cm^2. The ratio of the stage III resistivity ($\Delta\rho_{III}$) recovery to the stage IV recovery ($\Delta\rho_{IV}$), presented in Figure 2.74, shows a linear dependence on the fast neutron fluence, on a semilog plot, from which intermediate values of this ratio can be predicted. Results from a resistivity recovery study of molybdenum by Ibragimov, et al.[45] after fast neutron irradiation to 2 x 10^{20} n/cm^2, agree quite well with the prediction from Figure 2.74 in that a $\Delta\rho_{III}/\Delta\rho_{IV}$ ratio of almost one is obtained for approximately 2 x 10^{20} n/cm^2.

These results are all consistent with the formation of increasing number of interstitial clusters (i.e., increase in the ratio of the number of interstitials in clusters to the number of free interstitials) until a fast fluence of 10^{21} n/cm^2 is reached. There are practically no free interstitials remaining above this neutron fluence level.

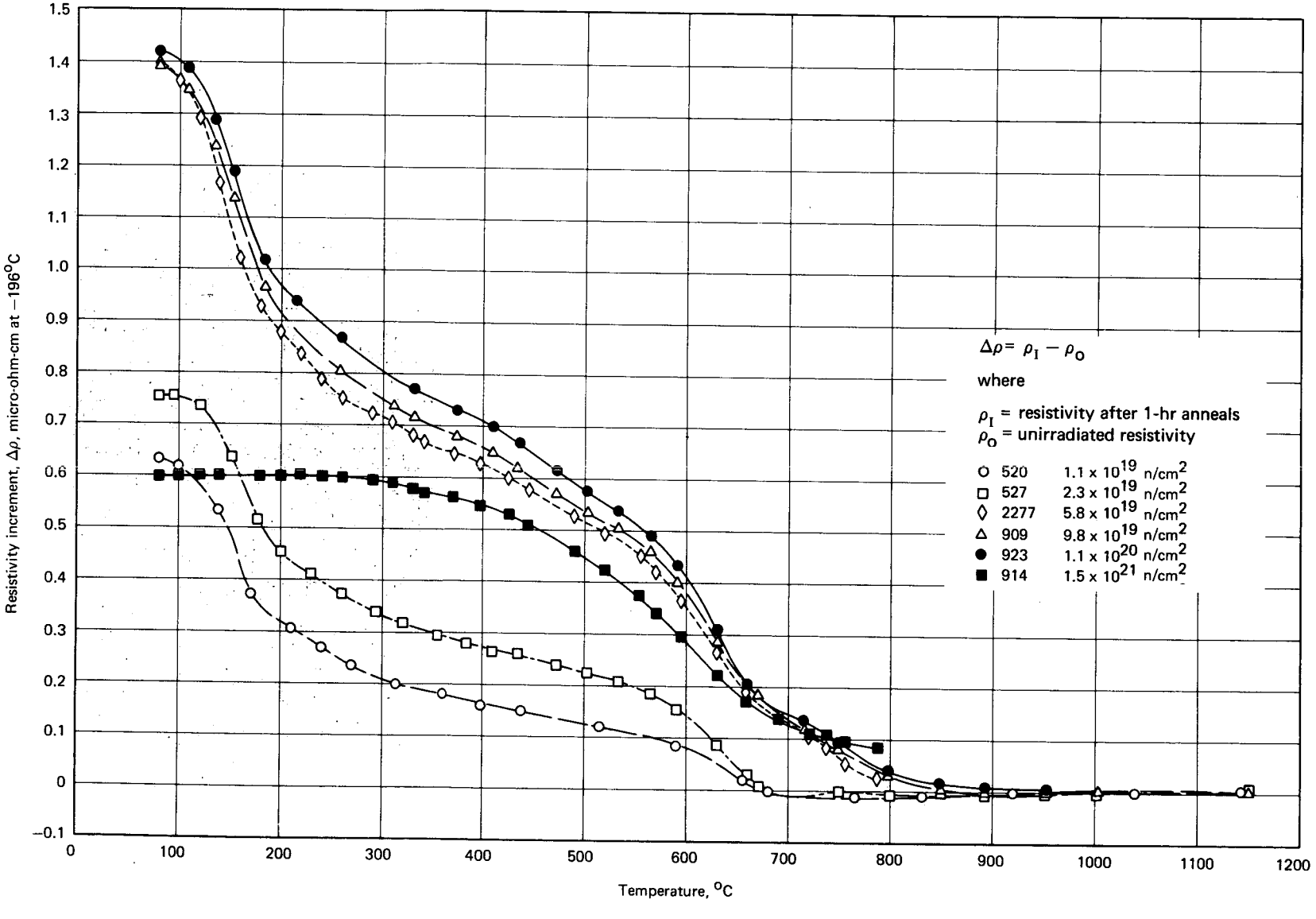

Fig. 2.71 — Isochronal resistivity recovery of neutron-irradiated, recrystallized molybdenum as a function of annealing temperature

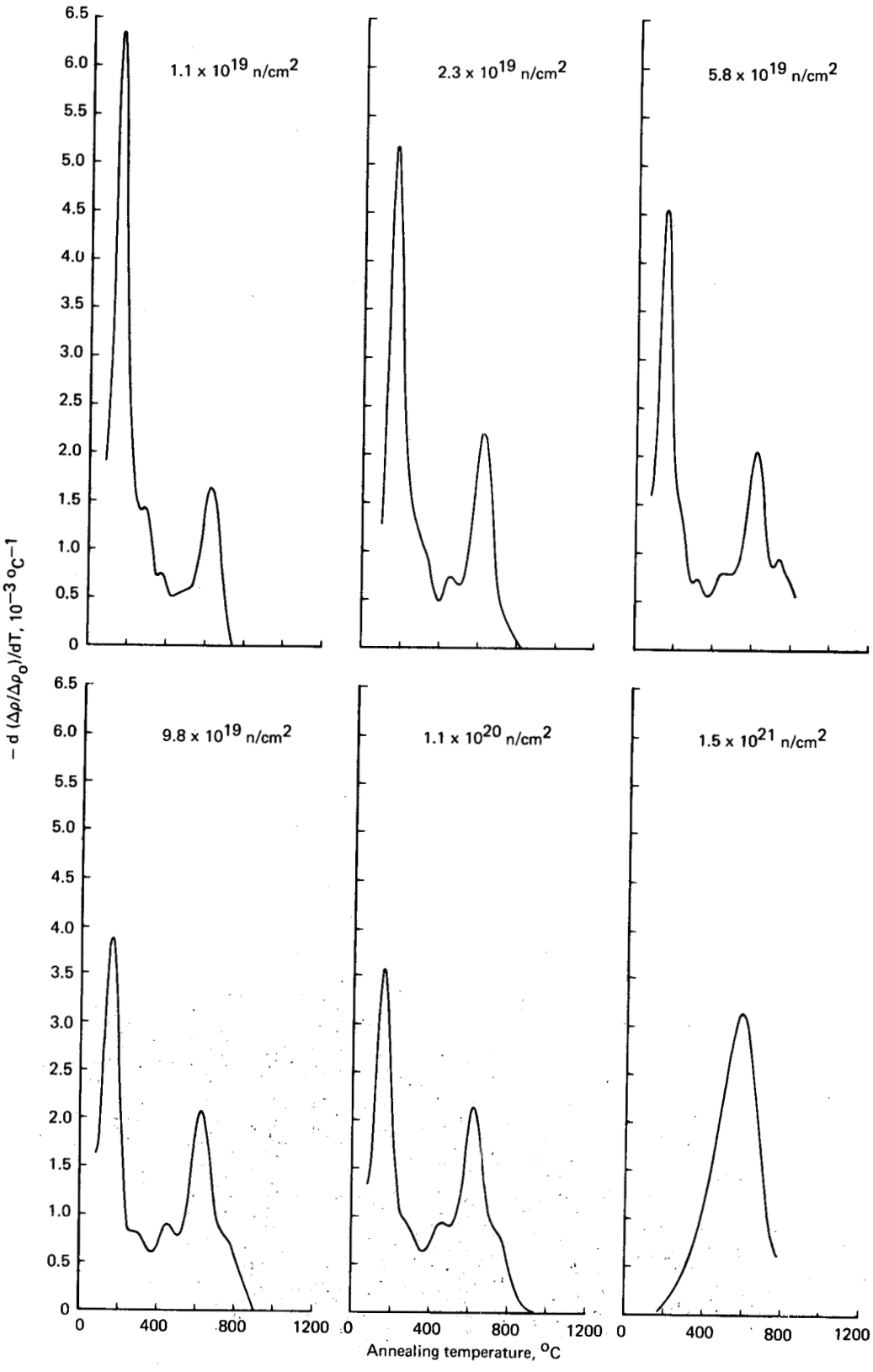

Fig. 2.72 – Derivative of the normalized isochronal resistivity recovery of neutron-irradiated, recrystallized molybdenum as a function of annealing temperature

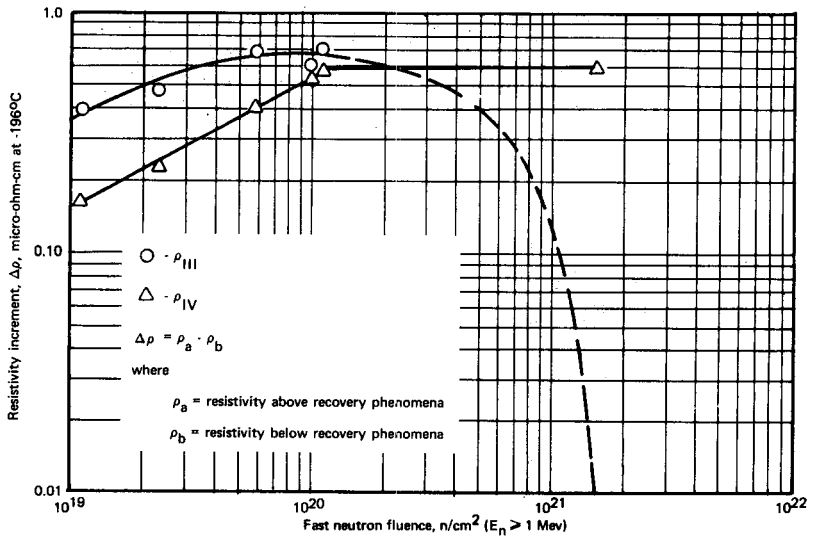

Fig. 2.73 — Resistivity recovery increments of stage III ($\Delta\rho_{III}$) to stage IV ($\Delta\rho_{IV}$) as a function of fast neutron fluence

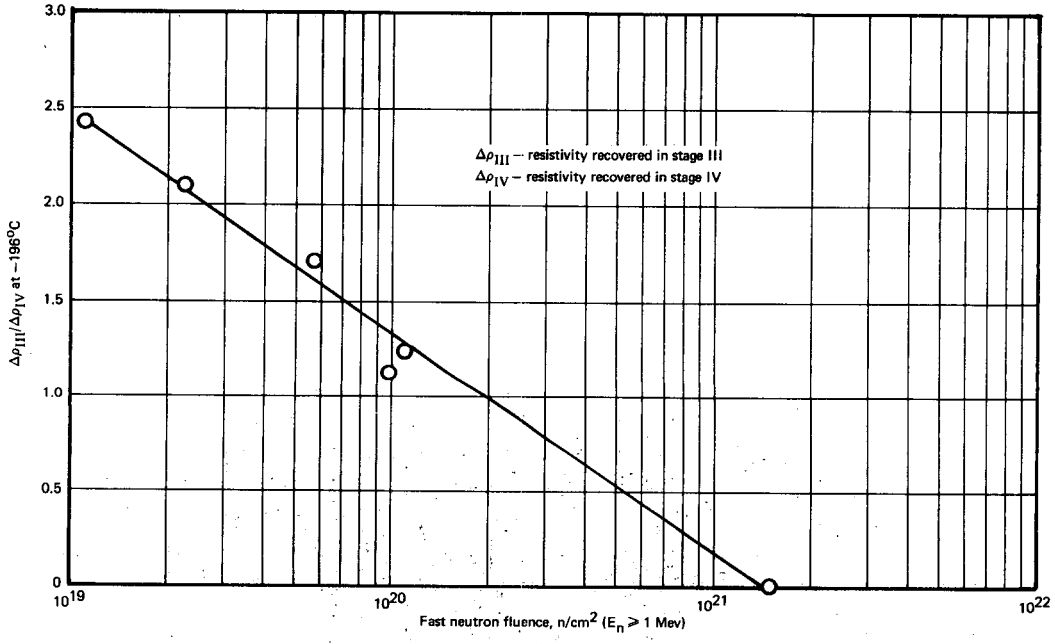

Fig. 2.74 — Ratio of resistivity recovered in stage III to stage IV as a function of fast neutron fluence

The major differences in the recovery behavior observed between tungsten and molybdenum undoubtedly arise from the differences in the homologous temperature of irradiation.[49] For tungsten, the irradiation temperature of approximately 70 °C corresponds to about 0.093 T_m, where T_m is the absolute melting temperature. For molybdenum, however, the irradiation temperature of 70 °C represents about 0.12 T_m. This represents an irradiation temperature corresponding to the onset of the stage III region in molybdenum and thus considerable recovery occurs during the irradiation. Recovery actually appears to begin at around 0 °C.[50,51] The 0.09 T_m irradiation temperature for tungsten is well below the recovery region for

stage III;[52] hence from the recovery point of view numerous point defects would be expected. Apparently irradiation within a recovery stage generates a larger ratio of cluster defects/point defects for the defects recovering in that recovery stage. This explanation is supported by the facts that the radiation-induced resistivity values observed for molybdenum are lower than for tungsten at the same radiation fluence, and that the slope observed for the neutron fluence dependence of molybdenum[53] is smaller than for tungsten.

The stage III recovery mechanism, considered to be the migration of point defects (interstitials), can also be compared to other metals with respect to the number of jumps such a migrating defect can make. It has been shown that a defect migrating with an activation energy Q, makes n jumps in a lifetime t before annihilation, with a vibrational frequency (v) of approximately 10^{14} sec^{-1}, at a temperature T according to:[54]

$$t = \frac{n}{v} e^{Q/kT} \qquad (2.2)$$

Rearranging this formula, for an isochronal anneal of a time t at a temperature T, a point defect can make n jumps according to:

$$n = t\, v\, e^{-Q/kT} \qquad (2.3)$$

Thus, for a 1-hour isochronal anneal, considering $Q \simeq 1.3$ ev[55] at 160°C, about 300 jumps can be made. This parallels the number of jumps which have been found in stage III for several metals.[54]

TRANSMISSION ELECTRON MICROSCOPY (R. C. Rau)

Microstructural studies using transmission electron microscopy were performed on neutron-irradiated tungsten and molybdenum. The objective of this work was to characterize radiation-induced microstructural features and, if possible, to relate those features to mechanical and physical properties. These studies concerned (1) characterization of dislocation loops in irradiated and annealed tungsten, (2) annealing of defect clusters in irradiated tungsten, and (3) effect of high irradiation temperatures on molybdenum.

Tungsten

Characterization of Dislocation Loops – Previous work[56, 57] has shown that post-irradiation annealing at temperatures near 1100°C produces resolvable dislocation loops in tungsten irradiated to fast neutron fluences of about 4×10^{19} n/cm^2 ($E_n \geq 1$ Mev) or greater. It had been postulated that the loops in tungsten were probably interstitial, based mainly on results in irradiated and annealed molybdenum,[58-60] but no diffraction contrast analyses had been carried out. To crystallographically characterize the loops in tungsten, tilting experiments in the electron microscope were performed on a specimen which had been irradiated to 1.5×10^{21} n/cm^2 at reactor-ambient temperature (~70°C), and subsequently creep-rupture tested (i.e., annealed) for 315 hours at 1100°C.

Thin foil specimens were prepared electrolytically[61] from an unstressed button head of the tested specimen. Preliminary scanning showed the microstructure to consist of well formed dislocation networks, making up subgrain boundaries, and a population of large dislocation loops averaging about 1000 Å in diameter.[57] Because of the polycrystalline nature of the specimens and the apparent lack of preferred orientation, grains sampled in the thin foils had random orientations. Hence it was necessary to scan many areas to find grains in reasonably simple orientations from which meaningful tilting experiments could be performed. Figure 2.75 shows six micrographs of an extensive series obtained from an especially suitable area. The orientation of this grain was near (001), and tilting was carried out about axes near [100], [$1\bar{1}0$], and [110]. The micrographs shown in Figure

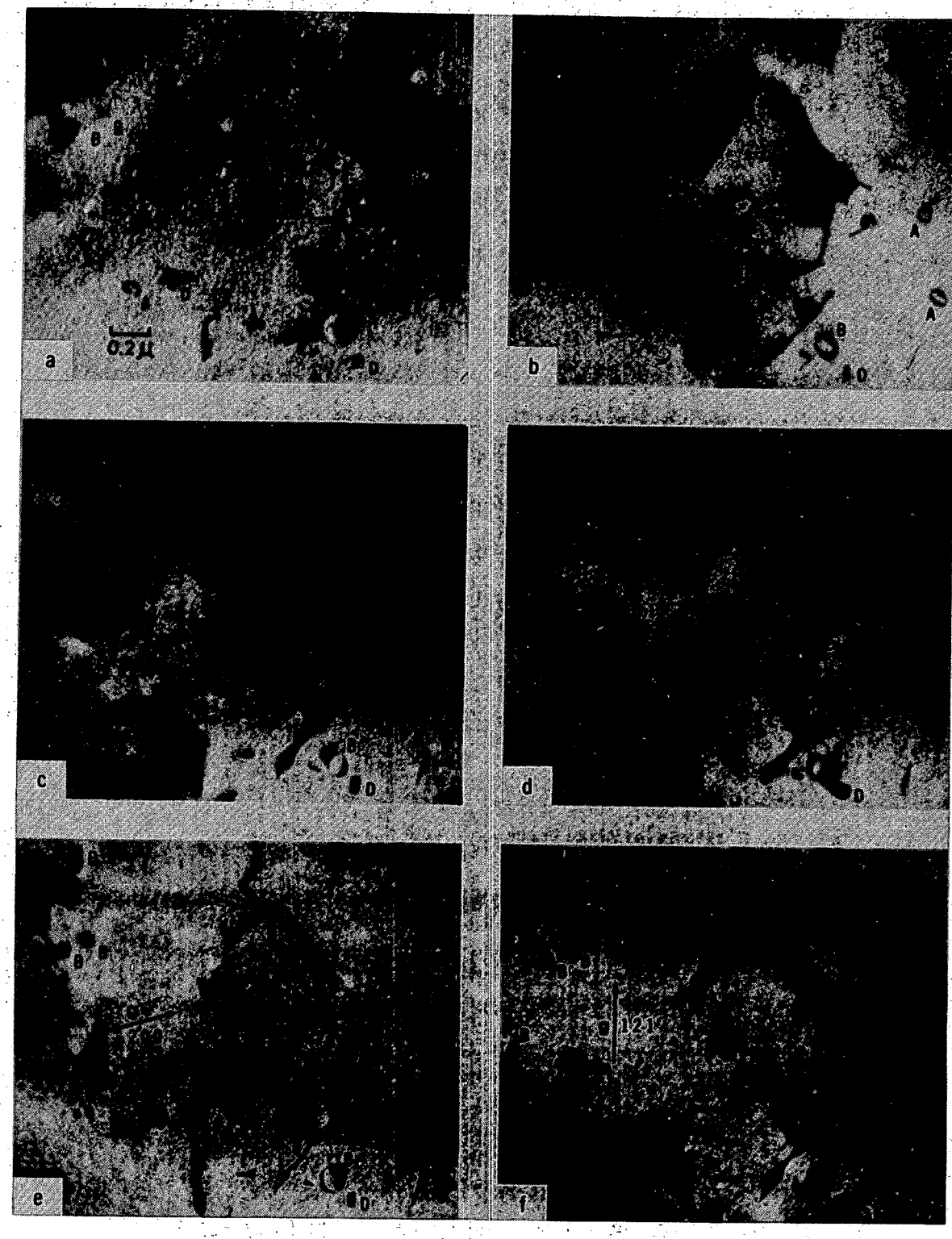

Fig. 2.75 — Dislocation loops in irradiated and annealed tungsten. All micrographs taken with $s > o$. (a) $\bar{g} = [1\bar{1}0]$, tilt $-19^{o}\ 50'$; (b) $\bar{g} = [110]$, tilt $-10^{o}\ 30'$; (c) $\bar{g} = [231]$, tilt $+1^{o}\ 50'$; (d) $\bar{g} = [2\bar{3}1]$, tilt $+5^{o}\ 30'$; (e) $\bar{g} = [200]$, tilt $+9^{o}\ 40'$; (f) $\bar{g} = [121]$, tilt $+13^{o}\ 50'$.

2.75 illustrate the complete characterization of the loops, i.e., their Burgers vectors, habit planes, and nature.

Burgers vectors of the loops were determined by noting diffraction conditions for which the loop images were at extinction; i.e., $\bar{g}.\bar{b} = 0$.[62] For example, loops labeled A and B are out of contrast in Figure 2.75a with $\bar{g} = [1\bar{1}0]$; loops labeled C and D are out of contrast in Figure 2.75b with $\bar{g} = [110]$. In Figure 2.75c and d, with $\bar{g} = \pm[\bar{2}31]$, only B loops are out of contrast; in Figure 2.75f, with $\bar{g} = [121]$, C loops are at extinction. These conditions unambiguously identify the Burgers vector of B loops as $\pm 1/2\,[11\bar{1}]$ and that of C loops as $\pm 1/2\,[1\bar{1}1]$. Similar analyses identified the Burgers vector of A loops as $\pm 1/2\,[111]$ and that of D loops as $\pm 1/2\,[\bar{1}11]$. The four sets of loops and their diffraction conditions in Figure 2.75 are summarized in Table 2.10.

Habit planes of the loops were determined by observing the manner in which their image shapes changed during tilting about known crystallographic directions, assuming their true shape to be circular. These observations, compared with observations of shape changes of circles drawn on a transparent tetrahedron, indicated that the loops lay on or

TABLE 2.10

MAGNITUDES OF $\bar{g}\cdot\bar{b}$ FOR OPERATING REFLECTIONS IN FIGURE 2.75

Loop	$\bar{b}$ \ $\bar{g}$	$[1\bar{1}0]$	$[110]$	$[\bar{2}31]$	$[2\bar{3}\bar{1}]$	$[200]$	$[121]$
A	$\pm\frac{1}{2}[111]$	0	± 1	± 1	∓ 1	± 1	± 2
B	$\pm\frac{1}{2}[11\bar{1}]$	0	± 1	0	0	± 1	± 1
C	$\pm\frac{1}{2}[1\bar{1}1]$	± 1	0	∓ 2	± 2	± 1	0
D	$\pm\frac{1}{2}[\bar{1}11]$	∓ 1	0	± 3	∓ 3	∓ 1	± 1

near {111} planes, with each loop lying on the particular {111} plane normal to its Burgers vector. Thus the loops are in edge orientation. The relative orientations of the four sets of {111} loops, both with respect to each other and with respect to the micrographs of Figure 2.75, are shown in the stereoscopic drawing of Figure 2.76.

The nature of the loops was determined by the formal method of analysis of the image contrast as the sign of the quantity $(\bar{g}.\bar{b})s$ was changed.[63] Using standard conventions to define the geometry of dislocations and their Burgers vectors,[64] the nature of the A, C, and D loops can be deduced from Figures 2.75c and d. For example, from the identification of the habit planes, it is known that C loops slope downward to the right in the micrographs. In Figure 2.75c these loops have outside contrast, indicating that $(\bar{g}.\bar{b})s$ is positive; hence the positive edge component of the Burgers vector has the same directional sense as the $\bar{g}$ vector. This situation obeys a right-hand rule, which indicates that the C loops are vacancy in nature.[63] Similar analysis of the contrast of the other loops indicates that they are all vacancy type. These results are summarized in Table 2.11.

Annealing of Defect Clusters in Irradiated Tungsten – To study the progressive effects of post-irradiation annealing on the defect structure of neutron-irradiated tungsten, a series of specimens were examined which had been irradiated to 4.2×10^{19} n/cm^2 ($E_n \geq 1$ Mev) at reactor-ambient temperature (~ 70°C). Following irradiation, the specimens received 1-hour anneals in argon at various temperatures and were tensile tested at 240°C.[35] The annealing temperatures and test results for both irradiated and unirradiated control samples are listed in Table 2.12.

Thin foils for transmission electron microscopy were prepared from both the unstressed button heads and the reduced areas near the fracture. Examination of foils from the button heads of unirradiated control specimens revealed that the starting microstructure contained

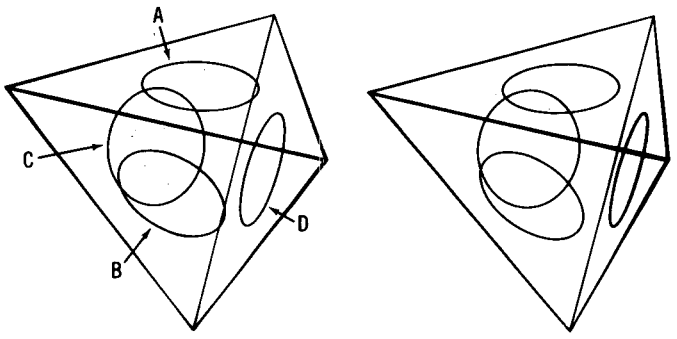

Fig. 2.76 — Stereoscopic drawing showing the appearance of loops on the four sets of {111} planes. The tetrahedron is oriented in approximate agreement with the foil orientation of Figure 2.75.

TABLE 2.11

ANALYSIS OF THE NATURE OF LOOPS IN FIGURES 2.75c AND 2.75d

Loop	Possible $\bar{b}$	$\bar{g} = [\bar{2}31]$, s + $\bar{g}\cdot\bar{b}$	Image	$\bar{g} = [2\bar{3}\bar{1}]$, s + $\bar{g}\cdot\bar{b}$	Image	Loop Nature
A	$\pm\frac{1}{2}[111]$	± 1	inside $\bar{g}\cdot\bar{b}<0$	∓ 1	outside $\bar{g}\cdot\bar{b}>0$	vacancy $\bar{b} = \frac{1}{2}[\bar{1}\bar{1}\bar{1}]$
B	$\pm\frac{1}{2}[11\bar{1}]$	0	—	0	—	vacancy[a] $\bar{b} = \frac{1}{2}[\bar{1}\bar{1}1]$
C	$\pm\frac{1}{2}[1\bar{1}1]$	∓ 2	outside $\bar{g}\cdot\bar{b}>0$	± 2	inside $\bar{g}\cdot\bar{b}<0$	vacancy $\bar{b} = \frac{1}{2}[\bar{1}1\bar{1}]$
D	$\pm\frac{1}{2}[\bar{1}11]$	± 3	inside $\bar{g}\cdot\bar{b}<0$	∓ 3	outside $\bar{g}\cdot\bar{b}>0$	vacancy $\bar{b} = \frac{1}{2}[1\bar{1}\bar{1}]$

[a]Nature of B loops determined from other micrographs not shown in Figure 2.75

TABLE 2.12

MECHANICAL PROPERTIES AND DEFECT CLUSTER DATA FOR IRRADIATED AND ANNEALED TUNGSTEN

Specimen No.	Fast Neutron Fluence,[a] n/cm^2 ($E_n \geq 1$ Mev)	Post-Irradiation Annealing Temperature, °C	T/T_M	Ultimate Strength, kg/mm^2	Elongation in 3.18 cm, %	Reduction in Area, %	Cluster Size, Å	Cluster Density, $No./cm^3$
10W	Unirradiated	240[b]	0.14[b]	49.9	37.7	55.2	—	—
7W	4.2×10^{19}	240[b]	0.14[b]	66.4	0.3	8.6	35	1.0×10^{17}
16W	Unirradiated	435	0.19	49.3	34.6	64.7	—	—
11W	4.2×10^{19}	435	0.19	61.7	1.1	8.2	35	2.2×10^{16}
26W	Unirradiated	743	0.28	50.7	21.9	33.6	—	—
23W	4.2×10^{19}	743	0.28	77.6	0.5	1.8	50	8.7×10^{16}
24W	4.2×10^{19}	897	0.32	60.0	0.6	2.1	50	1.1×10^{16}
25W	4.2×10^{19}	1043	0.36	52.3	12.0	12.3	100	3.5×10^{14}

[a]Irradiated at reactor-ambient temperature (~70°C).
[b]Tensile test temperature.

numerous dislocation tangles surrounding relatively dislocation-free cells, typical of worked and incompletely recrystallized metals. It was noted during subsequent examination of the irradiated specimen annealed at the highest temperature, 1043 °C, that these random tangles were partly replaced by more ordered networks of dislocations such as occur in well annealed and recrystallized metals.[65]

Examination of the irradiated specimens showed the presence of radiation-induced black-dot defect clusters and the effect of post-irradiation annealing on those clusters. Figure 2.77 shows photomicrographs illustrating typical microstructures in button head foils. In the unannealed condition (Figure 2.77a) a dispersion of fine dot clusters was present throughout the matrix. Annealing at 435 °C (Figure 2.77b) produced an apparent slight decrease in cluster concentration, but annealing at 735 °C (Figure 2.77c) resulted in a noticeable densification of the clusters. Finally, annealing at 897 °C (Figure 2.77d) and 1043 °C (Figure 2.77e) caused a definite decrease in cluster concentration and led to the formation of resolvable dislocation loops.

To obtain a quantitative comparison between defect cluster densities and tensile strengths of the specimens, cluster counts were made from the electron micrographs of Figure 2.77.[66] The resulting cluster densities listed in Table 2.12 are plotted as a function of annealing temperature in Figure 2.78a. This plot bears a striking resemblance to a plot of the tensile strengths of these samples shown in Figure 2.78b. These curves and the data in Table 2.12 show that annealing produces a minimum in the strength curve at 435 °C which corresponds to a depletion of defect clusters; a maximum occurs at 743 °C which corresponds to a pronounced coarsening and densification of the clusters. Higher-temperature annealing results in a loss of strength and a reduction in the population of defect clusters, in good agreement with previous findings.[56,57]

This complex annealing behavior is believed to be caused by two overlapping defect recovery peaks, one occurring below 435 °C and one above. The observed cluster density curve and hence the strength curve represent the sum of the two separate recovery curves. These separate recovery curves are due to the diffusion and agglomeration of two different defect species which require different thermal energies for migration. It is significant that the 435 °C minimum occurs somewhat beyond the 0.15 T_m (stage III) recovery peak observed in electrical resistivity studies; the 743 °C maximum occurs just below the 0.31 T_m (stage IV) recovery peak.[67,68] Both the 897 °C and 1043 °C annealing temperatures, which produce marked recovery in the observable microstructures, are above the 0.31 T_m recovery peak.

The assignment of specific migrating defects to the stage III and stage IV recovery regions has been the subject of much controversy in the literature, primarily because of the indirect measurement techniques involved. Recent direct observations on annealing in irradiated tungsten by field ion microscopy have provided conclusive evidence that stage III corresponds to the migration of free interstitials and stage IV corresponds to the migration of vacancies.[69-71] On this basis the defect clusters seen in the unannealed specimen in the present study are probably interstitial clusters, and those seen in the specimens annealed at the higher temperatures are probably vacancies. The clusters in the 435 °C annealed specimen might be remnants of the early interstitial cluster population, the beginnings of the buildup in vacancy cluster population, or a combination of both.

To check these conclusions, it would be desirable to carry out electron diffraction contrast experiments on the different specimens to identify the clusters present after each annealing temperature. Such experiments cannot be performed reliably, however, when the cluster density is high or when the clusters are not resolvable as dislocation loops. Hence in the present case only, the specimen annealed at the highest temperature, 1043 °C, was suitable for analysis. Large-angle tilting experiments were carried out on a foil from this specimen following the method of Edmondson and Williamson.[72] Figure 2.79 shows the

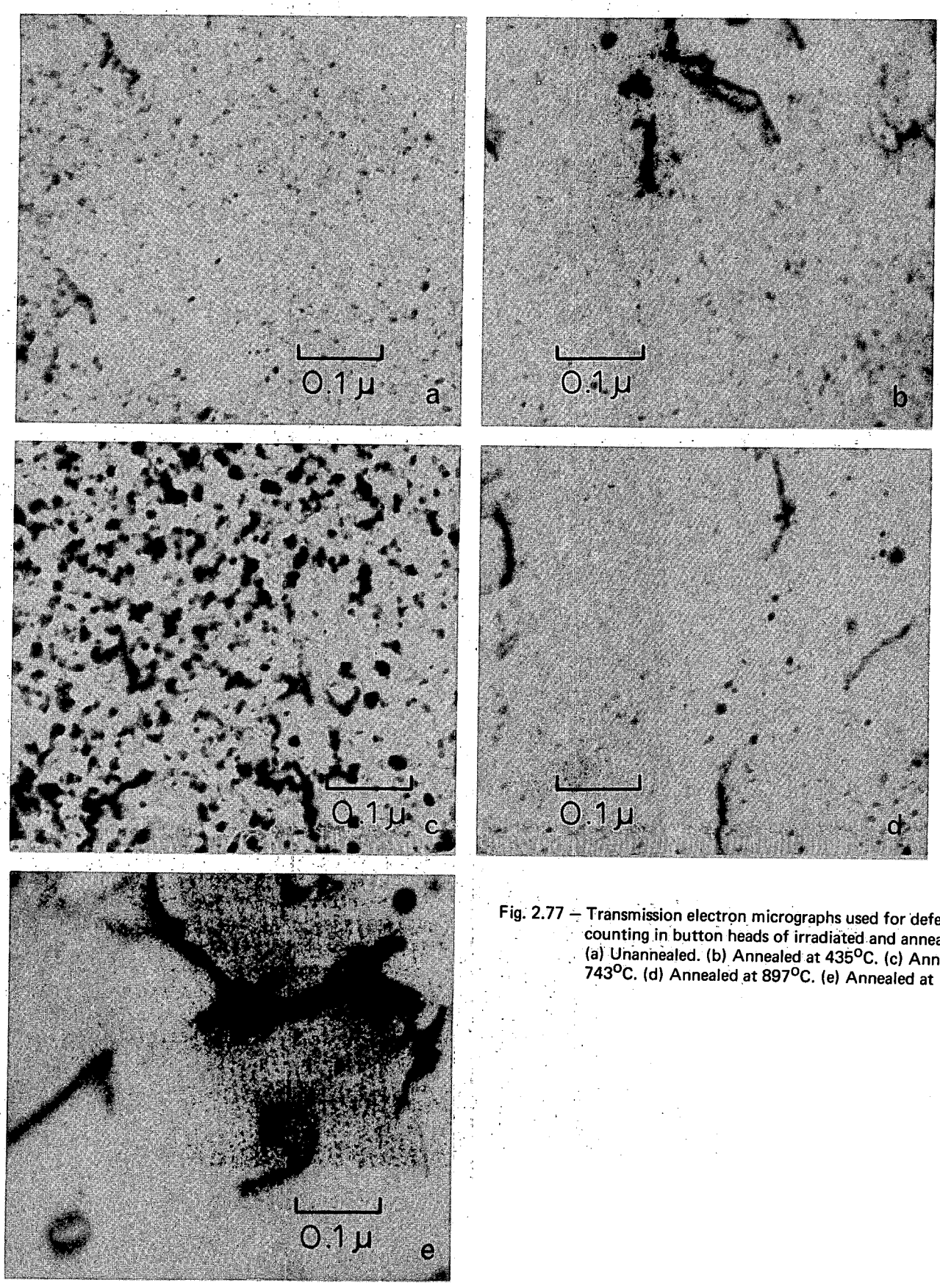

Fig. 2.77 – Transmission electron micrographs used for defect cluster counting in button heads of irradiated and annealed W. (a) Unannealed. (b) Annealed at 435°C. (c) Annealed at 743°C. (d) Annealed at 897°C. (e) Annealed at 1043°C.

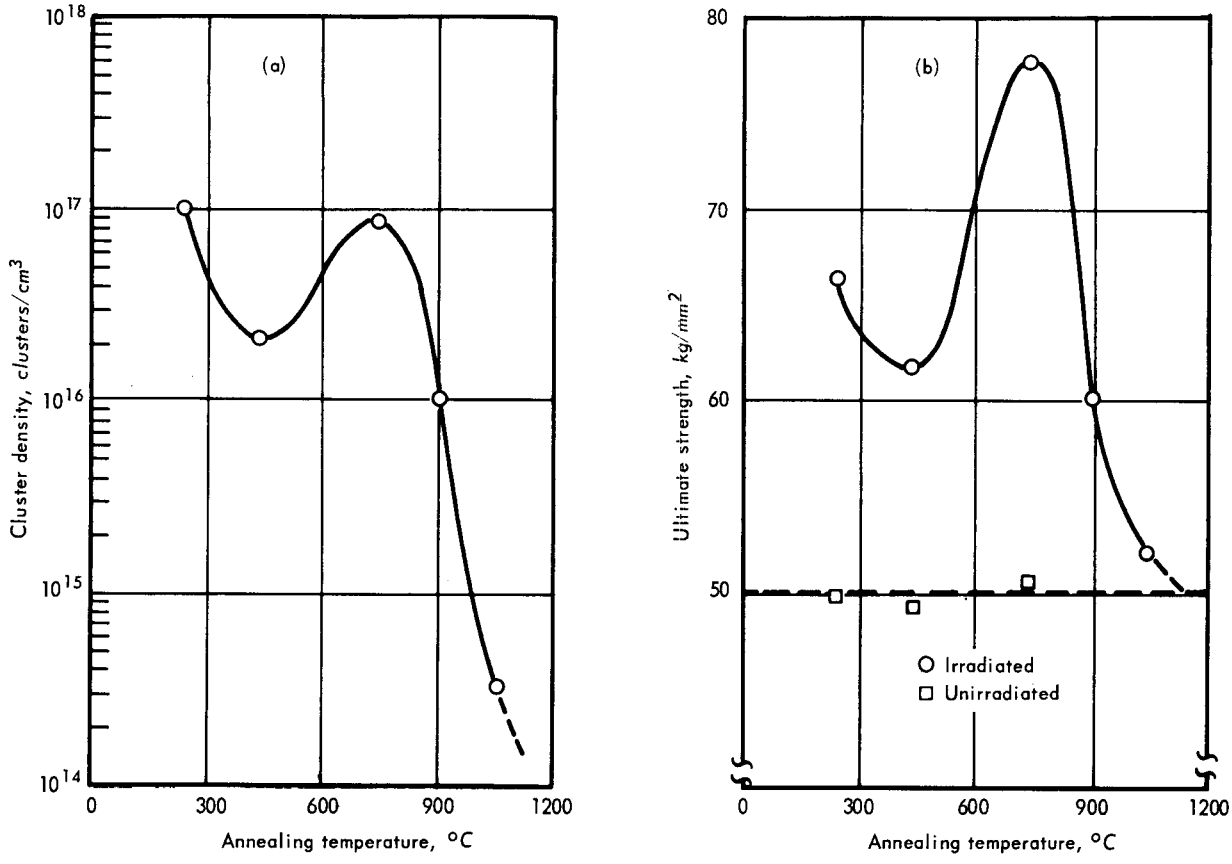

Fig. 2.78 — Effect of post-irradiation annealing temperature on defect cluster density, and ultimate tensile strength at 240°C of polycrystalline W irradiated at ~70°C to 4.2 x 10^{19} n/cm^2 ($E_n \geq 1$ Mev)

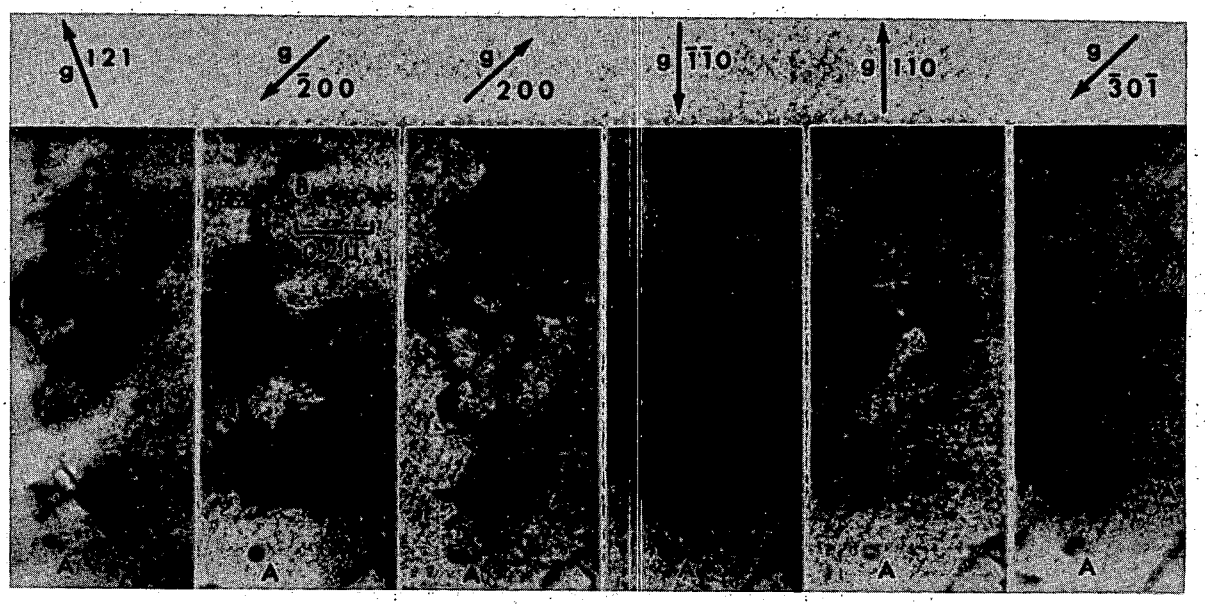

Fig. 2.79 — Series of electron micrographs used for identifying loops in tungsten irradiated to 4.2 x 10^{19} n/cm^2 at 70°C and annealed at 1043°C. All micrographs taken with $s > o$. (a) $\bar{g} = [121]$, tilt +18° 40′; (b) $\bar{g} = [\bar{2}00]$, tilt +2° 40′; (c) $\bar{g} = [200]$, tilt +0° 50′; (d) $\bar{g} = [\bar{1}\bar{1}0]$, tilt −6° 20′; (e) $\bar{g} = [110]$, tilt −8° 00′; (f) $\bar{g} = [\bar{3}0\bar{1}]$, tilt −17° 50′.

resulting micrographs. The figure shows that loops labeled A increase in apparent size due to purely geometrical factors as the foil is continuously tilted through a relatively large angle from +18° 40' to -17° 50', but the loop labeled B decreases in apparent size. But when the diffraction conditions are changed by reversing the sign of the quantity $(\bar{g}.\bar{b})s$ (i.e., by reversing $\bar{g}$ from $[\bar{2}00]$ to [200] or from $[\bar{1}\bar{1}0]$ to [110]), A loop images shrink and the B loop image expands. Thus the apparent size changes due to diffraction conditions are in the opposite sense to those due to geometrical factors for both A and B loops, and both are vacancy in nature.[72] This analysis agrees with the previous, more rigorous analysis of large loops in tungsten annealed at 1100°C (Figure 2.75), and supports the contention that vacancies migrate in stage IV.

In addition to specimens from the button heads, foils prepared from the gage sections near the fracture were also examined in the electron microscope. Detailed cluster counts were not made in the gage section foils, but it was apparent that the microstructures were generally similar to those in the button heads shown in Figure 2.77.[66] The sample annealed at 435°C was an exception; the observed cluster density in the gage section was noticeably lower than in the button head. This implies that the small clusters present after the 435°C anneal interact with and are possibly swept out by the dislocations moving along slip planes during tensile testing.[73]

Molybdenum

Defect Structures – Transmission electron microscopy studies were begun on a series of polycrystalline molybdenum specimens irradiated at three different temperatures and creep-rupture tested at 750°C.[74] This test temperature was selected on the basis of microstructural observations by Mastel and Brimhall,[75] who found that post-irradiation annealing at temperatures above 750°C led to a rapid decrease in defect cluster densities in molybdenum which had been irradiated at reactor-ambient temperatures. The specimens used in the present investigation, and their irradiation conditions and test results, are listed in Table 2.13.

TABLE 2.13

CREEP-RUPTURE DATA[a] FOR MOLYBDENUM TESTED AT 750°C AND 18.00 kg/mm^2

Specimen No.	Fast Neutron Fluence, n/cm^2 ($E_n \geq 1$ Mev)	Irradiation Temperature, °C	Rupture Life, hr	Elongation in 4.45 cm, %	Reduction in Area, %
1610	Unirradiated	–	20.38	39.5	95.7
1594	1.4×10^{20}	70	56.06	40.4	92.8
1622	1.8×10^{20}	700	244.06	37.6	94.4
1612	1.8×10^{20}	1000	355.09	31.1	95.2

[a]See Table 2.3 for complete history of specimens.

Thin foils were prepared electrolytically, using a mixture of 12.5 percent H_2SO_4 in methanol, from the unstressed button heads and the stressed regions near the fracture of the tested specimens. Examination of foils from the button head of the unirradiated control specimen showed a relatively defect-free microstructure containing only a few random dislocations. Stress at 750°C and the resulting deformation led to a microstructure of tangled networks of dislocations outlining subgrain boundaries, and free dislocations within the subgrains; these were revealed by foils from the gage section of this specimen.

Examination of button head foils from the specimen irradiated at pile-ambient temperature (~70°C) and tested at 750°C showed an abundance of resolvable dislocation loops, many quite large (up to 4000Å), shown in Figure 2.80a. These loops were uniformly distributed

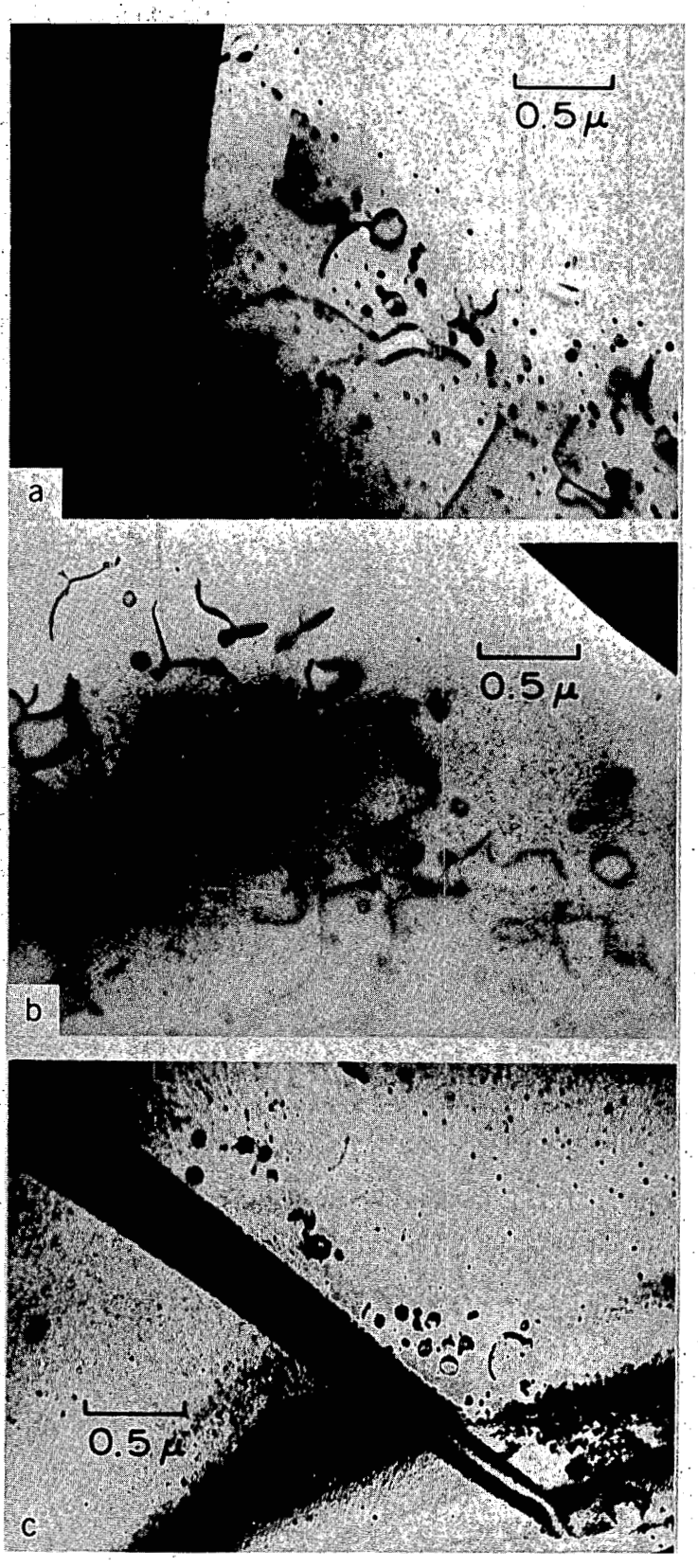

Fig. 2.80 — Microstructure in button heads of irradiated molybdenum creep-rupture tested at 750°C (a) irradiated at 70°C; (b) irradiated at 700°C; (c) irradiated at 1000°C

throughout the grains, and showed no tendency of denuding near grain boundaries. Preliminary diffraction contrast experiments indicated that the majority of the loops probably had a/2 <111> Burgers vectors, similar to the large loops in tungsten and in agreement with previous work on irradiated molybdenum.[58-60] Large-angle tilting experiments,[72] also preliminary, indicated that the loops were interstitial in nature. This result is consistent with other work on irradiated molybdenum.[58-60]

The microstructure of button head foils from the specimen irradiated at 700°C and tested at 750°C also contained a dense population of large dislocation loops within the grains (Figure 2.80b), but in this case a zone denuded of loops was present along the grain boundaries. The width of this denuded zone was about 1 micron, in agreement with recent observations by Brimhall et al.[76] on molybdenum irradiated to 3.5×10^{19} n/cm^2 ($E_n \geq 1$ Mev) at 600°C. Preliminary tilting experiments indicated that the loops were again interstitial in nature, and probably were in edge orientation, lying on {111} habit planes and having a/2 <111> Burgers vectors.

Examination of foils from the button head of the specimen irradiated at 1000°C and tested at 750°C showed a completely different microstructure than in the other two conditions. This microstructure (Figure 2.80c) was essentially the reverse of that seen in the 700°C irradiated specimen, and consisted of an almost structureless matrix containing a scattering of small black dots together with a few scattered colonies of loops located in regions within 1 micron of the grain boundaries. These loops, which averaged about 500 to 1000 Å in diameter, were tentatively identified as vacancy in nature. This result is consistent with the recent findings of Brimhall et al.[76] who reported that 1000°C annealing of molybdenum previously irradiated at 600°C led to the nucleation and growth of vacancy clusters within the 1-micron-wide denuded zone along grain boundaries.

Examination of the foils from the stressed regions in the gage sections of the molybdenum specimens irradiated at 70°C and 700°C showed dislocation tangles and networks outlining subgrain boundaries, typical of deformed metals. Gage section foils from the 1000°C irradiated specimen showed similar dislocation structures and evidence of pinning of dislocations by the small black dots in the matrix. Several such pinned dislocations can be seen bowing out from black dots in the micrograph of Figure 2.81. The identity of these black dots is not certain; they are not believed to be clusters originating from displacement events, but rather small carbide particles which precipitated during the 1000°C irradiation. The carbon content of this series of specimens was approximately 220 ppm, well in excess of the equilibrium solid solubility limit in molybdenum. The 1000°C irradiation temperature may cause precipitation of carbides from solution. Dislocation pinning by these particles probably accounts for the enhanced strength indicated for this specimen in Table 2.13.

Large dislocation loops were scattered throughout the matrix in gage section foils from the specimen irradiated at 1000°C and tested at 750°C. A fairly complete crystallographic characterization of these loops was made from a series of micrographs, two of which are shown in Figure 2.82. This diffraction contrast analysis indicated that most of the loops were edge loops, lying on {111} planes and having a/2 <111> Burgers vectors, but that they were interstitial in nature. This is in contrast to the tentative identification of vacancy loops in button head foils from this same specimen.

Finally, one rather unusual dislocation loop was found in the gage section of the 1000°C irradiated specimen. That loop is marked A in Figure 2.82a, taken with the (211) reflection operating. This loop is at extinction in Figure 2.82b, taken with the (002) reflection operating; i.e., g.b = 0. This behavior indicates that loop A cannot have a Burgers vector of the type a/2 <111> commonly found in bcc metals, but suggests that it must

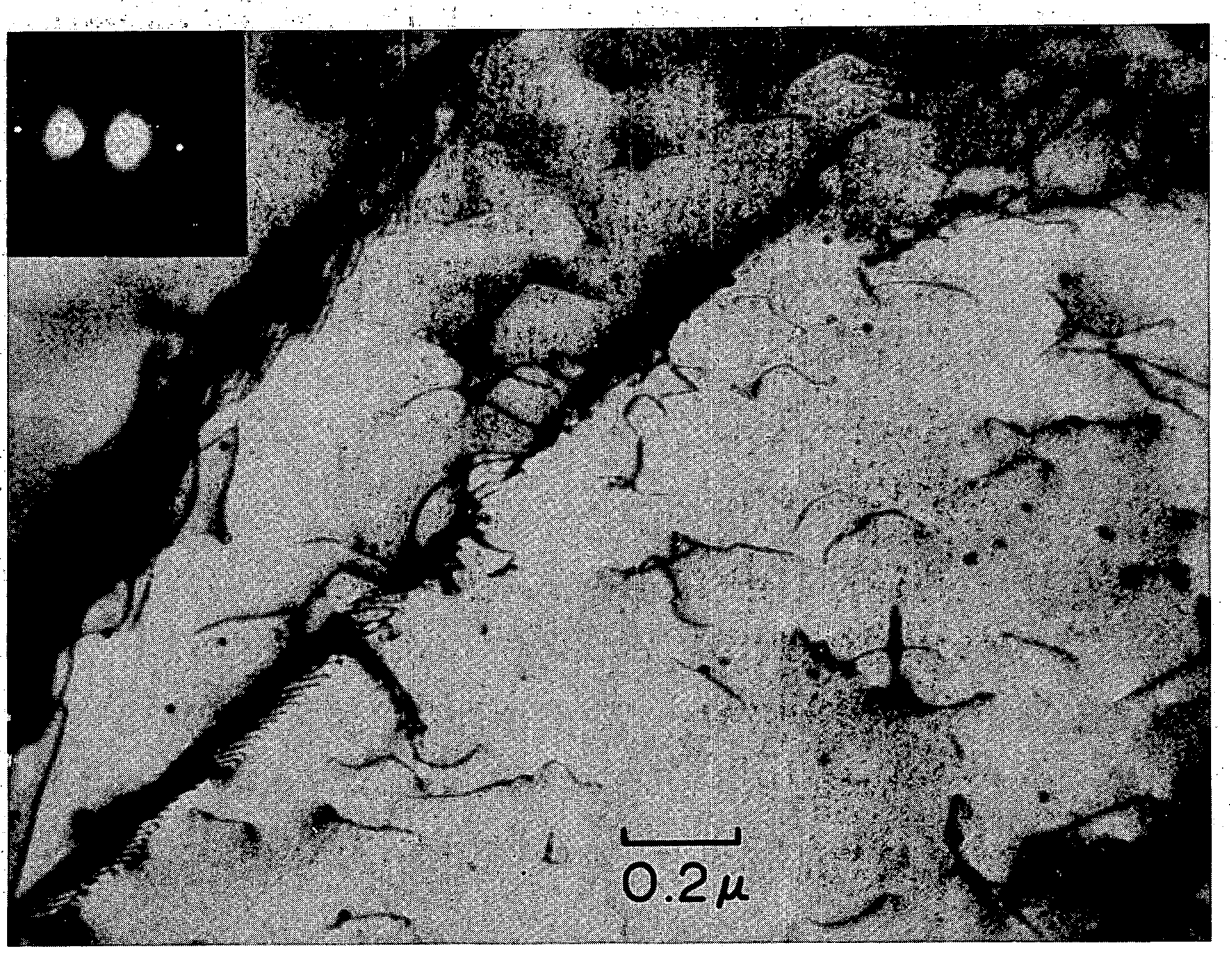

Fig. 2.81 — Pinning of dislocations by small carbide particles in stressed region of molybdenum irradiated at 1000°C and tested at 750°C

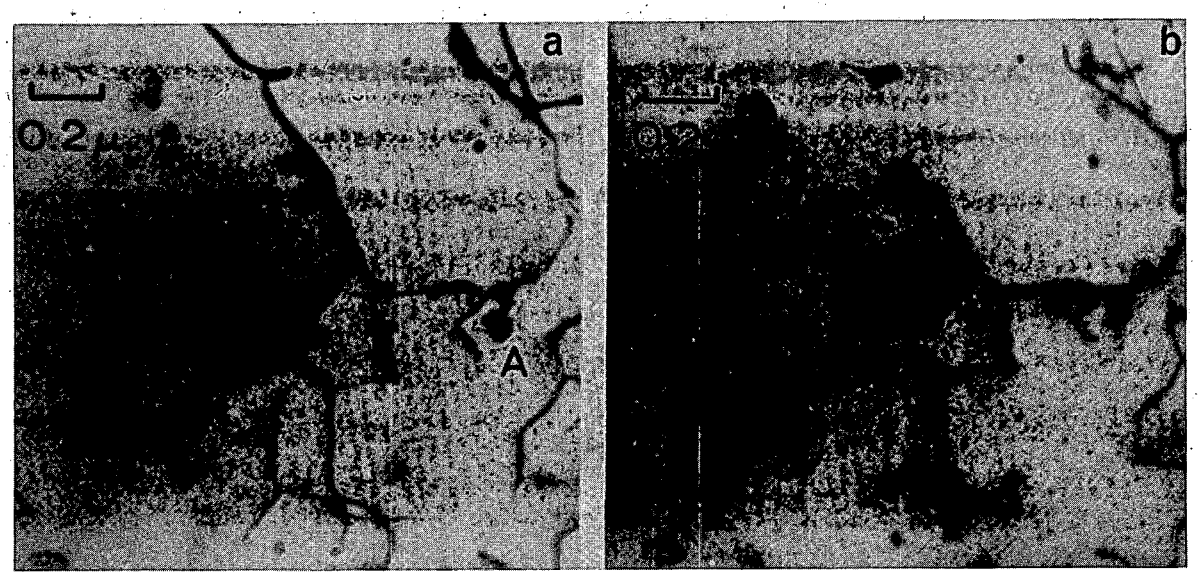

Fig. 2.82 — Dislocation loops in stressed region of molybdenum irradiated at 1000°C and tested at 750°C. Loop marked A is non-a/2<111> type. (a) $\bar{g}$ = |211|, tilt +9° 40′; (b) $\bar{g}$ = |002|, tilt −5° 40′.

have a higher-energy Burgers vector such as a <100> or a <110>. Although the available diffraction conditions were not sufficient to differentiate between these two possibilities, dislocation energy considerations strongly favor the a <100> choice.[77] Loops having Burgers vectors of this type have been found in iron bombarded with 150-kev Fe^+ ions,[78] but apparently have never been observed in neutron-irradiated bcc metals.

2.4 REACTOR DOSIMETRY

MONTE CARLO SPECTRUM CALCULATIONS (L. S. Burns, D. G. Besco, J. L. Kamphouse, J. Moteff)

The first phase of the Monte Carlo calculations of the neutron energy spectrum for various regions of the EBR-II was completed and some preliminary data are presented in this section. The neutron energy spectrum was determined for each region shown in the computer nuclear mockup in Figure 2.83. Gaps above and below the core were made equal in the mockup to utilize symmetry in the calculations. The spectrum was composed of 40 energy groups of equal lethargy between 0.01 and 14 Mev. The quadrilateral areas shown in the mockup are rotated about the reactor centerline to give a quasi three-dimensional geometry, described in the r-z plane and assumed in the ϕ rotational direction. Each region is composed of a homogeneous mixture of materials present in those regions. Neutron histories are started in the reactor and followed until they escape the configuration, are absorbed, or fall below the energy cutoff. The total number of neutrons below 0.01-Mev energy are also recorded for each region. The calculation considered elastic scattering, inelastic scattering, radiative capture, (n,α) reactions, (n-2n) reactions in beryllium, and neutron absorption without secondary emission. The core was composed of 91 elements with twelve control rods and two safety rods; it was surrounded by two rows of stainless steel and the U^{238} blanket. Appropriate axial and radial power distributions with a Watts fission spectrum were used to obtain source neutrons.

For presentation the integrals of the differential neutron flux densities, $\phi'(E)$, were normalized so that the number of neutrons above 1 Mev are equal to unity. These curves are given for four regions of the core in Figure 2.84. Regions 2A and 7A represent the third of rows 2 and 7, respectively, at the core midplane and above. Regions 2B and 7B represent the third of rows 2 and 7, respectively, above the midplane nearest the top of the core. Row 7 is actually within the stainless steel reflector surrounding the core. These four regions are clearly delineated in Figure 2.83.

The integrated neutron flux densities giving the fraction of neutrons above a given energy E, $\phi(E) = \int_E^{14} \phi'(E)dE$, for each one of the four regions, along with the Watt fission spectrum for comparative purposes, are shown in Figure 2.85. The energy E has the limits $0.01 < E < 14$ Mev. In this case $\phi'(E)$ was normalized so that the area under the complete curve from 0.01 to 14 Mev is equal to unity. The fraction of neutrons, $\phi(E)$, above 0.01 Mev as obtained from these curves are simply those considered in the detailed spectrum calculation. Since there are also neutrons present at energies below 0.01 Mev, the fraction of the total neutrons greater than E in the respective regions will be smaller than that obtained from Figure 2.85 by the factor k which will also be different for each region. These factors are listed in Table 2.14.

EBR-II FLUX DENSITY MEASUREMENTS (R. L. Stuart, J. L. Kamphouse, J. Moteff)

Wire monitors which were used for the flux mapping experiment in the EBR-II rows 2 and 7 positions were counted and preliminary results for the fast neutron flux densities were determined by using the threshold reactions $Fe^{54}(n,p)Mn^{54}$, $Ni^{58}(n,p)Co^{58}$, and

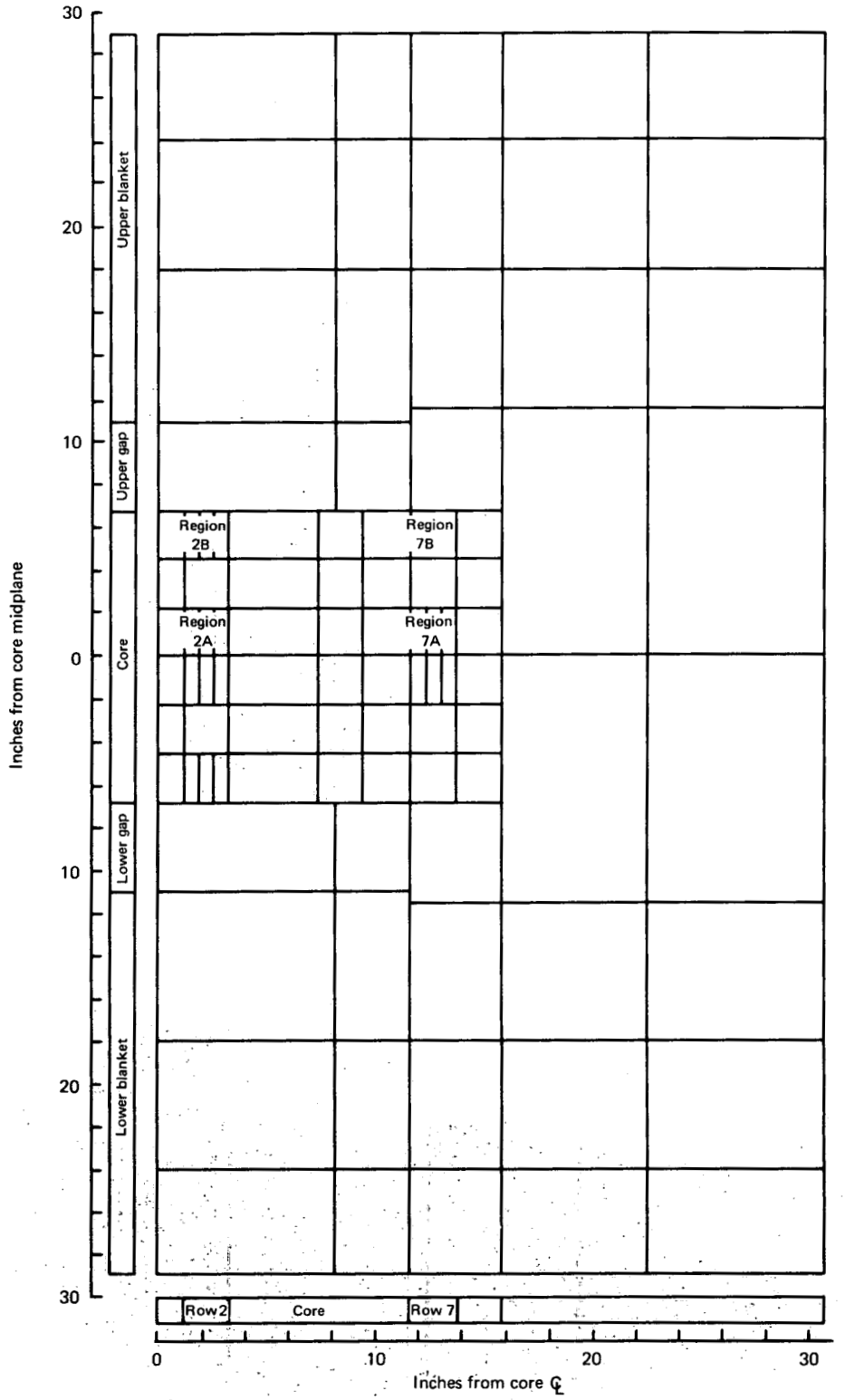

Fig. 2.83 – Computer nuclear mockup for Monte Carlo spectrum calculations in EBR-II

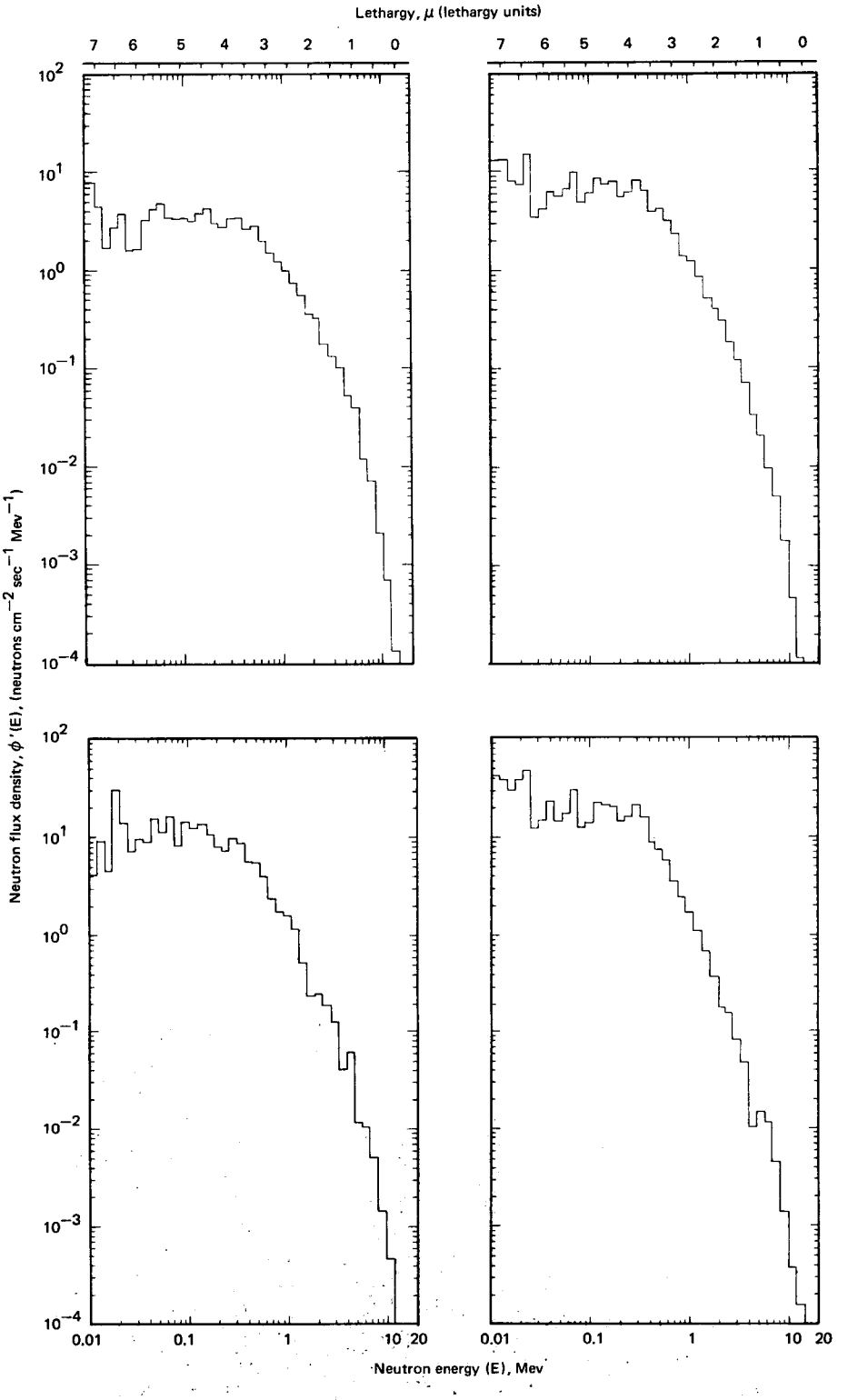

Fig. 2.84 — Monte Carlo neutron energy spectra for four core regions of the EBR-II. Spectra normalized to unity above 1 Mev ($\mu = \ln \frac{E_o}{E}$; E_o = 14 Mev

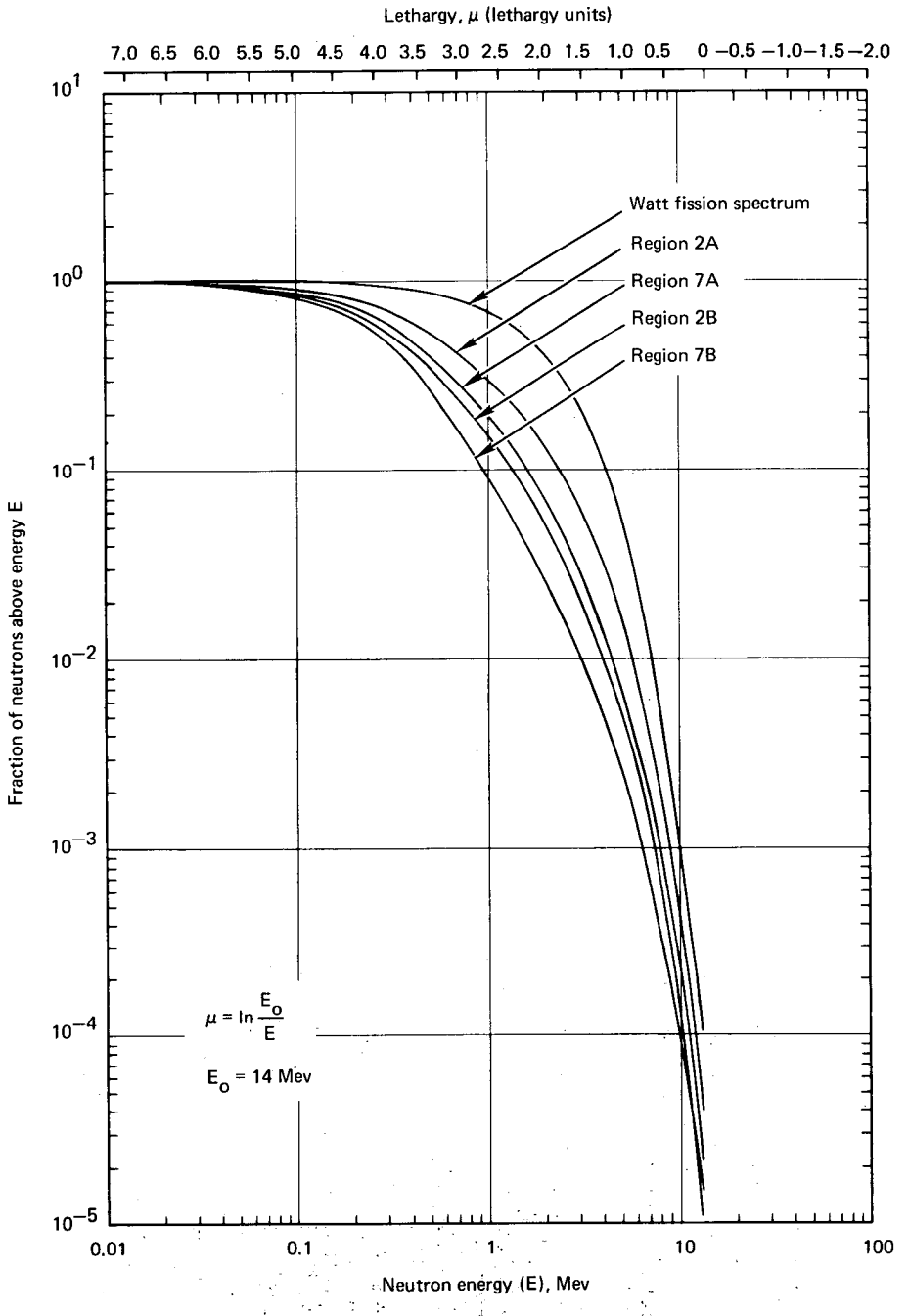

Fig. 2.85 — Monte Carlo neutron flux densities above energy E for four core regions of EBR-II. Flux densities normalized to unity above 0.01 Mev.

$Ti^{46}(n,p)Sc^{46}$. The $Co^{59}(n,\gamma)Co^{60}$ and $Fe^{58}(n,\gamma)Fe^{59}$ reactions were used to obtain information of the neutron environment at neutron energies below those obtained with the threshold reactions. A total of 148 dosimeters were used in this experiment.

The saturated activity of the Ni^{58} fast neutron dosimeters and the Co^{59} and Fe^{58} slow neutron dosimeters was normalized to unity at the core midplane and is given as a function of position in Figure 2.86. The actual values of the saturated activity for rows 2 and 7 at the core midplane are given in Table 2.14, for regions 2A and 7A. The Ni-Co dosimeter saturated activities for regions 2B and 7B were obtained from dosimeters located 15.2 cm above the core midplane, and the iron-saturated activity for regions 2B and 7B was obtained from dosimeters located 12.7 cm above the core midplane.

Using the Monte Carlo calculated spectra shown in Figure 2.84, the $Ni^{58}(n,p)Co^{58}$ and $Fe^{54}(n,p)Mn^{54}$ spectrum-averaged cross sections were determined for regions 2A, 2B, 7A, and 7B. These cross sections are given in Table 2.15 along with those obtained if one were to use a Watt fission spectrum. The neutron flux density ($E_n \geq 1$ Mev) was

TABLE 2.14

SATURATED ACTIVITY VALUES FOR FOILS USED IN EBR-II DOSIMETRY EVALUATION

Region	Saturated Activity, A_∞, dis. sec^{-1} mg^{-1}			
	$Ni^{58}(n,p)Co^{58}$	$Fe^{54}(n,p)Mn^{54}$	$Co^{59}(n,\gamma)Co^{60}$	$Fe^{58}(n,\gamma)Fe^{59}$
Row 2				
A	2.61×10^8	1.66×10^7	2.17×10^8	2.41×10^5
B	1.56×10^8	1.17×10^7	4.70×10^8	2.35×10^5
Row 7				
A	9.37×10^7	5.62×10^6	3.61×10^8	2.07×10^5
B	5.77×10^7	4.23×10^6	6.92×10^8	2.07×10^5

TABLE 2.15

SPECTRUM-AVERAGED CROSS SECTIONS AND FLUX DENSITIES FOR SEVERAL CORE REGIONS OF EBR-II

Region	Cross Section, $\bar{\sigma}_f$ ($E_n \geq 1$ Mev), millibarns[a]		Neutron Flux Density,[b] $\phi(E_n \geq 1$ Mev), n/cm^2-sec	
	$Ni^{58}(n,p)Co^{58}$	$Fe^{54}(n,p)Mn^{54}$	$Ni^{58}(n,p)Co^{58}$	$Fe^{54}(n,p)Mn^{54}$
Row 2				
A	117	103	3.19×10^{14} (2.31×10^{14})	2.45×10^{14} (1.78×10^{14})
B	84	74	2.65×10^{14} (1.38×10^{14})	2.43×10^{14} (1.27×10^{14})
Row 7				
A	89	80	1.49×10^{14} (8.23×10^{13})	1.05×10^{14} (6.02×10^{13})
B	64	59	1.28×10^{14} (5.07×10^{13})	1.10×10^{14} (4.59×10^{13})
Watt fission spectrum	162	141		

[a] Cross sections calculated using AFWL TR-65-34 (WL1) values; they are based on the EBR-II Monte Carlo spectra normalized to unity above 1 Mev (see Figure 2.84).

[b] Values in parentheses were obtained using the Watt fission spectrum-averaged cross sections, $\bar{\sigma}_f$ ($E_n \geq 1$ Mev), as listed in this table. The average cross sections, $\bar{\sigma}_f$, in a Watt fission spectrum are 112 and 98 mb, respectively, for the Ni^{58} and the Fe^{54} (n,p) reactions; i.e., $\bar{\sigma}_f$ ($E_n \geq 1$ Mev) = $\sigma_f/0.693$.

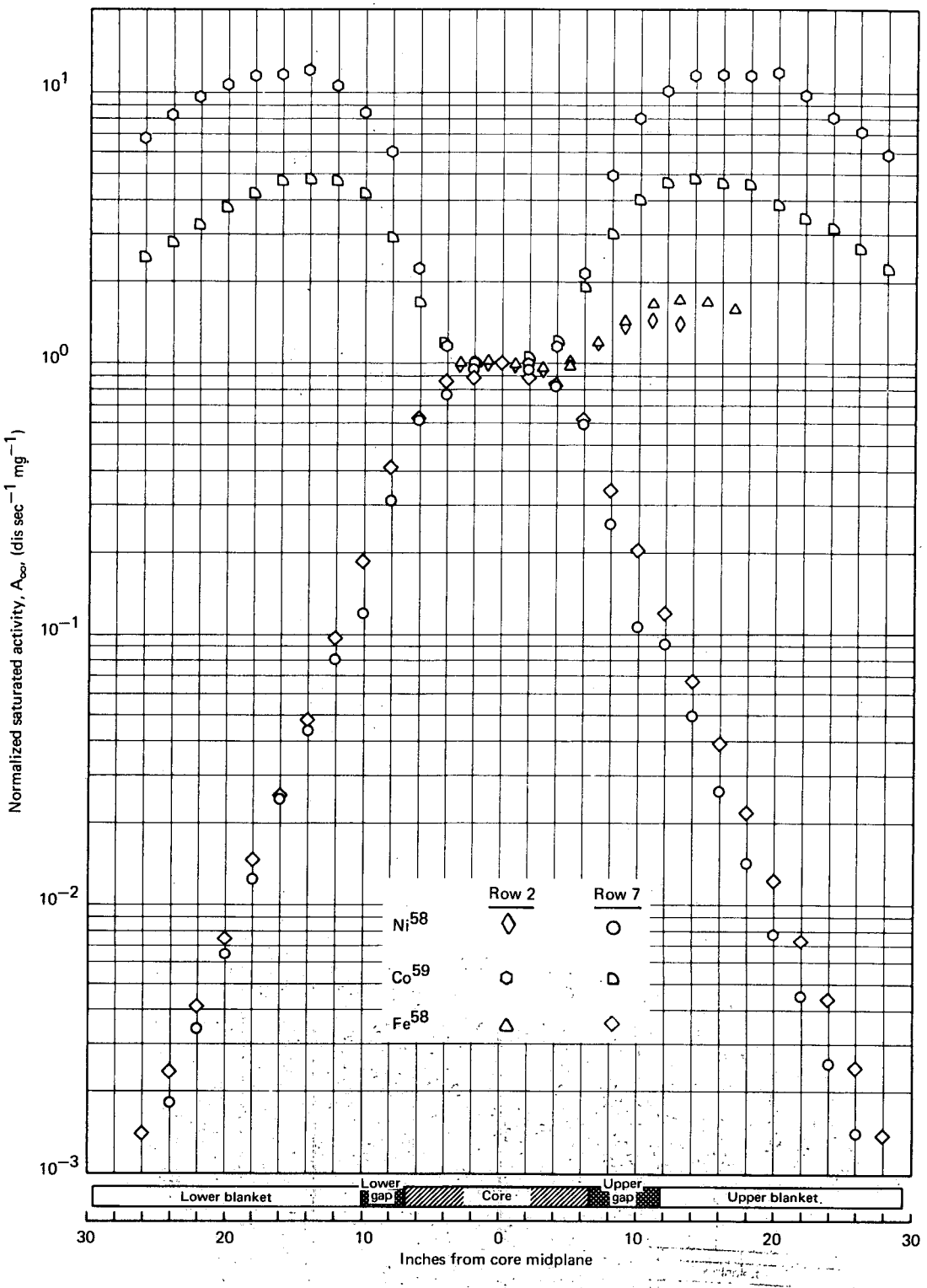

Fig. 2.86 -- Saturated activity for Ni^{58}, Co^{59}, and Fe^{58} as a function of position in EBR-II, normalized to unity at the core midplane

calculated from various dosimeters located in the four regions using the spectrum-corrected cross sections. The Ni^{58} dosimeters in regions 2A and 7A were located 15.2 cm above the core midplane. The Fe^{54} dosimeters in regions 2A and 7A were located 2.54 cm above the core midplane, and the Fe^{54} dosimeters in regions 2B and 7B were located 12.7 cm above the core midplane.

The neutron flux density ($E_n \geq 1$ Mev) as measured by the Fe^{54} dosimeters listed in Table 2.15 is essentially constant in going from the midplane to 12.7 cm above the midplane for either row 2 or row 7. Although the saturated activity is reduced about 40 percent, the spectrum-averaged cross sections are increased by almost the same amount and consequently the neutron flux density ($E_n \geq 1$ Mev) remains virtually constant. The Ni^{58} dosimeters show a similar trend. Serious errors can result if a Watt fission spectrum is assumed for obtaining the cross sections to be used in determining neutron flux densities from foil activities. The uncertainties can range from a factor of 1.4 in region 2A up to a factor of 2.4 in region 7B.

2.5 SUMMARY AND CONCLUSIONS

Post-irradiation creep-rupture tests of Incoloy 800 specimens irradiated in EBR-II to fast neutron fluences ($E_n \geq 1$ Mev) up to approximately 3×10^{20} n/cm^2 showed that the rupture life is reduced by irradiation when tested at 540°C but increased for a test temperature of 705°C. Correspondingly the minimum creep rate is increased at 540°C but decreased at 705°C. Post-irradiation rupture elongation values and in the region of 15 to 20 percent or about one-third the unirradiated value at 540°C, and in the region of 20 to 50 percent at 705°C, which is about one-half the unirradiated values.

Post-irradiation creep-rupture properties of Hastelloy X specimens irradiated in either ETR or EBR-II comparable fast fluences are essentially the same for both types of irradiation. The ductility determined by elongation measurements is about 5 percent for specimens irradiated to a fast neutron fluence of 3.2×10^{20} n/cm^2 ($E_n \geq 1$ Mev) compared to about 80 percent for the control at a test temperature of 704°C.

Hastelloy R-235 containing the same total boron (50 ppm) concentration but varying B^{10} isotope content and post-irradiation creep-rupture tested at 870°C showed increasing damage with increasing B^{10} content. This clearly supports the proposed mechanisms that the B^{10} isotope, in some manner, contributes to reduced ductility of irradiated alloys.

Transmission electron microscopy studies on irradiated A-286 and Hastelloy R-235 show shells of localized high-damage regions (dislocations) and gas bubbles with radii approximating the recoil distance of lithium and alpha particles in iron or nickel. The range of the lithium particle is calculated to be approximately 1 micron and that of the alpha to be about 2 microns.

Resistivity studies of irradiated ASTM-A302B indicate that the embrittlement is probably caused by the formation of a carbon-defect complex. This complex recovers in the temperature range of 300° to 500°C with the subsequent resolutioning of carbon. Resistivity studies on this material correlate, over the wide range investigated, quite well with radiation-induced changes and the subsequent recovery of mechanical properties.

The effect of irradiation temperature on creep-rupture properties of molybdenum at 750°C was determined. Irradiation at 70°C resulted in the least effect on the time to rupture; irradiation at 700°C and 1000°C showed increases in the time to rupture by factors of 12 and 18, respectively. There was also a relatively long second-stage creep period which increases with an increase in the irradiation temperature. Post-irradiation annealing at 1000°C of a specimen irradiated at 700°C did not produce a significant change in the creep rate but did increase the rupture life by 25 percent over that observed in the as-irradiated (700°C) condition.

Accelerated creep of irradiated molybdenum was observed at 580°C. Delayed creep, a period of time during the initial portion of the creep curve in which essentially no creep is observed to occur, was observed at 600°, 700°, and 750°C in specimens irradiated at reactor-ambient temperature. The accelerated creep was observed only for those specimens irradiated at the lower fluence (4.8×10^{18} n/cm^2, $E_n \geq 1$ Mev). Delayed creep to date has not been observed in control specimens, in tests of ambient temperature irradiated specimens at 580°, 850°, or 900°C, nor in 700°C and 1000°C irradiated specimens.

The effect of post-irradiation annealing on the 700°C creep-rupture properties of irradiated ($1\text{-}3 \times 10^{20}$ n/cm^2) molybdenum at two carbon levels, 26 ppm and 205 ppm, was studied. An annealing temperature of 900°C is necessary to remove the incubation period for delayed creep. Although an anneal at 1600°C eliminated the incubation period, this heat treatment does not restore the properties to control values. The data suggest the formation of stable defects at temperatures between 900° and 1200°C which tend to strengthen the irradiated material for those test conditions.

Initial results of the effects of irradiation at reactor-ambient (~70°C) temperatures to fast neutron fluences of 2.1×10^{20} n/cm2 ($E_n \geq 1$ Mev) on niobium and Nb – 1Zr tensile specimens show that the room-temperature yield strengths are increased about 110 and 200 percent respectively for the two materials. The yield strength increases at 650°C are about 93 and 110 percent, respectively, for niobium and Nb – 1Zr. The ductility of 360°C and 650°C of both metals is significantly reduced as a result of irradiation. Complete recovery occurs in the room-temperature strength and ductility of both metals following a 1000°C anneal for 1 hour.

A detailed study of the various recovery stages observed in resistivity measurements of isochronally annealed irradiated molybdenum was conducted. Molybdenum appears to saturate at about 1×10^{20} n/cm^2 ($E_n \geq 1$ Mev) with the saturation effect occurring as a resistivity maximum rather than the normal asymptotic approach. No significant stage III (~0.15 T_m) temperature shift nor residual resistivity was observed at high fluences or anneal temperatures; this indicates negligible transmutation reactions. The unusual saturation behavior apparently arises from the relatively high irradiation temperature (0.12 T_m) leading to a removal of free self-interstitials, with only excess vacancies left behind.

Hot-hardness studies of irradiated 73 percent warm-worked tungsten and irradiated recrystallized tungsten of the same sheet showed a factor of 3 greater radiation-induced hardening in the recrystallized material. Hardening occurred primarily in the athermal portion of the curve from 280°C (0.15 T_m) to 1050°C (0.36 T_m). Tests on recrystallized tungsten following either 73 or 98 percent warm working show the same values for either original material in the unirradiated and irradiated conditions. The hardness increase was the same for both cases, indicating that the substructure was the same for both materials. The 73 percent warm-worked material showed a radiation-induced hardness increase at 316°C (0.16 T_m); the 98 percent warm-worked material showed no additional increase.

Hot-microhardness data were also determined for Nb, Nb – 1Zr, Mo, Mo – 0.5Ti, 306 alloy (W – 30Re – 30Mo, at. %), 256 alloy (W – 30Mo – 25Re, at. %), Ta, and Ta – 10W from 25° to 1200°C. Most tests showed that the ultimate yield strength (σ_u) increases linearly with an increase in the hot-hardness (H_v) values when compared at corresponding temperatures. The relationship $\sigma_u = A H_v$, where A is a dimensionless number with values ranging from 0.3 to 0.4.

Transmission electron microscopy was used to study the annealing behavior of small defects in irradiated tungsten and to determine the crystallography of dislocation loops formed during this annealing. These studies revealed a complex annealing process attri-

buted to the presence of two overlapping temperature regions within which different defect species become mobile. At temperatures below 435°C annealing results from migration of free interstitials; annealing above this temperature is related to vacancy migration. Dislocation loops formed during high-temperature annealing (1100°C) are vacancy in nature and pure edge in character, lying on {111} planes and having a/2<111> Burgers vectors.

Microstructures of molybdenum irradiated at three different temperatures and creep-rupture tested at 750°C were studied by transmission electron microscopy. These observations revealed many interstitial dislocation loops throughout the matrix in specimens irradiated at 70°C and 700°C. In the specimen irradiated at 700°C, a zone about 1 micron wide, denuded of loops, parallels the grain boundaries. The specimen irradiated at 1000°C contained no loops within the matrix, but showed occasional loops thought to be vacancy in nature near grain boundaries. This specimen also showed evidence of small precipitates, believed to be carbides, which pin mobile dislocations.

Preliminary evaluation of the Monte Carlo spectrum calculations and the influence on fast neutron cross sections for the $Ni^{58}(n,p)$ and $Fe^{54}(n,p)$ reactions of wires irradiated in EBR-II was completed. Results show that although the experimentally determined saturated activity measured with the wire detectors is reduced about 40 percent from the core center to the core edge, the spectrum average cross sections ($E_n \geq 1$ Mev) are increased almost by the same amount. Consequently, the fast neutron fluence ($E_n \geq 1$ Mev) remains virtually constant throughout the core region. Serious errors can result if a Watt fission spectrum is assumed in the determination of the average reaction cross section of these detector wires. The resulting errors can be low by a factor of 1.4 in the center of the core up to a factor of 2.4 in the core region near the edge.

2.6 PLANS AND RECOMMENDATIONS

Investigations will continue to study the basic mechanisms of the effects of neutron irradiation on the stress-, strain-, time-, and temperature-dependent properties of selected heat-resistant alloys and refractory metals. Contributing mechanisms will be identified by considering current dislocation theories coupled with analyses of experimental data generated by creep, tensile, resistivity, and hot-hardness measurements and by direct observations of radiation-induced defects with the transmission electron microscope.

Particular emphasis will be given to the problem of radiation-induced changes in the ductility of some of these metals and alloys and to the importance of neutron spectra and fluence on both the substructure and the resulting mechanical properties.

In view of the need for information concerning the effect of neutron-induced changes in welds, a weld evaluation program will be initiated on selected candidate materials for fast breeder reactors. Selected materials will initially be limited to the heat-resistant alloys. Early work will concentrate on the general behavior of welds in unirradiated alloys.

Current investigation of the mechanisms of neutron-radiation-induced defects in various metals and alloys by isochronal and isothermal resistivity studies will be continued. Isothermal studies will be expanded to furnish migration energies and jump frequencies for various defect stages. Resistivity studies will be expanded to include iron- and nickel-base alloys, vanadium, and vanadium alloys. These resistivity studies will also be used to investigate the kinetics of bubble (or cavity) diameter changes and their influence on the cladding void volume.

Isothermal hot-hardness studies will be continued to investigate activation energies associated with various defect recovery stages in irradiated materials. Use of the hot-

hardness apparatus to study creep phenomena by varying indenter holding times will be conducted to employ hot-hardness methods for defining important temperature regions to be studied in tensile tests and to provide data for correlating and interpolating ultimate tensile strength of various irradiated alloys.

Detailed transmission electron microscopy studies to further define the kinetics of defect cluster and loop formation will be conducted. Emphasis will be placed on electron microscopy, resistivity, and density studies to define the number and size of defect loops, cavities, and/or gas bubbles for correlation with corresponding strength and hardness properties and changes in ductility.

Creep-rupture and tensile testing of irradiated specimens will be continued at temperatures above and below the prominent recovery regions to evaluate the magnitude and mechanisms of the neutron-irradiation-induced changes in properties. Particular emphasis will be given to those materials irradiated in EBR-II to fluences up to about 5×10^{22} n/cm^2. These studies will include detailed investigations on the radiation-induced changes in first- and second-stage creep behavior by the technique of applied stress changes on single specimens. The study of molybdenum and niobium alloys will be continued on potential LMFBR candidate materials including the vanadium-base alloys.

2.7 REFERENCES

1. Busboom, H. J. and Mathay, P. W., "Fast Neutron Damage Studies in High Nickel Alloys," GE-APED, GEAP 4985, August 1966.
2. Stiegler, J. O. and Weir, J. R., "Effects of Irradiation on Ductility," ORNL, ORNL-TM-2019, January 1968.
3. Monkman and Grant, Trans. ASTM, Vol. 56, 1956, p. 593.
4. "AEC Fuels and Materials Development Program Progress Report No. 69," GE-NMPO, GEMP-69, September 29, 1967, pp. 50-58.
5. Woodford, D. A., "Constant Load Creep Data Interpreted in Terms of the Stress Dependence of Dislocation Velocity," Trans. Met. Soc. AIME, Vol. 239, May 1967, pp. 655-659.
6. "Annual Progress Report for Period Ending June 30, 1966," ORNL, Metals and Ceramics Division, ORNL-3970, Table 20.3, p. 116.
7. Harwell, UK-AEA, private communications.
8. "Sixth Annual Report – High-Temperature Materials Program, Part A," GE-NMPO, GEMP-475A, March 31, 1967, pp. 205-208.
9. Wagenblast, H., Fujita, F. E., and Damask, A. C., "Kintics of Carbon Precipitation in Irradiated Iron-IV Electron Microscope Observations," Acta Met., Vol. 12, 1964, pp. 347-353.
10. Fujita, F. E. and Damask, A. C., "Kinetics of Carbon Precipitation in Irradiated Iron-II Electrical Resistivity Measurements," Acta Met., Vol. 12, 1964, pp. 331-339.
11. Carpenter, G. F., Knopf, N. R., and Byron, E. S., "Anomalous Embrittling Effects Observed During Irradiation Studies on Pressure Vessel Steels," Nucl. Sci. and Engr., Vol. 19, 1964, pp. 18-38.
12. Steele, L. E. and Hawthorne, J. R., "New Information on Neutron Embrittlement Relief of Reactor Pressure Vessel Steels," ASTM, STP-380, 1965, p. 289.
13. GEMP-475A, pp. 201-204.
14. "AEC Fuels and Materials Development Program Progress Report No. 71," GE-NMPO, GEMP-1002, December 29, 1967, pp. 48-50.
15. GEMP-69, pp. 58-61.
16. Gleiter, H. and Hornbogen, E., "Theory of the Interaction of Dislocations with Coherent Ordered Zones, (1)," (In German), Phys. Status Solidi, Vol. 12, 1965, pp. 235-250.

17. Copley, S. M. and Kear, B. H., "A Dynamic Theory of Coherent Precipitation Hardening with Application to Nickel-Base Superalloys," Trans. AIME, Vol. 239, 1967, pp. 984-992.
18. Raymond, E. L., "Effect of Grain Boundary Denudation of Gamma Prime on Notch-Rupture Ductility of Inconel Nickel-Chromium Alloys X-750 and 718," Trans. AIME, Vol. 239, 1967, pp. 1415-1422.
19. Gleiter and Hornbogen, op. cit., pp. 251-264.
20. Mastel, B. and Brimhall, J. L., "The Combined Effect of Carbon and Neutron Radiation on Molybdenum," Acta Met., Vol. 13, 1965, pp. 1109-1116.
21. GEMP-475A, pp. 69, 70.
22. Brimhall, J. L. and Mastel, B., "Effect of Prestrain and Subsequent Neutron Irradiation on Molybdenum," Acta. Met. Vol. 14, No. 4, April 1966, pp. 539-541.
23. Damask, A. C. and Dienes, C. J., "Point Defects in Metals," Gordon and Breach, New York, 1963, pp. 146-147.
24. GEMP-400A, pp. 86-90.
25. GEMP-475A, pp. 80-82.
26. GEMP-1002, pp. 61-63.
27. GEMP-1002, p. 60.
28. Tietz, T. E. and Wilson, J., "Behavior and Properties of Refractory Metals," Stanford University Press, 1965, p. 20.
29. Geary, A. L., "Fundamental and Applied Research in Metallurgy," Nuclear Metals, Inc., NMI-1258, September 17, 1963, p. 11.
30. Petty, E. R. and O' Neill, H., "Hot Hardness Values in Relation to the Physical Properties of Metals," Metallurgia, Vol. 63, 1961, pp. 25-30.
31. Westbrook, J. H., "Temperature Dependence of the Hardness of Pure Metals," Trans. ASM, Vol. 45, 1953, pp. 221-248.
32. O' Neill, H., "Hardness Measurement of Metals and Alloys," 2nd Ed., Chapman and Hall, Ltd., London, England, pp. 153-207.
33. Wronski, A. S. and Johnson, A. A., "A Hardening Effect Associated with Stage III Recovery in Neutron-Irradiated Molybdenum," Phil., Vol. 8, No. 90, June 1963, pp. 1067-1070.
34. GEMP-475A, pp. 73-77.
35. GEMP-400A, pp. 76-77.
36. Makin, M. J. and Minter, F. J., "The Mechanical Properties of Irradiated Niobium," Acta Met., Vol. 7, June 1959, pp. 361-366.
37. GEMP-475A, pp. 73-74.
38. "AEC Fuels and Materials Development Program Progress Report No. 67, GE-NMPO, GEMP-67, June 30, 1967, p. 55.
39. GEMP-475A, pp. 93-96.
40. Peacock, D. R. and Johnson, A. A., "Stage III Recovery in Neutron-Irradiated Molybdenum and Niobium," Phil. Mag. Vol. 8, 1963, pp. 275-284.
41. Holmes, D. K., "The Interaction of Radiation with Solids," North Holland Publishing Company, 1964, p. 147.
42. Kissinger, H. E., Brimhall, J. L., and Mastel, B., "Physical Characterization of Molybdenum Single Crystals for Irradiation Experiments," International Conference on Characterization of Materials," Pennsylvania State University, November 16-18, 1966.
43. GEMP-475A, p. 83.
44. GEMP-69, pp. 37-44.
45. Ibragimov, S. S., Lyashenko, V. S., and Zavyalov, A. I., "An Investigation of the Structure and Properties of Several Steels and Other Metals After Irradiation with Fast Neutrons," J. Nucl. Energy, Vol. 16, 1962, pp. 45-49.

46. Keys, L. K., Smith, J. P., and Moteff, J., "High Temperature Recovery of Neutron-Irradiated Tungsten," Bulletin of the American Physical Society, Vol. 13, 1968, p. 463.
47. Kinchin, G. H. and Thompson, M. W., "Irradiation Damage and Recovery in Molybdenum and Tungsten," J. Nucl. Energy, Vol. 8, 1958, pp. 275-284.
48. GEMP-69, p. 46.
49. GEMP-69, p. 42.
50. Kinchin and Thompson, op. cit. p. 279.
51. Nihoul, J., "The Recovery of Radiation Damage in Molybdenum," Phys. Stat. Solidi, Vol. 2, 1962, p. 310.
52. Kinchin and Thompson, op. cit., p. 280.
53. GEMP-475A, Figure 2.23, p. 87.
54. Lomer, W. H. and Cottrell, A. H., "Analysis of Point Defects in Metals and Alloys," Phil. Mag., Vol. 46, 1955, pp. 701-719.
55. DeJong, M. and Afman, H. B., "Resistometric Measurements on Molybdenum Irradiated with 2.5 Mev Electrons," Acta Met., Vol. 15, 1967, pp. 1-12.
56. Lacefield, K., Moteff, J., and Smith, J. P., "Neutron Radiation Damage in Tungsten Single Crystals," Phil. Mag., Vol. 13, 1966, p. 1079.
57. Rau, R. C., Moteff, J., and Ladd, R. L., "Comparison of Microstructure with Mechanical Properties of Irradiated Tungsten," J. Nucl. Mat., Vol. 24, 1967, p. 164.
58. Higgins, P. R. B. and Roberts, A. C., "The Nature and Annealing Behavior of Fission Fragment Damage in Molybdenum," J. Less-Common Met., Vol. 6, 1964, p. 472.
59. Downey, M. E. and Eyre, B. L., "Neutron Irradiation Damage in Molybdenum," Phil. Mag., Vol. 11, 1965, p. 53.
60. Meakin, J. D. and Greenfield, I. G., "Interstitial Loops in Neutron-Irradiated Molybdenum," Phil. Mag., Vol. 11, 1965, p. 277.
61. Ladd, R. L. and Rau, R. C., "Immersed Double-Jet Technique for Electrothinning Tungsten for Transmission Electron Microscopy," Rev. Sci. Instr., Vol. 38, 1967, p. 1162.
62. Hirsch, P. B., Howie, A., and Whelan, M. J., "A Kinematical Theory of Diffraction Contrast of Electron Transmission Microscope Images of Dislocations and Other Defects," Phil. Trans. Roy. Soc. A, Vol. 252, 1960, p. 499.
63. Mazey, D. J., Barnes, R. S., and Howie, A., "On Interstitial Dislocation Loops in Aluminium Bombarded with Alpha-particles," Phil. Mag., Vol. 7, 1962, p. 1861.
64. Bilby, B. A., Bullough, R., and Smith, E., "Continuous Distributions of Dislocations: A New Application of the Methods of Non-Riemannian Geometry," Proc. Roy. Soc. A, Vol. 231, 1955, p. 263.
65. GEMP-67, pp. 60-61.
66. GEMP-69, pp. 44-48.
67. Moteff, J. and Smith, J. P., "Recovery of Defects in Neutron-Irradiated Tungsten," ASTM STP-380, 1965, p. 171.
68. GEMP-475A, pp. 82-89.
69. Attardo, M. and Galligan, J. M., "A Field Ion Microscope Study of Neutron-Irradiated Tungsten," Phys. Stat. Sol., Vol. 16, 1966, p. 449.
70. Attardo, J. J., Galligan, J. M., and Chow, J. G. Y., "Interstitial Removal in Stage-III Recovery of Neutron-Irradiated W," Phys. Rev. Letters, Vol. 19, 1967, p. 73.
71. Jeannotte, D. and Galligan, J. M., "Energy of Motion of Vacancies in Tungsten," Phys. Rev. Letters, Vol. 19, 1967, p. 232.
72. Edmondson, B. and Williamson, G. K., "On the Determination of the Nature of Dislocation Loops," Phil. Mag., Vol. 9, 1964, p. 277.
73. Mastel, B., Kissinger, H. E., Laidler, J. J., and Bierlein, T. K., "Dislocation

Channeling in Neutron-Irradiated Molybdenum," J. Appl. Phys., Vol. 34, 1963, p. 3637.
74. GEMP-69, pp. 29-31.
75. Mastel and Brimhall, op. cit., p. 1109.
76. Brimhall, J. L., Mastel, B., and Bierlein, T. K., "Thermal Stability of Radiation Produced Defects in Molybdenum," Acta Met.
77. Dingley, D. J. and Hale, K. F., "Burgers Vectors of Dislocations in Deformed Iron and Iron Alloys," Proc. Roy. Soc. A, Vol. 295, 1966, p. 55.
78. Masters, B. C., "Dislocation Loops in Irradiated Iron," Phil. Mag., Vol. 11, 1965, p. 881.